# Thermal Measurement and Optimization of Materials and Processes in a Li-ion Cell

by

VIVEK VISHWAKARMA

Presented to the Faculty of the Graduate School of
The University of Texas at Arlington in Partial Fulfillment
of the Requirements
for the Degree of

DOCTOR OF PHILOSOPHY

THE UNIVERSITY OF TEXAS AT ARLINGTON
August 2017

# ACKNOWLEDGEMENTS

Coming to an end of Ph.D. is like the end of a wonderful journey. A journey full of amazing experiences, learnings and people. It gives me immense pleasure to think that finally after my PhD defense, I have got the opportunity to express my gratitude to all the people who helped in shaping up my dissertation.

First and foremost, I would like to thank my Ph.D. advisor Dr. Ankur Jain for his constant support and encouragement throughout the course of my graduate studies. Under his mentorship, I learned to conduct independent research and hone my problem solving skills. I am also grateful to him for being an enthusiastic supporter of my ideas and providing me freedom to pursue them. Apart from research, I am indebted to Dr. Jain for instilling in me his sense of discipline and teaching me how to be a good presenter, by setting a remarkable example by himself.

I would also like to thank my dissertation committee members: Dr. Samir Iqbal, Dr. Abdolhossein Haji-Sheikh, Dr. Cheng Luo and Dr. Albert Tong. Their valuable suggestions and advice helped me a lot in finalizing my Dissertation. I would also like to thank Dr. Fuqiang Liu and his research group, particularly, Zi Wei for teaching me and getting me started with the electrochemical characterization of Li-ion cells. I would also like acknowledge the generous support by the Mechanical and Aerospace Engineering Department and College of Engineering for the financial support.

My graduate life would have been far less enjoyable without the amazing friends. Thanks to Raghav Paul for having the patience to listen to my one-sided conversations and always being on my side. Words would fall short to describe the wonderful times I have had with Diya and Daipayan in last five years. Many thanks go out to my fellow labmates with whom I have had a lot of fun. Thank you, Krishna, Stephen, Arash, Dean, Hardik and Darshan. My special thanks to the staff at MAE – Debi, Lanie and Flora for being so kind and taking care of all the administrative work.

My family. My parents have been the pillar of support and it’s their love, encouragement, immense patience and sacrifices which has led to this thesis. Without their unflinching support I could not have carried on my education.

July 7, 2017

# ABSTRACT

## Thermal Measurement and Optimization of Materials and Processes in a Li-ion Cell

VIVEK VISHWAKARMA, Ph.D.
The University of Texas at Arlington, 2017

Supervising Professor: Ankur Jain

Applications of Lithium-ion cells range from consumer electronics to electric cars because of their excellent electrochemical performance and energy density. However, a Li-ion cell also suffers from poor thermal transport characteristics, which reduces performance, causes overheating and thermal runaway. This work contributes towards thermal characterization of key Li-ion battery materials and identifies and improves the rate-limiting, material-level thermal conduction process in a Li-ion cell.

Among the various materials within a Li-ion cell, the separator is expected to have the lowest thermal conductivity. In this work, we have carried out first-ever measurements of thermal conductivity and heat capacity of the separator material. These measurements are based on thermal response to an imposed DC heating within a time period during which an assumption of a thermally semi-infinite domain is valid. This in-plane measurement technique required microfabrication of microheater and thermal sensor on the flexible separator material. Experimental data are found to be in excellent agreement with the analytical model. Further investigation of heat transfer in Li-ion battery at material level resulted in the identification of cathode-separator interfacial heat transfer as the rate-limiting process that dominates overall thermal conduction in a Li-ion cell. This interfacial contact resistance contributes about 88% of the total thermal resistance in the cell. Further, to address this problem, an amine-based chemical bridging of the interface has been carried out. Experiments have showed that chemical bridging between separator and electrode resulted in significant reduction in the interfacial thermal resistance without any deterioration in electrochemical performance.

While conventional Li-ion cells utilize liquid electrolytes, future Li-ion cells are expected to use gel polymer electrolytes (GPEs) due to improved performance, safety and the possibility of a wide variety of shapes, sizes, and dimensions. Thermal properties of polymer electrolyte such as thermal conductivity and heat capacity are important parameters that will govern the thermal performance of future polymer Li-ion cells. In this work we presents the measurements of thermal and ionic conductivities in a PVdF-based GPE. The effect of incorporating BN/$Al_2O_3$ ceramic nano/microparticles in the GPE on thermal and ionic transport has been also characterized. The fundamental insights gained in this work on thermal transport in a GPE and the role of nano/microparticle inclusions may facilitate thermal-electrochemical optimization and design of GPEs for safe, high-performance Li-ion cells.

# TABLE OF CONTENTS

# LIST OF FIGURES

# LIST OF TABLES

# CHAPTER 1

# INTRODUCTION[1]

Li-ion cells are used for energy conversion and storage in a wide variety of applications, including consumer electronics, electric vehicles, aerospace systems, etc. [1, 2, 3]. Energy storage in hybrid and electric vehicles tremendously improves fuel efficiency, while also offering reduced emissions and other environmental benefits [4]. In other applications, Li-ion cells enable energy storage and conversion at very high density and rates compared to competing technologies [1, 5]. The capability of high efficiency energy storage facilitates the harnessing of renewable energy sources such as wind energy and solar energy [6], where energy storage is critical. Among several competing energy storage mechanisms, electrochemical energy storage in Li-ion cells offers several advantages in terms of energy density, power, etc. [3, 7], which has spurred significant amount of research in this technology.

From a scientific perspective, a Li-ion cell involves several multidisciplinary and multiscale processes that are closely coupled with each other [7-9], as shown in Figure 1.1. One such example is the coupling between thermal transport and electrochemical processes. Electrochemical reactions in a Li-ion cell generate heat, which influences the temperature distribution. The temperature

---

[1] Portions of this chapter are reprinted from "Measurement of Multiscale Thermal Transport Phenomena in Li-Ion Cells: A Review," by Krishna Shah, Vivek Vishwakarma and Ankur Jain, J. Electrochem. En. Conv. Stor. 13(3), 2016, after the permission from the ASME publisher (Appendix A)

distribution in turn governs the electrochemical reaction kinetics, ionic charge transport and crystalline phase equilibria of the electrodes. The dynamics of these phenomena are strongly coupled. For example, in addition to the thermal properties of the cell, temperature rise during discharge also depends on electrochemical properties such as equivalent series resistance (ESR). At the same time, electrochemical processes in the cell are themselves strong functions of temperature. As a result, thermal transport plays a key role in determining the electrochemical performance of the cell, particularly for high-rate processes.

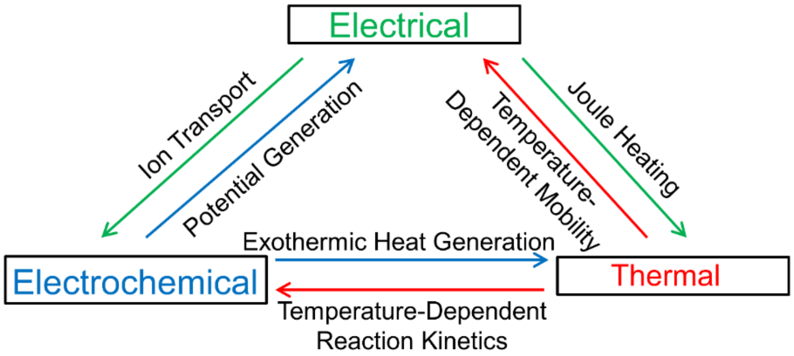

Figure 1.1. Schematic showing three significant categories of physical processes and the nature of their interactions in a Li-ion cell

As shown in Figure 1.1, electrical, electrochemical and thermal phenomena occurring in a Li-ion cell interact with each other through well-known processes, such as species diffusion, charge transport, chemical kinetics, thermal transport, etc. These processes are governed by physical laws involving multiple transport properties such as thermal conductivity, mass diffusivity, reaction rates, etc. Due to the heterogeneous nature of materials inside a Li-ion cell, these properties are often not well known in advance. In addition, these properties are often strong functions of temperature and electrochemical state of the cell, with significant spatial variation within the cell volume as well.

Further, these coupled phenomena occur over multiple lengthscales [8-10], as shown in Figure 1.2. At the molecular level, pertinent processes include Li ion intercalation in the electrode materials, species transport, etc. [7, 11-13]. Electrode layers, typically 5-50 μm thick, and a porous separator, are rolled or folded into cells [14, 15], which are then integrated in a battery pack [16]. The morphology and chemical composition of layers, overall packaging within a cell, and the arrangement of cells in a battery pack all influence the nature of physical processes

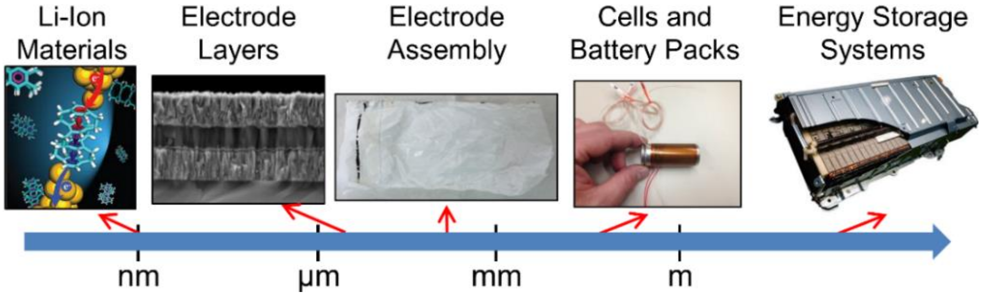

Figure 1.2. Schematic showing the multiscale nature of Li-ion based electrochemical energy storage and conversion

that determine performance, safety and reliability.

This dissertation is prepared to investigate the poor thermal performance of Li-ion cells and the possible ways of enhancing the thermal transport at material level. We have developed experimental techniques to measure thermal transport properties such as thermal conductivity ($k$) and specific heat capacity ($C_p$) of Li-ion cell materials. This work also recognizes other possible rate limiting steps responsible for poor thermal transport in Li-ion cells such as thermal contact resistance (TCR). While plenty of work is available to understand thermal transport at cell and pack level, literature on thermal transport at material level in Lithium-ion cells is lacking.

## 1.1. Battery Materials

Primary lithium cell with lithium metal as the anode was first proposed and developed in 1970s [17]. As the lightest metal and the least dense solid ($\rho$= 0.534 g.cm$^{-3}$), lithium has great potentials and advantages to be used as the backbone of the metal-ion batteries. In addition, lithium exhibits a -3.04 V potential deference against hydrogen electrode, which is desirable for most portable electronic devices. Due to their remarkable advantages such as high energy density, high capacity, and variable discharge rate, Lithium-ion cells have been rapidly applied in electronic devices [18]. The primary cells are one-off and non-rechargeable power sources, which is a major drawback for devices that require high current draw rates. However, in the 1980s, a rechargeable lithium battery was developed, also known as secondary lithium battery [19].

Both primary and secondary lithium batteries were designed based on metallic lithium as positive electrode in the earlier models. However, the interface between lithium metal and electrolyte was not stable since the lithium metal could detach from the surface of the cathode leading to serious safety issue [20-23].

Lithium-ion battery is an electrochemical energy storage system with lithium ion shuttling from negative electrode (Anode) to positive electrode (Cathode) during discharging and back when charging. Modern conventional rechargeable Lithium-ion cell consists of five major components such as separators, anode (negative electrode), cathode (positive electrode), electrolyte and current collectors. Physical and functional significance of these materials is discussed later in this chapter.

### 1.1.1. *Separators*

A separator is a highly engineered porous polymer membrane placed between electrodes of opposite polarity, permeable to ionic flow but preventing electric contact of the electrodes. It is a critical, multi-functional component of a

Li-ion cell that plays a key role in performance and safety during energy conversion and storage processes.

The flow of heat through the separator plays a key role in minimizing cell temperature and avoiding thermal runaway. Separator’s main function is to keep the positive and negative electrodes apart to prevent electrical short circuits while allowing rapid transport of ionic charge carriers to complete the circuit during the passage of current in an electro-chemical cell. [24] They are very good electronic insulators and have the capability of conducting ions by either intrinsic ionic conductor or by soaking electrolyte.

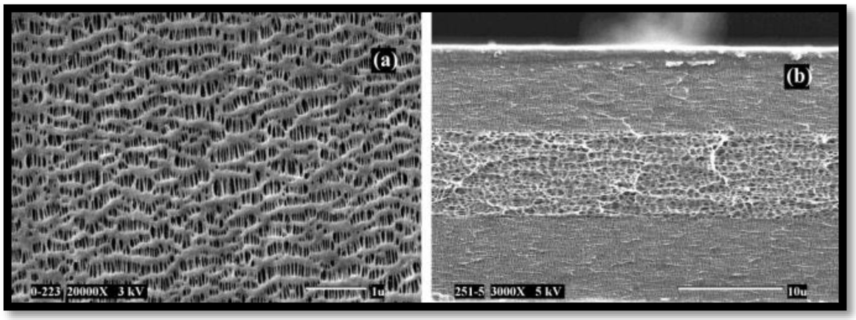

Figure 1.3. a) SEM of PE based battery separator and (b) PE/PP/PE composite battery separator [24]

Battery separator can be classified into different types based on their physical and chemical characteristics. They can be microporous, paper, woven, non-woven and bonded. Most of the traditional Li-ion cell used in consumer products operating at ambient and low temperature (<100 °C) are microporous in nature as shown in Figure 1.3. They are fabricated from a variety of inorganic, organic, and naturally occurring materials and generally contain pores that are greater than 50-100 Å in diameter. Materials such as nylon, cotton, polyesters, glass, polymer films (e.g. polyethylene (PE), polypropylene (PP), poly(tetrafluoroethylene) (PTFE), poly(vinyl chloride) (PVC)), and naturally occurring substances (rubber, asbestos, wood) have been used for microporous separators. The microporous polyolefins (PP, PE, or laminates of PP and PE) are widely used in lithium based nonaqueous batteries.

Polymer electrolytes have also attracted considerable attention for batteries in recent years. These polymers form complexes with a variety of alkali metal salts to produce ionic conductors that serve as solid electrolytes. Their use in batteries is still limited due to poor electrode/electrolyte interface and poor room temperature ionic conductivity. Due to the rigid structure, they can also serve as the separator. Polymer electrolytes are covered in more detail in section 1.1.3 and Chapter 4.

### 1.1.2. *Electrodes*

The anode (negative electrode) in conventional Li-ion cell is obtained by coating a graphite on copper film. Graphite is commonly used as the active material in negative electrodes mainly because it can reversibly place Lithium-ions between its many layers. low redox potential and excellent structural stability [25]. This reversible electrochemical capability is maintained over several of thousands of cycles in batteries with optimized electrodes [26, 27]. Other non-graphitic carbon, such as soft carbons, carbon nanotubes, and graphene, has also been investigated in the recent years [28].

The cathode (positive electrode) material in Li-ion battery chemistry is the major and active source of all the Li-ions [29]. In a Li-ion cell, because carbon electrode which acting as the negative doesn't have Li, the positive terminal must act as source of Li. Hence, intercalation compound is required for the cell assembly [30]. The most common cathode materials are $LiCoO_2$, $LiMnO_4$, $LiFePO_4$ and lithium layered metal oxides [31].

### 1.1.3. *Electrolytes*

Electrolyte plays the significant role of transmitting electrons and lithium ions during charging and discharging processes[32]. Also, electrolyte is one of the key components which defines the battery's electrochemical performance, safety, cycling performance, current density and thermal stability. Electrolytes can be divided into three major categories based on physical characteristics, such as liquid electrolyte, solid electrolyte, and gel electrolyte. Traditional Li-ion cells are designed based on liquid electrolytes, containing a lithium salt, such as $LiPF_6$, $LiBF_6$, $LiClO_4$, $LiBC_4O_8$, or $Li[PF_3(C_2CF_5)_3]$, dissolved in organic alkyl carbonate solvent. $LiPF_6$ is the most commonly used electrolyte for Li-ion cell due to low interfacial resistance, low cost and ease of synthesis. It has replaced other electrolytes and became the major material for electrolytes, which exhibits better overall performance including higher ionic conductivity. However, $LiPF_6$ offers low thermal stability compare to other lithium salts and decompose at 80°C in the following way [33].

Since commercial Li-ion batteries use $LiPF_6$ as lithium salt, and is sensitive to $H_2O$, it requires a non-aqueous solvent to improve the performance and safety of the battery, an organic alkyl carbonate can be a suitable solvent [34, 35]. The most common organic alkyl carbonate solvents are one or mixture of the following: propylene carbonate (PC), ethylene carbonate (EC), diethyl carbonate (DEC), and dimethyl carbonate (DMC). The cyclic carbonates, PC and EC, have high dielectric constant, which is a significant feature for dissolution of lithium salt, and high flash point, which is an important factor for the safety of the cells [36]. In the recent past, gel-polymer electrolytes (GPEs) have been widely investigated as a potential replacement of the conventional liquid electrolyte and separator [37-40]. A GPE comprises a polymer matrix capable of holding liquid electrolyte without sacrificing much of the electrochemical and mechanical performance [40]. The absorbed liquid electrolyte is immobilized within the pores of the polymer matrix, retaining the properties of the liquid electrolyte and conventional separator, while minimizing the volume of the combustible electrolyte needed, which results in improved safety [38]. By eliminating the need to contain a liquid electrolyte in a rigid containment, GPEs also offer an added advantage of enabling batteries in a wide variety of shapes, including flexible batteries [41,42]. Polyethylene oxide (PEO), polyacrylonitrile (PAN), polymethyl methacrylate (PMMA), and polyvinylidene fluoride (PVdF) are the most widely studied polymer matrices for GPEs [38, 40].

## 1.2. Thermal Property Measurements

The temperature field in any engineering system is governed by two key thermal transport properties – thermal conductivity, $k$ and heat capacity, $C_p$. While thermal conductivity refers to the property of the material to conduct heat, heat capacity refers to heat required to be added to a body for unit temperature rise. Thermal diffusivity α, defined as $\alpha=k/\rho C_p$ is also often measured for engineering systems. In addition to these material properties, thermal transport is also often a strong function of thermal interface resistance between materials. While heat capacity is a scalar quantity, in some systems, thermal conductivity may be strongly direction-dependent. In Li-ion cells, thermal conductivity anisotropy occurs due to the rolled/folded nature of the electrode stack. Both thermal conductivity and heat capacity are, in general, temperature-dependent, although in several cases, these properties may be nearly constants within the temperature range of interest. While thermal conductivity is often measured through the temperature field resulting from an imposed heat flux or vice versa, heat capacity is generally measured by determining the heat needed to be added for a specific temperature rise.

In the context of Li-ion cells, thermal property measurements can be carried out at multiple spatial scales, including for individual materials of a Li-ion cell, such as separator, electrodes, etc., individual cells, as well as for larger systems. Thermal transport, particularly in larger systems is also often characterized in terms of lumped thermal circuit parameters, including thermal resistances and thermal capacitances of various components. Such an approach facilitates circuit representation and analysis of thermal behavior of systems.

Several experimental measurements, both of fundamental thermal conductivity and heat capacity have been reported for Li-ion cell materials. Thermal property measurements are primarily done either at material level or at the cell level in Li-ion cells. At material level, thermal property measurements of electrodes [45-49], electrolyte [50], separator [51, 52], electrode stack [46, 53] and contact thermal resistance [54, 55] have been reported. Such material level measurements are key in understanding heat transfer inside a Li-ion cell and in determining the rate limiting heat transfer processes.

Thermal property measurement of polymer electrolyte has been carried out using a guarded heat flowmeter [50].Temperature difference across the sample is measured which is used to calculate the total thermal resistance, from which thermal conductivity of the polymer electrolyte has been extracted. Thin polymer electrolyte films are prepared by doctor blade technique and sandwiched between top and bottom plates, across which the temperature difference is measured. Thermal conductivity reported to vary from 0.12 to 0.22 W/mK over a 25-150 °C temperature range [50].

Similarly, thermal property of a composite cathode has been measured using a heat flowmeter [45]. The composite cathode is made of equal volume fractions of polymer electrolyte, and a mixture of active material and acetylene black. The thermal conductivity of the composite is measured to vary in the 0.2-0.5 W/mK range between 25 °C and 150 °C [45].

Time-domain thermoreflectance (TDTR) has been used to measure thermal conductivity of $LiCoO_2$ thin film. Effect of the degree of lithiation on thermal conductivity has been measured. In situ measurements of thermal conductivity of

$LiCoO_2$ cathode during cycling show thermal conductivity to reversibly decrease from 5.4 to 3.7 W/mK when delithiated [47].

In-plane thermal conductivity of the separator material has been measured using a DC heating method [51]. Two thin metal lines, separated by a small distance, are microfabricated on the separator material. One of the lines is used as a heater, while both are used for temperature measurement. Ultrafast measurement of temperature of both lines as a function of time is used for determining thermal properties of the separator. In-plane thermal conductivity and heat capacity of 0.5 W/mK and 2480 J/kgK respectively are reported at room temperature [51]. These values do not change significantly when measured at 50 °C.

Cross-plane thermal conductivity of electrodes and separators has been measured using a differential steady state method [52]. The experimental setup is very similar to that of the 1D heat flowmeter previously used [45]. The cross plane thermal conductivity of positive electrode (PE), negative electrode (NE) and separator are measured to be 2.0, 1.06 and 0.19 W/mK respectively in the presence of electrolyte [52].

Cross-plane thermal conductivity of several components and that of a stack of components have also been measured. The measurement is carried out using two different methods. In the first method, thermal conductivity has been measured by ensuring 1D flow of the heat generated in the heater assembly passing through the NE-separator-PE stack. Values in the 0.33 to 0.66 W/mK range have been reported [46]. In the other method, thermal diffusivity is measured using xenon flash technique from which thermal conductivity is extracted by using the heat capacity value measured separately. The out of plane thermal conductivity measurement of the stack is carried out at two different SOCs. The thermal conductivity measured for the stack is 1.90 W/mK and 2.36 W/mK respectively for the OCV values of 2.45 V and 3.75 V. In the presence of electrolyte, these values change somewhat to 3.39 W/mK and 3.40 W/mK respectively. The heat capacity was measured to be 1040 J/kgK and 960 J/kgK respectively for the OCV values 2.45 V and 3.75 V [46]. Similar work has been done to study the effect of cycling on thermal properties of lithium polymer cells [53]. Thermal conductivity and specific heat of the battery components taken out of from a fresh cell and a one cycled 500 times at 45 °C has been reported. The effect of cycling at high temperature on these parameters has been reported [53]. In plane and cross plane thermal conductivity of the anode material has also been measured using transient planar source and laser flash techniques [54, 49].

In addition to these reports of thermal conductivity and heat capacity measurements, thermal contact resistance between cell materials has been reported.

In these experiments, the material stack is sandwiched between two copper blocks, and the total thermal resistance of the stack is measured. Key conclusions made here include lower contact thermal resistance of the wet stack compared to dry stack and weak temperature dependence of the stack resistance [55]. However, the thermal resistances measured here are the total thermal resistances which also includes the material thermal resistance and not just the contact thermal resistances between the battery components. Contact thermal resistance between the electrodes and copper rods used in these experiments have been measured, that is not of particular relevance for in situ operation of the cell.

In another work, interfacial thermal conduction between cathode and separator has been measured using a similar one-dimensional heat flow method. It has been shown that this interfacial resistance dominates over the material thermal resistances from the separator and cathode, offering around 88% of the total thermal resistance. This work concluded that interfacial thermal resistance is the rate-limiting heat transfer process within a Li-ion cell, and originates from the weak van der Waals adhesion between separator and cathode [56]. In addition to these material thermal characterizations, cell level thermal characterization is needed to capture the nature of heat transfer phenomena at the spatial scale of a cell. There have been a few experimental measurements reported in literature for cell level thermal property measurements. Some of these are based on primarily thermal methods [57-60], whereas others are based on the coupling between thermal transport and electrochemical properties [61-62]. It is important for such measurements to account for anisotropy due to the rolled/folded nature of the electrode roll. Lumped and reduced order model based thermal parameter characterizations have also been done [63-64].

An analytical solution based approach has been used where a Li-ion cell is externally heated and the measured transient temperature rise is fitted with an analytical solution to determine the thermal conductivity and specific heat. The radial thermal conductivity is measured to be 0.15-0.2 W/mK for 26650 and 18650 cells. Axial thermal conductivity measurements show the axial thermal conductivity to be 30.4-32.0 W/mK, which represents nearly 150-fold anisotropy [58]. This work also allows simultaneous heat capacity measurement which is determined to be 1605-1720 J/kgK for 26650 and 18650 cells [58]. Another paper with a similar approach reports similar values for thermal conductivities, but a much lower heat capacity, in the range of 814-972 J/kgK [59].

The axial thermal conductivity of a Li-ion cell has also measured using a comparative method to obtain the heat flow through battery indirectly, while preventing heat loss via thermal compensation [57]. The thermal compensation system consist of a heater which reduces radial temperature gradient to minimize radial heat losses. This method is difficult to adapt for radial thermal conductivity measurement. In this work, the radial thermal conductivity was estimated to be around 1.0 W/mK from the known thermal conductivities of the electrode stack components, ignoring thermal contact resistances. Axial thermal conductivity was reported to range from 6.83 to 4.25 W/mK over an entire discharge process [57].

The specific heat capacity and cross-plane thermal conductivity for a 75Ah LFP pouch cell has been measured using an isothermal calorimeter. The influence of SOC and temperature on the specific heat capacity of the LFP cell is considered in modeling and calculations. Over the full temperature range from -5 °C to 55 °C, this property is found to vary by approximately 38%. The cross-plane thermal conductivity is reported to be around 0.42 W/mK, and nearly independent of temperature across the full SOC range [60].

The thermal impedance spectrum of a system – analogous to electrochemical impedance spectrum (EIS) – has been used to provide information about thermal properties of the system [61-62]. Thermal impedance is measured through Laplace transform of the transient temperature rise in response to an external or internal heat pulse. Thermal impedance spectra have been obtained for batteries from different manufacturers and used as validation of this method. The heat capacity and thermal conductivity are obtained from a nonlinear fit of the experimental data with a theoretical impedance function developed for a cylindrical rod with external heat generation. Heat capacity and thermal conductivity of the electrode roll of an 18650 Li-ion cell are measured to be 1900 J/kgK and 1.4W/mK respectively [61]. However, anisotropy in thermal conductivity is not accounted for here. The effect of SOC has also been studied for one of the cells, which indicated slight increase in thermal conductivity with state of charge [61]. Using a similar technique, thermal conductivity and heat capacity of a 4.4Ah $LiFePO_4$ cell have been reported to be 0.35 W/mK and 958 J/kgK respectively [62].

## 1.3. Scope of Current Work

While materials in a Li-ion cell are reasonably well-optimized for electrochemical performance [14-15, 65], relatively lesser research has been carried out to measure, understand and optimize thermal transport within the Li-ion cell materials. Our recent work showed that thermal conduction within the cell is the dominant mechanism in determining the overall thermal performance of the cell, as opposed to heat transfer from outer surface of the cell [66, 67]. Recent measurements on Li-ion cells indicated strong anisotropy in thermal conduction, and a poor thermal conductivity of 0.15-0.20 W/m-K in the direction normal to the electrodes [58]. This value is as poor as that of typical polymers [68]. Thermal conductivity of typical electrode has been reported to be 2-5 W/m-K [46, 47].Other components such as current collectors (copper or aluminum) and anode (graphite) have even higher thermal conductivity. However, overall thermal conductivity is very low as reported above. It is clearly important to understand, identify and improve the material-level origin of this poor thermal conductivity.

As shown in Figure 3.1 (Chapter 3), in this thermal unit cell, thermal properties of anode, cathode and current collector are very well known except for separator. The separator is a critical, multi-functional component of a Li-ion cell that plays a key role in performance and safety during energy conversion and storage processes. Heat flow through the separator is important for minimizing cell temperature and avoiding thermal runaway. In chapter 2 we present the measurements of thermal conductivity and heat capacity of the separator material. These measurements are based on thermal response to an imposed DC heating within a time period during which an assumption of a thermally semi-infinite domain is valid. Experimental data are in excellent agreement with the analytical model. Comparison between the two results in measurement of the in-plane thermal conductivity and heat capacity of the separator. Results indicate very low thermal conductivity of the separator. Measurements at an elevated temperature indicate that thermal conductivity and heat capacity do not change much with increasing temperature. Experimental measurements of previously unavailable thermal properties of the separator reported here are expected to aid in a better fundamental understanding of thermal transport in a Li-ion cell, and enhanced safety due to more accurate thermal prediction.

It is really interesting to note that the overall thermal conductivity of the Li-ion cell is found to be even lower than the lowest thermal conductivity offering material (e.g. separators and electrolyte). In chapter 3, we identify the rate-limiting material-level process that dominates overall thermal conduction in a Li-ion cell. Results indicate that thermal characteristics of a Li-ion cell are largely dominated by heat transfer across the cathode-separator interface rather than heat transfer through the materials themselves. This interfacial thermal resistance contributes around 88% of total thermal resistance in the cell. Measured value of interfacial resistance is close to that obtained from theoretical models that account for weak adhesion and large acoustic mismatch between cathode and separator. Further, to address this problem, an amine-based chemical bridging of the interface is carried out. This is shown to result in four-times lower interfacial thermal resistance without deterioration in electrochemical performance, thereby increasing effective thermal conductivity by three-fold. This improvement is expected to reduce peak temperature rise during operation by 60%. By identifying and addressing the material-level root cause of poor thermal transport in Li-ion cells, this work may contribute towards improved thermal performance of Li-ion cells.

While Gel-Polymer Electrolytes (GPEs) have been widely investigated for use in next-generation Li-ion cells due to the potential for improved thermal safety, thermal transport within a GPE is still poorly understood. Among all materials in a Li-ion cell, the GPE has the lowest thermal conductivity, and hence determines the overall rate of heat flow in a Li-ion cell. This makes it critical to measure and understand thermal transport in a GPE and investigate trade-offs between thermal and ionic transport. Chapter 4 presents measurements of thermal and ionic conductivities in a PVdF-based GPE. The effect of incorporating BN/$Al_2O_3$ ceramic nano/microparticles in the GPE on thermal and ionic transport is characterized. Measurements indicate up to 2.5X improvement in thermal conductivity of activated GPE membranes, with relatively minor effect on electrochemical performance of GPE-based single-layer cells. The measured enhancement in thermal conductivity is in very good agreement with theoretical calculations based on the effective medium theory that accounts for thermal transport in a dispersed, two-phase medium such as a GPE. The fundamental insights gained in this work on thermal transport in a GPE and the role of nano/microparticle inclusions may facilitate thermal-electrochemical optimization and design of GPEs for safe, high-performance Li-ion cells.

## 1.4. References

[1] Scrosati, B., & Garche, J. (2010). Lithium batteries: Status, prospects and future. *Journal of Power Sources*, *195*(9), 2419-2430.

[2] Marsh, R. A., Vukson, S., Surampudi, S., Ratnakumar, B. V., Smart, M. C., Manzo, M., & Dalton, P. J. (2001). Li ion batteries for aerospace applications. *Journal of Power Sources, 97*, 25-27

[3] Linden, D., & Reddy, T. B. (2002). *Handbook of Batteries. 3rd.*

[4] Khaligh, A., & Li, Z. (2010). Battery, ultracapacitor, fuel cell, and hybrid energy storage systems for electric, hybrid electric, fuel cell, and plug-in hybrid electric vehicles: State of the art. *IEEE transactions on Vehicular Technology, 59*(6), 2806-2814.

[5] Franco, J. J. L., Boemo, E., Castillo, E., & Parrilla, L. (2010, March). Ring oscillators as thermal sensors in FPGAs: Experiments in low voltage. *In Programmable Logic Conference (SPL), 2010 VI Southern* (pp. 133-137). IEEE.

[6] Diouf, B., & Pode, R. (2015). Potential of lithium-ion batteries in renewable energy. *Renewable Energy*, *76*, 375-380.

[7] Goodenough, J. B., & Park, K. S. (2013). The Li-ion rechargeable battery: a perspective. *Journal of the American Chemical Society, 135*(4), 1167-1176.

[8] Wang, C. Y., & Srinivasan, V. (2002). Computational battery dynamics (CBD) electrochemical/thermal coupled modeling and multi-scale modeling. *Journal of power sources, 110*(2), 364-376.

[9] Sushko, M. L., Rosso, K. M., Zhang, J. G., & Liu, J. (2011). Multiscale simulations of Li ion conductivity in solid electrolyte. *The Journal of Physical Chemistry Letters, 2*(18), 2352-2356.

[10] Northrop, P. W., Ramadesigan, V., De, S., & Subramanian, V. R. (2011). Coordinate transformation, orthogonal collocation, model reformulation and simulation of electrochemical-thermal behavior of lithium-ion battery stacks. *Journal of the Electrochemical Society, 158*(12), A1461-A1477.

[11] Wang, C. Y., Gu, W. B., & Liaw, B. Y. (1998). Micro-Macroscopic Coupled Modeling of Batteries and Fuel Cells I. Model Development. *Journal of the Electrochemical Society, 145*(10), 3407-3417.

[12] Ouyang, C., Shi, S., Wang, Z., Huang, X., & Chen, L. (2004). First-principles study of Li ion diffusion in $LiFePO_4$. *Physical Review B, 69*(10), 104303.

[13] Stephan, A. M., & Nahm, K. S. (2006). Review on composite polymer electrolytes for lithium batteries. *Polymer*, *47*(16), 5952-5964.

[14] Etacheri, V., Marom, R., Elazari, R., Salitra, G., & Aurbach, D. (2011). Challenges in the development of advanced Li-ion batteries: a review. *Energy & Environmental Science, 4*(9), 3243-3262.

[15] Zhang, S. S. (2007). A review on the separators of liquid electrolyte Li-ion batteries. *Journal of Power Sources, 164*(1), 351-364.

[16] Young, K., Wang, C., Wang, L. Y., & Strunz, K. (2013). Electric vehicle battery technologies. *In Electric Vehicle Integration into Modern Power Networks (pp. 15-56). Springer New York.*

[17] Tarascon, J. M., & Armand, M. (2001). Issues and challenges facing rechargeable lithium batteries. *Nature, 414*(6861), 359-367.

[18] Patil, A., Patil, V., Shin, D. W., Choi, J. W., Paik, D. S., & Yoon, S. J. (2008). Issue and challenges facing rechargeable thin film lithium batteries. *Materials research bulletin, 43*(8), 1913-1942.

[19] Wainwright, D. (1995). *U.S. Patent No. 5,464,705*. Washington, DC: U.S. Patent and Trademark Office.

[20] Lundsgaard, J. S. (1989). *U.S. Patent No. 4,879,190*. Washington, DC: U.S. Patent and Trademark Office.

[21] Besenhard, J. O., & Eichinger, G. (1976). High energy density lithium cells: Part I. Electrolytes and anodes. *Journal of Electroanalytical Chemistry and Interfacial Electrochemistry, 68*(1), 1-18.

[22] Gabano, J. P. (1983). Lithium batteries. *London and New York, Academic Press*, 1983, 467 p.

[23] Murphy, D. W., Christian, P. A., DiSalvo, F. J., & Waszczak, J. V. (1979). Lithium incorporation by vanadium pentoxide. *Inorganic Chemistry, 18*(10), 2800-2803.

[24] Arora, P., & Zhang, Z. (2004). Battery separators. Chemical reviews, 104(10), 4419-4462. [25] Kanno, R., Takeda, Y., Ichikawa, T., Nakanishi, K., & Yamamoto, O. (1989). Carbon as negative electrodes in lithium secondary cells. *Journal of Power Sources, 26*(3-4), 535-543.

[26] Mohri, M., Yanagisawa, N., Tajima, Y., Tanaka, H., Mitate, T., Nakajima, S., Yoshida, M., Yoshimoto, Y., Suzuki, T. & Wada, H. (1989). Rechargeable lithium battery based on pyrolytic carbon as a negative electrode. *Journal of Power Sources*, *26*(3-4), 545-551.

[27] Peled, E., Menachem, C., Bar-Tow, D., & Melman, A. (1996). Improved Graphite Anode for Lithium-Ion Batteries Chemically Bonded Solid

Electrolyte Interface and Nanochannel Formation. *Journal of the Electrochemical Society, 143*(1), L4-L7.

[28] Wakihara, M. (2001). Recent developments in lithium ion batteries. *Materials Science and Engineering: R: Reports, 33*(4), 109-134.

[29] Chen, X., Shen, W., Vo, T. T., Cao, Z., & Kapoor, A. (2012, December). An overview of lithium-ion batteries for electric vehicles. *In IPEC, 2012 Conference on Power & Energy* (pp. 230-235). IEEE.

[30] Rolf, H. (2000). Electronic properties of materials.

[31] Kam, K. C., & Doeff, M. M. (2011). Electrode Materials for Lithium Ion‖ Material Matters, Vol. 7, No. 4,(2012) Electronic Properties of Materials.

[32] van Schalkwijk, W., & Scrosati, B. (Eds.). (2007). *Advances in lithium-ion batteries*. Springer Science & Business Media.

[33] Sloop, S. E., Pugh, J. K., Wang, S., Kerr, J. B., & Kinoshita, K. (2001). Chemical Reactivity of PF 5 and LiPF6 in Ethylene Carbonate/Dimethyl Carbonate Solutions. *Electrochemical and Solid-State Letters, 4*(4), A42-A44.

[34] Kawamura, T., Kimura, A., Egashira, M., Okada, S., & Yamaki, J. I. (2002). Thermal stability of alkyl carbonate mixed-solvent electrolytes for lithium ion cells. *Journal of Power Sources, 104*(2), 260-264.

[35] McCloskey, B. D., Bethune, D. S., Shelby, R. M., Girishkumar, G., & Luntz, A. C. (2011). Solvents' critical role in nonaqueous lithium–oxygen battery electrochemistry. *The Journal of Physical Chemistry Letters, 2*(10), 1161-1166.

[36] Tamura, T., Yoshida, K., Hachida, T., Tsuchiya, M., Nakamura, M., Kazue, Y., Tachikawa, N., Dokko, K.& Watanabe, M. (2010). Physicochemical properties of glyme–Li salt complexes as a new family of room-temperature ionic liquids. *Chemistry letters, 39*(7), 753-755.

[37] Meyer, W. H. (1998). Polymer electrolytes for lithium-ion batteries. *Advanced materials, 10*(6), 439-448.

[38] Stephan, A. M. (2006). Review on gel polymer electrolytes for lithium batteries. *European polymer journal, 42*(1), 21-42.

[39] Song, J. Y., Wang, Y. Y., & Wan, C. C. (1999). Review of gel-type polymer electrolytes for lithium-ion batteries. *Journal of Power Sources, 77*(2), 183-197.

[40] Huang, X., & Hitt, J. (2013). Lithium ion battery separators: development and performance characterization of a composite membrane. *Journal of Membrane Science, 425*, 163-168.

[41] Cho, J.H., Lee, J., Xia, Y., Kim, B., He, Y., Renn, M.J., Lodge, T.P. & Frisbie, C. D. (2008). Printable ion-gel gate dielectrics for low-voltage polymer thin-film transistors on plastic. *Nature materials, 7*(11), 900.

[42] Meng, C., Liu, C., Chen, L., Hu, C., & Fan, S. (2010). Highly flexible and all-solid-state paper like polymer supercapacitors. *Nano letters*, *10*(10), 4025-4031.

[45] Song, L., & Evans, J. W. (1999). Measurements of the thermal conductivity of lithium polymer battery composite cathodes. *Journal of the Electrochemical Society, 146*(3), 869-871.

[46] Maleki, H., Al Hallaj, S., Selman, J. R., Dinwiddie, R. B., & Wang, H. (1999). Thermal Properties of Lithium-Ion Battery and Components. *Journal of the Electrochemical Society, 146*(3), 947-954.

[47] Cho, J., Losego, M.D., Zhang, H.G., Kim, H., Zuo, J., Petrov, I., Cahill, D.G. & Braun, P. V. (2014). Electrochemically tunable thermal conductivity of lithium cobalt oxide. *Nature communications*, *5*, 4035.

[48] Maleki, H., Selman, J. R., Dinwiddie, R. B., & Wang, H. (2001). High thermal conductivity negative electrode material for lithium-ion batteries. *Journal of power sources, 94*(1), 26-35.

[49] Goli, P., Legedza, S., Dhar, A., Salgado, R., Renteria, J., & Balandin, A. A. (2014). Graphene-enhanced hybrid phase change materials for thermal management of Li-ion batteries. *Journal of Power Sources, 248,* 37-43.

[50] Song, L., Chen, Y., & Evans, J. W. (1997). Measurements of the Thermal Conductivity of Poly (Ethylene Oxide) -Lithium Salt Electrolytes. *Journal of the Electrochemical Society, 144*(11), 3797-3800.

[51] Vishwakarma, V., & Jain, A. (2014). Measurement of in-plane thermal conductivity and heat capacity of separator in Li-ion cells using a transient DC heating method. *Journal of Power Sources, 272,* 378-385.

[52] Yang, Y., Huang, X., Cao, Z., & Chen, G. (2016). Thermally conductive separator with hierarchical nano/microstructures for improving thermal management of batteries. *Nano Energy, 22*, 301-309.

[53] Maleki, H., Wang, H., Porter, W., & Hallmark, J. (2014). Li-Ion polymer cells thermal property changes as a function of cycle-life. *Journal of Power Sources*, *263,* 223-230.

[54] Koo, B., Goli, P., Sumant, A.V., dos Santos Claro, P.C., Rajh, T., Johnson, C.S., Balandin, A.A. & Shevchenko, E. V. (2014). Toward lithium ion batteries with enhanced thermal conductivity. *ACS nano, 8*(7), 7202-7207.

[55] Ponnappan, R., & Ravigururajan, T. S. (2004). Contact thermal resistance of Li-ion cell electrode stack. *Journal of power sources*, *129*(1), 7-13.

[56] Vishwakarma, V., Waghela, C., Wei, Z., Prasher, R., Nagpure, S.C., Li, J., Liu, F., Daniel, C. & Jain, A. (2015). Heat transfer enhancement in a lithium-ion cell through improved material-level thermal transport. *Journal of Power Sources*, *300*, 123-131.

[57] Zhang, W., Zhang, X., Wang, C., Yu, G., & Yang, C. (2014). Experimental and Computational Research on the Thermal Conductivities of Li/SOCl2 Batteries. *Journal of the Electrochemical Society*, *161*(5), A675-A681.

[58] Drake, S. J., Wetz, D. A., Ostanek, J. K., Miller, S. P., Heinzel, J. M., & Jain, A. (2014). Measurement of anisotropic thermophysical properties of cylindrical Li-ion cells. *Journal of Power Sources, 252,* 298-304.

[59] Spinner, N. S., Mazurick, R., Brandon, A., Rose-Pehrsson, S. L., & Tuttle, S. G. (2015). Analytical, numerical and experimental determination of thermophysical properties of commercial 18650 LiCoO2 lithium-ion battery. *Journal of the Electrochemical Society*, *162*(14), A2789-A2795.

[60] Bazinski, S. J., & Wang, X. (2015). Experimental study on the influence of temperature and state-of-charge on the thermophysical properties of an LFP pouch cell. *Journal of Power Sources, 293*, 283-291.

[61] Barsoukov, E., Jang, J. H., & Lee, H. (2002). Thermal impedance spectroscopy for Li-ion batteries using heat-pulse response analysis. *Journal of power sources, 109*(2), 313-320.

[62] Fleckenstein, M., Fischer, S., Bohlen, O., & Bäker, B. (2013). Thermal Impedance Spectroscopy-A method for the thermal characterization of high power battery cells. *Journal of Power Sources*, *223*, 259-267.

[63] Forgez, C., Do, D. V., Friedrich, G., Morcrette, M., & Delacourt, C. (2010). Thermal modeling of a cylindrical LiFePO 4/graphite lithium-ion battery. *Journal of Power Sources, 195*(9), 2961-2968.

[64] Kim, Y., Mohan, S., Siegel, J. B., Stefanopoulou, A. G., & Ding, Y. (2014). The estimation of temperature distribution in cylindrical battery cells under unknown cooling conditions. *IEEE Transactions on Control Systems Technology, 22*(6), 2277-2286.

[65] Yuan, L. X., Wang, Z. H., Zhang, W. X., Hu, X. L., Chen, J. T., Huang, Y. H., & Goodenough, J. B. (2011). Development and challenges of LiFePO 4 cathode material for lithium-ion batteries. *Energy & Environmental Science, 4*(2), 269-284.

[66] Shah, K., Drake, S. J., Wetz, D. A., Ostanek, J. K., Miller, S. P., Heinzel, J. M., & Jain, A. (2014). Modeling of steady-state convective cooling of cylindrical Li-ion cells. *Journal of Power Sources, 258,* 374-381.

[67] Shah, K., Drake, S. J., Wetz, D. A., Ostanek, J. K., Miller, S. P., Heinzel, J. M., & Jain, A. (2014). An experimentally validated transient thermal model for cylindrical Li-ion cells. *Journal of Power Sources, 271*, 262-268.

[68] Henry, A. (2013). Thermal transport in polymers. *Annu. Rev. Heat Transfer, 17*, 485-520.

# CHAPTER 2

# THERMOPHYISCAL PROPERTY MEASUREMENT OF SEPARATOR MATERIAL

Vishwakarma, V., & Jain, A. (2014). Measurement of in-plane thermal conductivity and heat capacity of separator in Li-ion cells using a transient DC heating method. Journal of Power Sources, 272, 378-385.

## Abstract

The separator is a critical, multi-functional component of a Li-ion cell that plays a key role in performance and safety during energy conversion and storage processes. Heat flow through the separator is important for minimizing cell temperature and avoiding thermal runaway. Despite the critical nature of thermal conduction through the separator, very little research has been reported on understanding and measuring the thermal conductivity and heat capacity of the separator. This chapter presents first-ever measurements of thermal conductivity and heat capacity of the separator material. These measurements are based on thermal response to an imposed DC heating within a time period during which an assumption of a thermally semi-infinite domain is valid. Experimental data are in excellent agreement with the analytical model. Comparison between the two results in measurement of the in-plane thermal conductivity and heat capacity of the separator. Results indicate very low thermal conductivity of the separator. Measurements at an elevated temperature indicate that thermal conductivity and heat capacity do not change much with increasing temperature. Experimental measurements of previously unavailable thermal properties reported in this work may facilitate a better fundamental understanding of thermal transport in a Li-ion cell, and enhanced safety due to more accurate thermal prediction.

Keywords: Lithium-ion Cells, Separator, Thermal Conductivity, Heat Capacity, Battery Safety, Flexible Substrates.

## 2.1. Introduction

Thin flexible substrates are frequently used in engineering applications such as flexible electronics [1-2], separators for Li-ion cells [3-5], organic semiconductors [6], flexible displays [7-9], etc. Compared to a thick rigid substrate, a flexible substrate offers reduced weight, increased design flexibility, bendability, etc. [10]. In addition, thin substrates also often provide valuable functionality, such as controlled ionic conductance through thin separators in Li-ion cells [3]. The thin, flexible nature of the separator in a Li-ion cell also makes it possible to roll the electrode-separator assembly and compactly package it inside a high energy density cell. [3]. Figure 2.1 shows an image of the electrode-separator roll from a Li-ion cell, and a schematic of various layers in the assembly. The positive electrode is typically made of a transition metal oxide, whereas the negative electrode is typically graphite. Transfer of Li ions from one electrode to another enables charging or discharging of the cell. The two electrodes are typically separated by the separator, which is typically based on an electrically insulating porous material and is about a few tens of microns thick. The separator material plays a multi-functional role [5, 11]. The primary role of the separator is to provide a pathway for Li ions to migrate from one electrode to the other while blocking electron transport [12]. The separator also provides mechanical strength without deterioration at high temperature [13-14] and contributes to conductance of heat generated inside the cell. A number of studies have been carried out for understanding and quantifying ionic conductance through the separator material [5, 11]. A more limited number of studies have investigated mechanical stresses in the separator that may occur during cell operation [13-14, 16]. Despite the importance of thermal transport within the cell, however, there is a lack of literature on measurement, modeling and optimization of thermal transport properties of the separator. Heat generated throughout the cell must conduct through the electrode roll to the outer surface, where it is eventually dissipated to the surroundings. This makes it important to understand the nature of thermal conduction with the cell [17], and rate-limiting steps that determine the effectiveness of this process [18].

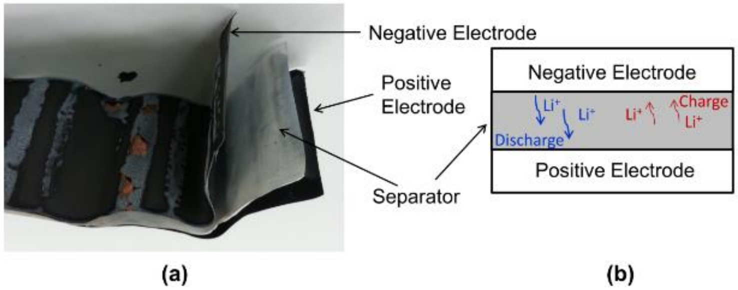

Figure 2.1. (a) Image of the electrode-separator roll in a Li-ion cell; (b) Schematic of various layers in the assembly.

Among all materials in the electrode roll including positive electrode ($LiFePO_4$, $LiCoO_2$, etc.), Negative electrode (graphite), current collectors (metal) and separator, the separator is expected to have the lowest thermal conductivity, and hence must be investigated in detail. In addition, thermal contact resistances between the separator and electrodes may also be important. A number of papers have addressed thermal modeling within a Li-ion cell [19-24]. The accuracy of temperature fields predicted by such models depends critically on the accuracy of underlying thermal properties of constituent materials. There is a lack of experimental data on thermal properties of the separator, and most past work on thermal modeling [19-24] appears to use assumed values for thermal properties of the separator. Given the importance of accurate temperature prediction on battery safety, it is clearly very desirable to experimentally measure these properties. Such a measurement will contribute towards the thermal engineering, and hence operational safety of Li-ion cells. The fundamental governing energy equation, the solution to which determines the temperature distribution within a thermal system is given by [25]

$$k\nabla^2 T + Q''' = \rho C_p \frac{\partial T}{\partial t} \tag{1}$$

where $T$ is the temperature field and $Q'''$ is volumetric heat generation rate. The two fundamental thermophysical properties that appear in this equation, and that play a key role in determining the nature of thermal transport through the separator material are its thermal conductivity, $k$ (W/mK) and specific heat capacity, $C_p$ (J/kgK) [26]. While $k$ determines the rate of thermal conduction through the separator, $C_p$ characterizes the extent of heat storage within the material. The quantity $\frac{k}{\rho C_p}$ is often referred to as the thermal diffusivity, $\alpha$ ($m^2/s$). Note that equation (1) assumes that $k$ is an isotropic property, although in some materials, $k$ may be different in different directions [26].

A number of experimental techniques have been reported in the past for measurement of thermophysical properties of substrates [27-31]. In general, the temperature rise in the material of interest in response to a known heat flux is measured and compared with a theoretical model to determine $k$ and $C_p$. Heat flux is imposed by either Joule heating due to an electric current, or optically through a laser. Methods based on constant, time-varying and periodic heat flux have been used in the past [27]. Two separate experiments are often required to measure both, although two measurements within the same experiment have also been used [29]. A vast amount of literature exists on the measurement of thermophysical properties of thick, rigid substrates, typically a few mm or thicker [27]. In addition, thin films, a few µm or thinner, deposited on a thick, rigid substrate have also been thermally characterized [32]. On the other hand, not much research has been reported on measurement of thermophysical properties of thin, flexible substrates. Neither of the approaches outlined above for rigid substrates or thin films will work for a substrate that is a few tens of µm, such as a typical Li-ion separator. This necessitates a new approach for thermophysical property measurement. A typical separator in a Li-ion cell is a few tens of µm thick [11,16], which presents a challenge in measurement of thermophysical properties.

An additional challenge in the measurement of thermophysical properties of a flexible substrate is in the microfabrication of heater and sensor elements. While microfabrication is carried out commonly on rigid substrates such as Silicon wafers and glass slides [33], fabrication of metal features on a thin flexible substrate is not as well developed. The mechanical stiffness of a typical separator of a Li-ion cell is even less than that of typical substrates used for flexible electronics [1-2].

This chapter presents a novel experimental method for measurement of in-plane thermal conductivity and heat capacity of a Li-ion cell separator. The method is based on measurement of temperature rise in two parallel metal lines during a short time following DC heating in one of the lines. This method is capable of measurement on substrates for which experimental methods for neither thick rigid substrates, nor thin films are applicable. Measurements are in excellent agreement with an analytical model based on the assumption of a semi-infinite domain. Both in-plane thermal conductivity and heat capacity are measured at room temperature and at an elevated temperature. Results from this work are expected to contribute towards better thermal understanding and safety of Li-ion cells. Analytical modeling and experimental method are presented in next two sections, followed by a discussion of results.

## 2.2. Measurement Technique

In this chapter, the thermal response of a thin, flexible separator to DC heating is measured and used to determine its thermophysical properties. Since there are standard methods available for measurement of density, the two thermophysical properties of primary interest here are $k$ and $C_p$. Generally, the measurement of thermal conductivity involves measurement of the steady state temperature difference sustained by a given heat flow through the material of interest. A straight-forward application of this approach is not possible for the thin and flexible separator material. It is difficult to insert standard thermocouples in this material. Similarly, application of a known heat flux is also difficult using standard experimental tools. In this chapter, thin metal heaters and temperature sensors are microfabricated on the flexible substrate, and thermal response to DC Joule heating due to an electric current is measured. Figure 2.2 shows a schematic of the geometry under consideration. Two parallel thin metal lines of length $L$ are fabricated on the flexible substrate of thickness $t_{subs}$. The heater and sensor lines are located at $x$=0 and $x=x_0$ respectively. The heater line bisects the flexible substrate into two halves, each of width w. The separator itself is tethered on a thick, rigid substrate at both ends ($y=\pm L/2$).

Consider the thermal effect of a DC current $I_0$ passing through the heater line, which has an electrical resistance of $R$. The heat generated in the heater line is given by

$$Q_0 = I_0^2 R \tag{2}$$

Assuming that this experiment is carried out in vacuum, no heat loss occurs due to convection. Since the substrate is thin and free-standing, therefore no thermal conduction takes place in the out-of-plane $z$ direction. Since the microheater line is long in the y direction, heat conduction is one-dimensional in x-direction only. Due to symmetry, half of $Q_0$ passes through each half of the substrate bifurcated by the heater line. The governing energy conservation equation in the separator material is given by

$$k\frac{\partial^2 T}{\partial x^2} = \rho C_p \frac{\partial T}{\partial t} \tag{3}$$

where $T$ is the temperature rise above ambient.

The governing equation is subject to the following boundary condition:

$$-k\left.\frac{\partial T}{\partial x}\right|_{x=0} = \frac{Q_0}{2A} = \frac{I_0^2 R}{2Lt_{subs}} \tag{4}$$

In addition, it may be assumed that the initial temperature is zero everywhere, i.e. $T$=0 at $t$=0.

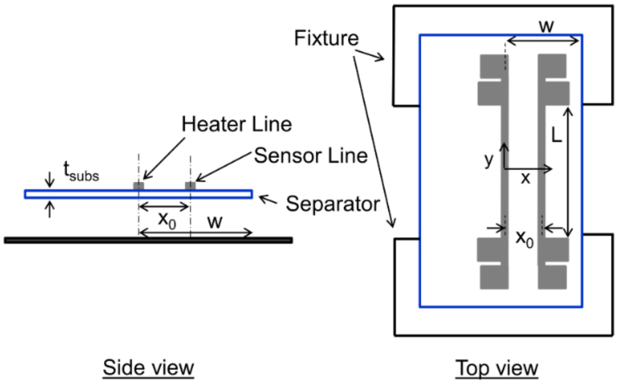

Figure 2.2. Schematic of the geometry under consideration.

A solution for the temperature distribution may be determined assuming the plastic substrate to be a semi-infinite medium for thermal conduction. This assumption is valid as long as the thermal penetration depth for the duration of the experiment, $t_{exp}$ is much lesser than $w$, i.e.

$$2\sqrt{\alpha \cdot t_{\mathrm{exp}}} << w \tag{5}$$

where $\alpha$ is the thermal diffusivity of the sample. Thus, for a given value of $w$, the semi-infinite assumption will be valid as long as the duration of the experiment $t_{exp}$ satisfies

$$t_{\mathrm{exp}} << \frac{w^2}{4\alpha} \tag{6}$$

Under this assumption, the solution for the transient temperature field may be derived by re-writing the energy conservation equation (Equation (3)) in terms of heat flux instead of temperature using Fourier's law. Once written in terms of heat flux, equation (3) can be easily integrated and converted back to temperature [26]. The solution for $T(x,t)$ is found to be

$$T(x,t) = \frac{I_0^2 R}{Ak}\left[\left(\frac{\alpha t}{\pi}\right)^{\frac{1}{2}} e^{-\left(\frac{x}{4\alpha t}\right)} - \frac{x}{2} erfc\left(\frac{x}{\sqrt{4\alpha t}}\right)\right] \tag{7}$$

This expression forms the fundamental basis for measurement of thermal conductivity and heat capacity of the separator.

Equation (7) shows that the difference between temperature of the heater and sensor at any time is given by

$$\Delta T(t) = T(0,t) - T(x_0,t) = \frac{I_0^2 R}{Ak}\left[\left(\frac{\alpha t}{\pi}\right)^{\frac{1}{2}}\left(1 - e^{-\left(\frac{x}{4\alpha t}\right)}\right) - \frac{x}{2} erfc\left(\frac{x}{\sqrt{4\alpha t}}\right)\right] \tag{8}$$

which, for large time, $t >> \frac{x_0^2}{4\alpha}$, reduces to

$$\Delta T\left(t >> \frac{{x_0}^2}{4\alpha}\right) = \frac{I_0^2 R x_0}{2Ak} \tag{9}$$

Thus, at large time, the difference between heater and sensor temperature becomes constant. Measurement of this temperature difference can be used in equation (9) to determine *k*, since all other parameters in the equation are known.

Further, in order to determine the heat capacity of the separator, the variation of the heater temperature alone with time is considered. Equation (7) shows that the temperature at the heater, *x*=0, is given by

$$T_{heater}(t) = T(0,t) = \frac{I_0^2 R}{Ak}\left(\frac{\alpha t}{\pi}\right)^{\frac{1}{2}} \tag{10}$$

Due to the $t^{0.5}$ term in equation (10), a log-log plot of the heater temperature as a function of time is expected to be linear, with a slope of 0.5. In addition, the intercept $M$ of this plot is given by

$$M = \log_{10}\left(\frac{I_0^2 R}{A\sqrt{k\rho C_p \pi}}\right) \tag{11}$$

Equation (11) shows that a measurement of the intercept of log-log plot of temperature as a function of time can be used to determine $k \cdot C_p$, the product of thermal conductivity and volumetric heat capacity of the material, i.e.

$$kC_p = \frac{1}{\rho\pi}\left(\frac{I_0^2 R}{A10^M}\right)^2 \tag{12}$$

Once $k$ is measured from equation (9) using temperature data from the heater and sensor, $C_p$ can be determined from equation (13) using the heater data alone.

Note that there are two distinct requirements on the measurement time based on the requirement for the substrate to act as a semi-infinite medium, equation (6) and based on the requirement for deriving equation (9). Combining the two, it is found that the time duration for this measurement technique has upper and lower bounds given by

$$\frac{x_0^2}{4\alpha} << t << \frac{w^2}{4\alpha} \tag{13}$$

Physically speaking, these requirements arise from the thermal wave generated from the DC current in the heater line to at least reach the sensor line, but still not reach the boundary of the separator material.

Thermal conductivity and heat capacity of the separator from a commercial 26650 Li-ion cell is measured using the technique discussed above. Microfabrication and experimental setup is described in the next section, followed by a discussion of measurement results.

## 2.3. Experiments

### 2.3.1. *Microfabrication and Packaging of Test Samples*

Two Titanium metal lines are deposited in a class-100 cleanroom on a sample of separator extracted from a commercial 26650 Li-ion cell. The separator is extracted from a completely discharged 26650 Li-ion cell, and electrode materials are stripped out. Since the 26650 cell is hermetically sealed, careful attention is given to ensure safe removal of the separator. The disassembly is carried out inside a fume hood. The top of the cell is first pried off, and the casing of the cell is cut down on one side. The casing is slowly peeled back in order to provide complete access to the electrode roll. This material consists of multiple layers – separator, positive electrode, negative electrode, separator, and current collectors. Once removed, the spirally wound layers in the roll are slowly unraveled and placed flat. Layers are allowed to dry for an hour and then are manually detached from one another. The separator material is cut into samples of the desired size. Note that separator samples used in this work do not contain electrolyte, since the focus of this work is measurement of thermal properties of the separator material alone. Presence of electrolyte introduces added complications that must be addressed separately. Understanding and measuring thermal properties of the separator alone is a first step in that direction.

In order to carry out microfabrication of the metal lines on the separator material, a fixture is designed to tightly mount the separator on a rigid surface. The separator is tightly attached to a standard microscope glass slide (Figure 2.3(a)) using double sided tape, and the edges are sealed by single sided tape (Figure 2.3(b)). 0.3 μm Titanium is then deposited using AJA e-beam evaporator followed by photolithography using a negative mask. Metal etching is carried out in 1:1:20 mixture of HF, $H_2O_2$ and DI water respectively (Figure 2.3(c)). Once the microheater is fabricated on the separator, the entire glass slide with separator is submerged in acetone for 10 minutes. This results in release of the separator from the tape (Figure 2.3(d)). Each metal line is 40 μm wide and 1.8 mm long. The lines are connected to two contact pads on each end in order to facilitate four-wire measurements. The high electrical resistivity of Titanium provides the capability of large heat generation. In addition, Titanium also has a large temperature coefficient of resistivity (TCR), making it ideal for use as a temperature sensor.

The separator with microfabricated metal lines is suspended across two microscope coverslips which are mounted on microscope glass slides for ease of handling (Figure 2.3(e)). Contact pads for the heater and sensor lines are then wire bonded with conductive epoxy and left to dry for 3-4 hours. Figure 2.3(f) shows the final microheater device with one heater line and one sensor line.

The microheater device fabricated on the separator is very flexible, and does not lose functionality even when the separator is twisted or bent. Figure 2.4 demonstrates this by wrapping the separator material with metal features on the curved surface of a cylinder. Metal lines are found to be preserved and working even when the separator is significantly curved.

### 2.3.2. *Calibration and Thermophysical Property Measurements*

The microheater device is calibrated in a Boeckel CCC 0.5D incubator. The device is placed inside the incubator, and the temperature is increased from 22 °C to 82 °C in steps of 15°C. At each point, the temperature is allowed to stabilize for 15 minutes before measuring heater resistance. A Keithley 2612A sourcemeter is used to send a small sensing current of 10 μA, and a Keithley 2100 multimeter is used to measure the voltage difference induced across the microheater device. A plot of resistance as a function of temperature provides the required calibration for determining temperature rise during thermophysical property measurement experiments.

Experiments for thermophysical property measurement based on the technique described in section 2.2 are carried out in an evacuated vacuum chamber to eliminate convective heat losses. The temperature rise during each experiment is small enough to rule out radiation as a significant heat loss mechanism. Heating current passing through the heater line is sourced from a Keithley 2612A sourcemeter. A Keithley 2401 sourcemeter is used for sourcing a sensing current of 100 μA through the sensor for temperature measurement. This current is small enough to reliably measure the sensor resistance, and hence temperature without causing significant self-heating.

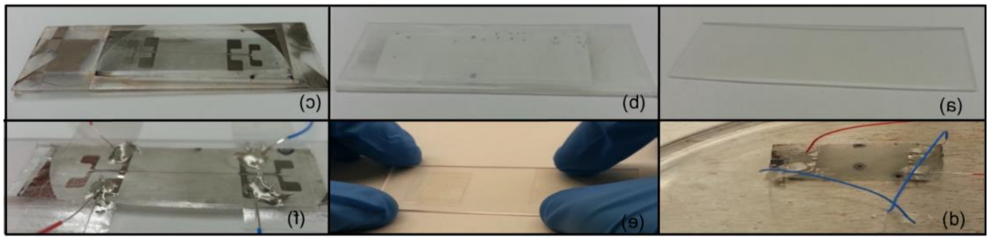

Figure 2.3. Images of steps for microfabrication of microheater device. (a) Attachment to a glass slide, (b) Sealing by single sided tape, (c) Metal deposition and etching, (d) Release of the separator, (e) Attachment on a coverslip-based fixture, (f) Final device with wire bonding.

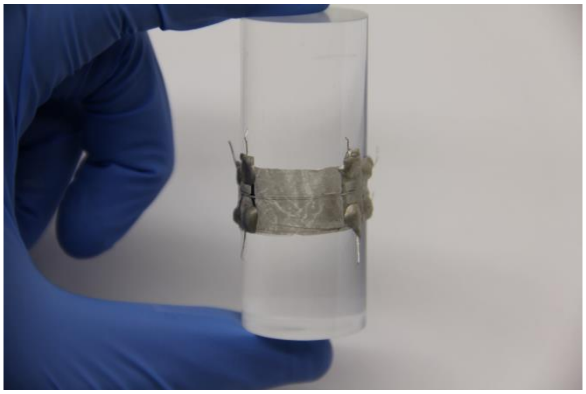

Figure 2.4. Demonstration of flexibility of the device by wrapping the sample with metal features on the curved surface of a cylinder.

A National Instruments NI-9205 cDAQ system controlled by a LabView VI is used to measure and log the heater and sensor voltages. Electrical resistance measured in this fashion is converted to temperature rise using calibration data. While the difference between the heater and sensor temperatures is used to determine *k*, the heater temperature alone is used to determine $C_p$, once *k* is known.

## 2.4. Results and Discussion

### 2.4.1. *Heater and Sensor Calibration, and Density Measurement*

Measurements of heater and sensor electrical resistances as functions of temperature are shown in Figure 2.5. The heater and sensor resistances are close to each other, and both exhibit a linear increase with temperature with nearly the same slope. This is expected since the heater and sensor lines are geometrically identical, and made from the same material in the same process. The measured value of thermal coefficient of resistance (TCR) for the heater and sensor is found to be 0.0022 and 0.0023 $K^{-1}$ respectively, which are both close to the theoretically expected value of 0.0026 $K^{-1}$ [34]. The measured slopes of these curves are used to determine heater and sensor temperatures from measured electrical resistance during experiments described in sections 2.4.2 and 2.4.3.

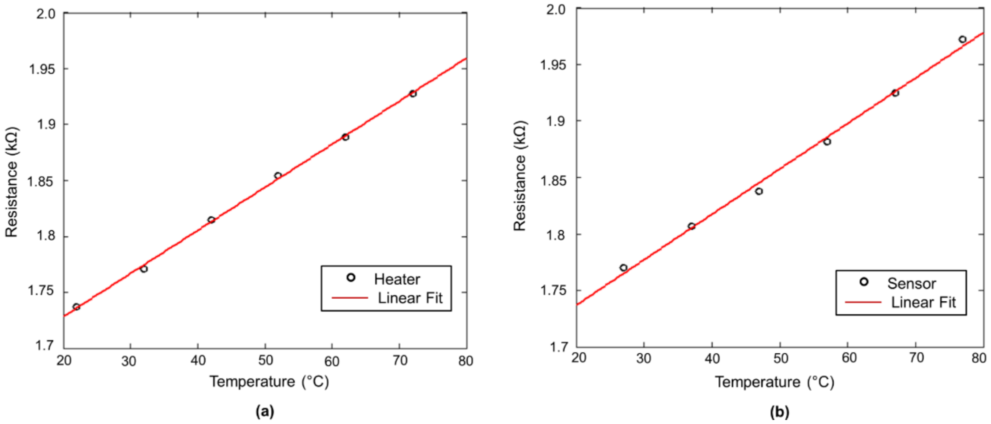

(a)

(b)

Figure 2.5. Temperature calibration plots for (a) Heater line; (b) Sensor line.

In order to measure the density of the separator, the thickness of a sample of known dimensions is measured by determining the step change across a sample adhered on a glass slide using a StepIQ profilometer. The sample mass is measured using a Sartorius 1712 MP balance. Using these measurements, the density of the separator is found to be 913±18 kg/m$^3$.

### 2.4.2. *k Measurements*

Figure 2.6 plots the measured temperature rise in the heater and sensor lines as a function of time for 4.6 mA heating current. The temperature difference

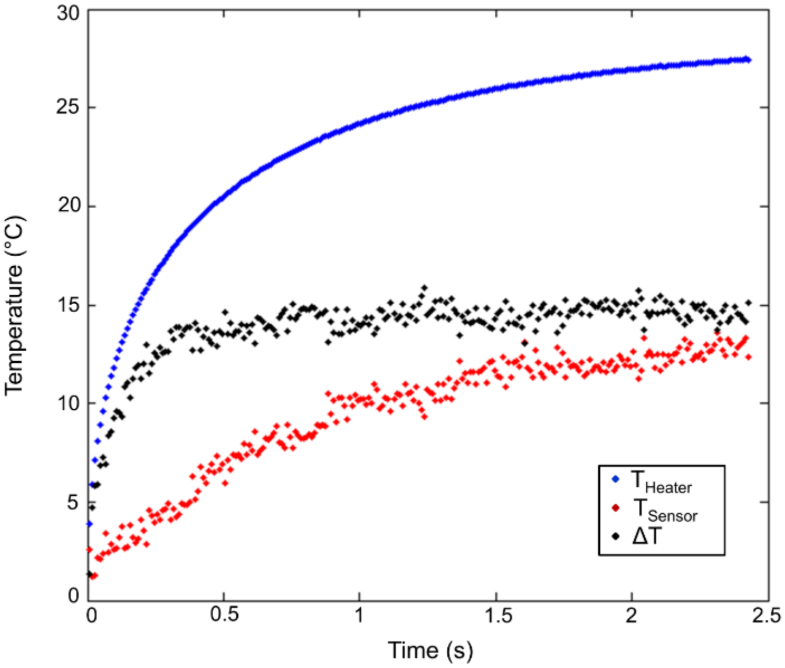

Figure 2.6. Measured temperature rise in the heater and sensor lines as a function of time for 4.6 mA heating current.

between the two is also plotted. As expected from the theoretical model, the heater temperature initially rises faster than the sensor temperature. After some time following the start of DC heating, the difference between the two stabilizes, as expected from equation (9). It takes roughly 0.50 s for the temperature difference to stabilize, which is consistent with the lower limit predicted by equation (13).

This experiment is repeated at a number of heating currents. At each current, the temperature difference stabilizes within the expected time, and the temperature difference at this time is used to determine $k$ from equation (9). The thermal conductivity is measured to be 0.50 ±0.03 W/mK. The measured room temperature thermal conductivity is close to the values assumed in previous papers on thermal analysis of Li-ion cells [19-24], although these papers are not completely clear about the source of the values used.

Note that equation (9) shows that a plot of $\Delta T$ at large time as a function of $I_0^2$ is expected to be linear, with a slope $S_k$ given by

$$S_k = \left( \frac{R x_0}{2Ak} \right) \tag{14}$$

Figure 2.7 plots the temperature difference between heater and sensor at large time as a function of the square of the heating current. As expected from equation (14), this curve is found to be linear. This shows that the experimental data is in good agreement with the analytical model presented in Section 2.2.

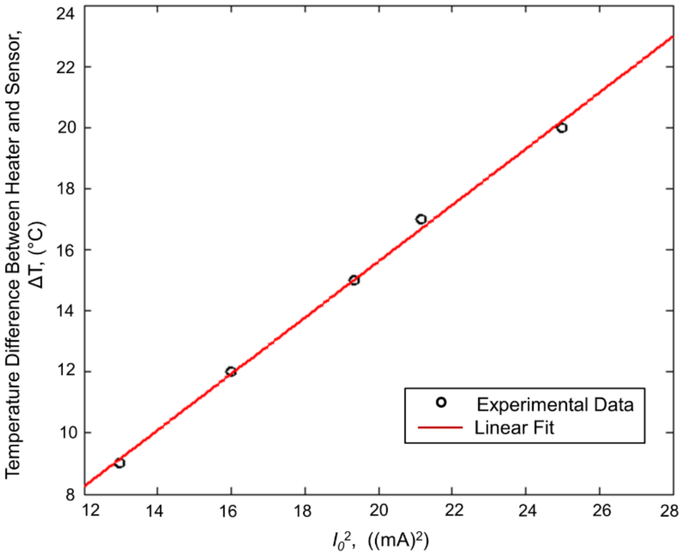

Figure 2.7. Plot showing temperature difference between heater and sensor at large time as a function of the square of the heating current

### 2.4.3. *$C_p$ Measurements*

Figure 2.8 presents a log-log plot of the measured temperature rise in the heater for 4.6 mA heating current as a function of time up to around 2.0 s. As predicted by the analytical model, a linear fit with slope of 0.50, also shown in Figure 8 is in good agreement with experimental data. The intercept of the data can be used to determine $C_p$ based on equation (12). This experiment is also repeated at a number of heating currents. Figure 2.9 plots the combined data. At each current, there is good agreement between experimental data and the analytical model that predicts the data to lie along a line of slope 0.50. The value of heat capacity determined from these experiments is 2480 ±200 kJ/kgK.

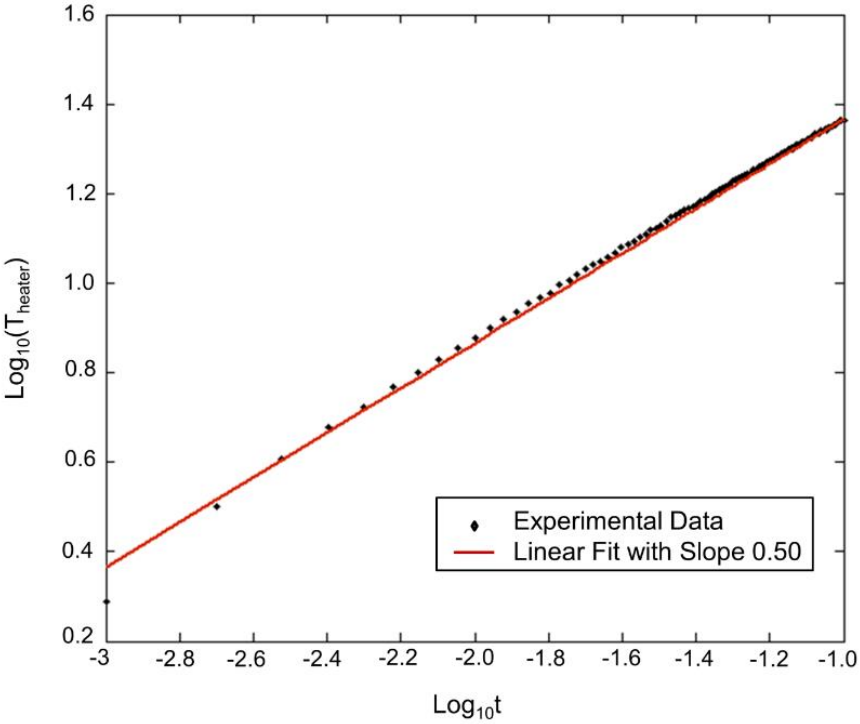

Fig. 2.8. Log-log plot of the measured temperature rise in the heater as a function of time for 4.6 mA.

Equation (15) shows that a plot of $10^M$ as a function of $I_0^2$ is expected to be linear, with a slope given by

$$S_{Cp} = \frac{R}{A\sqrt{kC_p\rho\pi}} \tag{15}$$

Figure 2.10 plots $10^M$ as a function of $I_0^2$. As expected from equation (15), this curve is linear, showing that the experimental data agrees well with the analytical model for heat capacity measurement.

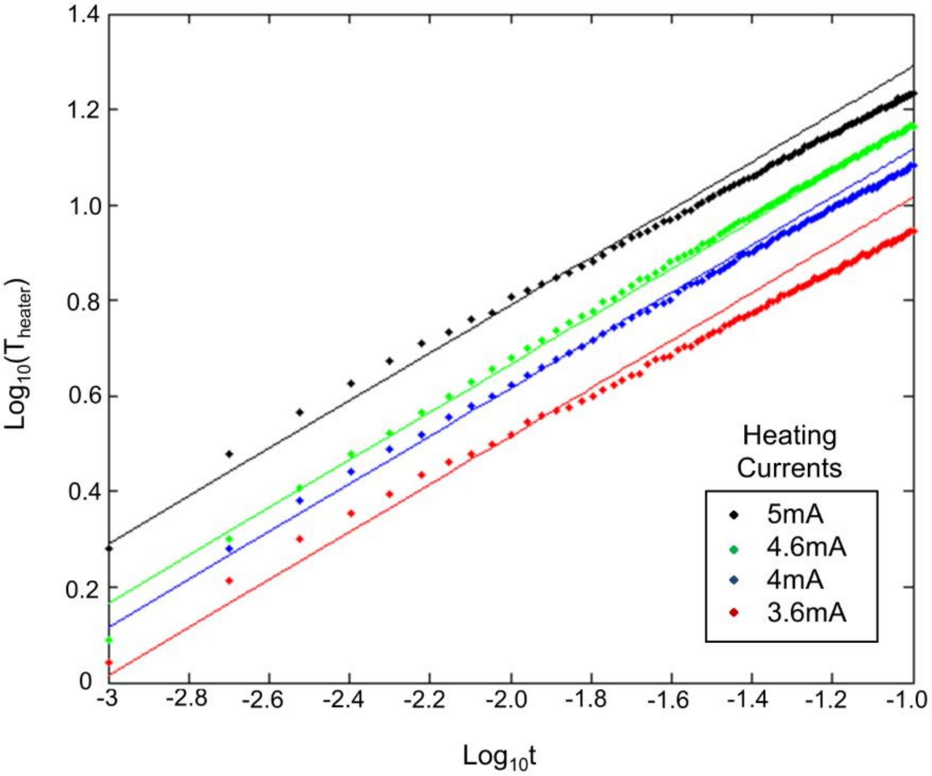

Figure 2.9. Log-log plot of the measured temperature rise in the heater for multiple currents with linear fits.

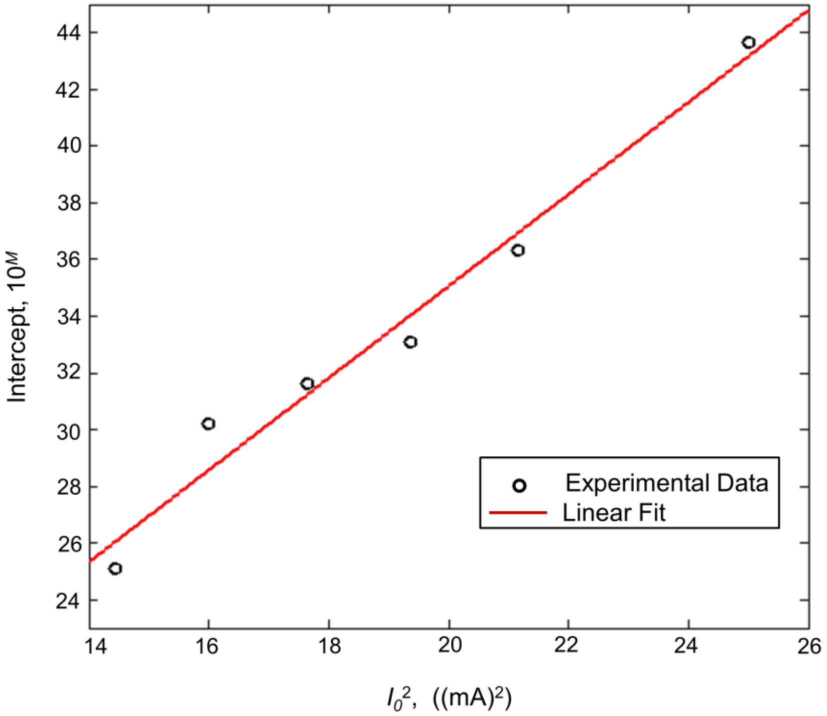

Figure 2.10. Plot of intercept of log-log plots as a function of the square of the heating current

In order to further compare experimental data with the theoretical discussion in section 2.2, the heater temperature is measured for a very long time. This data, plotted on a log-log scale is presented in Figure 2.11. It is found that for approximately the first 3.0 seconds, the plot fits closely with a line of slope 0.5. Beyond this time, the experimental data deviates from the 0.5 slope line, and the rate of increase in temperature is much lower than before. This is consistent with the discussion in section 2.2, which shows that there is an upper limit in time beyond which the semi-infinite assumption is no more valid.

Table 2.1 compares measured *k* and $C_p$ at room temperature with values assumed by previous papers on thermal modeling [19-24]. Heat capacity values for polyethylene reported by Gaur, *et al.* [35] are close to the present measurements, although the material used in that work is in bulk form, and may be different in morphology from the separator of a Li-ion cell. The measured thermal conductivity in this work is slightly higher than the recently measured overall cell-level radial thermal conductivity [17], which indicates the additional impedance to heat flow may be occurring due to thermal contact resistance at interfaces between various materials in the electrode-separator stack.

### 2.4.4. *k and $C_p$ Measurements at High Temperature*

Thermal performance of the separator is particularly important at high temperature. Ineffective heat dissipation during high temperature operation may result in heat buildup and temperature rise, which may eventually lead to a thermal runaway situation. As a result, it is important to understand and measure thermal properties of the separator at high temperature. The experiments described in previous sections are repeated in a 50 °C ambient with all other experimental conditions being the same as previous experiments. Table 2.2 summarizes the room temperature (25 °C) and high temperature (50 °C) measurements of thermal conductivity and heat capacity. It is found that there is negligible change in both thermal conductivity and heat capacity between 25 °C and 50 °C. The small change in the properties between these temperatures is within the measurement error. As a result, thermal conductivity and heat capacity of separator material in a Li-ion cell may be assumed to be independent of temperature in the range of interest for modeling and simulation of thermal performance and safety of Li-ion cells.

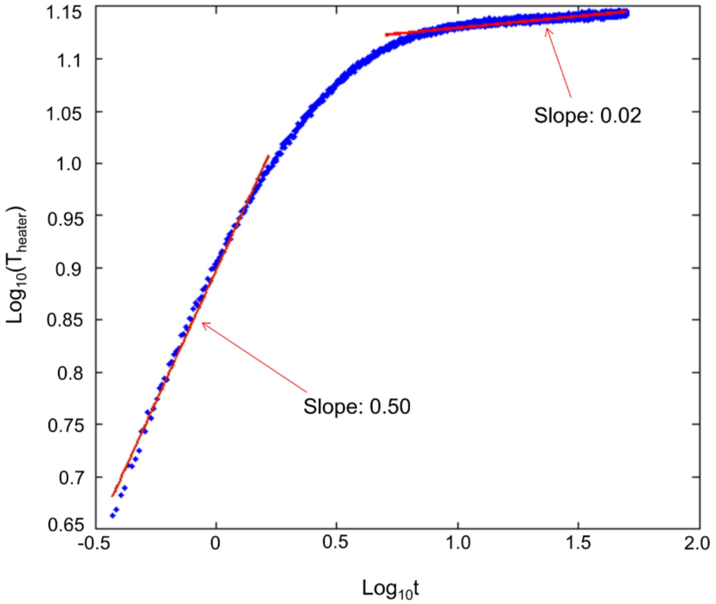

Figure 2.11. Log-log plot of the measured temperature rise in the heater for a large time duration.

Table 2.1. Comparison of measured $k$ and $C_p$ at room temperature with values assumed by previous papers on thermal modeling.

|  | Chen, *et al.* [22] | Wei *et al.* [21] | Peyman & Bahrami [20] | Kim *et al.* [23] | Current Work |
|---|---|---|---|---|---|
| $k$ (W/m.K) | 0.3344 | 1.29 | 0.34 | 1.0 | 0.5±0.03 |
| $C_p$ (J/kg.K) | 1978 | 1839 | 1987 | 700 | 2480±300 |
| $\rho$ (kg/m$^3$) | 1008.98 | 1043 | 1017 | 1200 | 913 ±18 |

### 2.4.5. Experimental Error Analysis

The main sources of experimental error in the measurement of $k$ and $C_p$ arise from measurement of the cross-section area A of the separator. Other errors, including instrument least count errors, etc. are negligible. Based on a relative error analysis, the experimental errors in thermal conductivity and heat capacity measurements are estimated to be 6% and 12% respectively. The error in heat capacity measurement is greater, since heat capacity is determined based on the measurement of $k$, and thus, relative error in measuring $k$ also contributes towards relative error in $C_p$, in addition to other sources of error.

## 2.5. Conclusions

The separator material is expected to have the lowest thermal conductivity among all materials in the electrode stack of a Li-ion cell. This work presents a novel experimental method to measure the in-plane thermal conductivity and heat capacity of the separator from a Li-ion cell. Experimental data from this measurement method, based on a thermally semi-infinite domain in the separator, are found to be in excellent agreement with the underlying theoretical model. Data suggest that the separator has poor thermal conductivity, which does not change significantly at higher temperature. Measurements presented in this chapter contribute towards the understanding of thermal conduction within a Li-ion cell, and provide useful thermal property data that has so far been missing from the literature for a material of much importance for ensuring safety and performance of Li-ion cells.

Table 2.2. Measured thermal conductivity and heat capacity of Li-ion cell separator at room temperature and at elevated temperature.

| | $k$ ($Wm^{-1}K^{-1}$) | $C_p$ ($J\ kg^{-1}K^{-1}$) |
|---|---|---|
| Room Temperature (25 °C) | 0.50±0.03 | 2480±300 |
| Elevated Temperature (50 °C) | 0.43±0.03 | 2470±300 |

## 2.6. Acknowledgments

Microfabrication described in this chapter was carried out at the Nanotechnology Research and Education Center at the University of Texas, Arlington.

## 2.7. References

[1] Sun, Y., & Rogers, J. A. (2007). Inorganic semiconductors for flexible electronics. *Advanced materials, 19*(15), 1897-1916.

[2] Wong, W. S., Chabinyc, M. L., Ng, T. N., & Salleo, A. (2009). Materials and novel patterning methods for flexible electronics. *In Flexible Electronics* (pp. 143-181). Springer US.

[3] Armand, M., & Tarascon, J. M. (2008). Building better batteries. *Nature, 451*(7179), 652-657.

[4] Scrosati, B., & Garche, J. (2010). Lithium batteries: Status, prospects and future. *Journal of Power Sources*, *195*(9), 2419-2430.

[5] Etacheri, V., Marom, R., Elazari, R., Salitra, G., & Aurbach, D. (2011). Challenges in the development of advanced Li-ion batteries: a review. *Energy & Environmental Science, 4*(9), 3243-3262.

[6] Forrest, S. R. (2004). The path to ubiquitous and low-cost organic electronic appliances on plastic. *Nature, 428*(6986), 911-918.

[7] MacDonald, W. A., Looney, M. K., MacKerron, D., Eveson, R., Adam, R., Hashimoto, K., & Rakos, K. (2007). Latest advances in substrates for flexible electronics. *Journal of the Society for Information Display, 15*(12), 1075-1083.

[8] Rogers, J. A., Bao, Z., Baldwin, K., Dodabalapur, A., Crone, B., Raju, V. R., Kuck, V., Katz, H., Amundson, K., Ewing, J., Drzaic, P. (2001). Like electronic displays: Large-area rubber-stamped plastic sheets of electronics and microencapsulated electrophoretic inks. *Proceedings of the National Academy of Sciences, 98*(9), 4835-4840.

[9] Chen, Y., Au, J., Kazlas, P., Ritenour, A., Gates, H., & McCreary, M. (2003). Electronic paper: Flexible active-matrix electronic ink display. *Nature, 423*(6936), 136-136.

[10] Tao, X. (Ed.). (2005). Wearable electronics and photonics. *Elsevier.*

[11] Zhang, S. S. (2007). A review on the separators of liquid electrolyte Li-ion batteries. *Journal of Power Sources, 164*(1), 351-364.

[12] Harris, S. J., Timmons, A., Baker, D. R., & Monroe, C. (2010). Direct in situ measurements of Li transport in Li-ion battery negative electrodes. *Chemical Physics Letters, 485*(4), 265-274.

[13] Xiao, X., Wu, W., & Huang, X. (2010). A multi-scale approach for the stress analysis of polymeric separators in a lithium-ion battery. *Journal of Power Sources, 195*(22), 7649-7660.

[14] Christensen, J. (2010). Modeling diffusion-induced stress in Li-ion cells with porous electrodes. Journal of the Electrochemical Society, 157(3), A366-A380. [15] Wang, Q., Ping, P., Zhao, X., Chu, G., Sun, J., & Chen, C. (2012). Thermal runaway caused fire and explosion of lithium ion battery. *Journal of power sources, 208*, 210-224.

[16] Venugopal, G., Moore, J., Howard, J., & Pendalwar, S. (1999). Characterization of microporous separators for lithium-ion batteries. *Journal of Power Sources, 77*(1), 34-41.

[17] Drake, S. J., Wetz, D. A., Ostanek, J. K., Miller, S. P., Heinzel, J. M., & Jain, A. (2014). Measurement of anisotropic thermophysical properties of cylindrical Li-ion cells. *Journal of Power Sources, 252*, 298-304.

[18] Shah, K., Drake, S. J., Wetz, D. A., Ostanek, J. K., Miller, S. P., Heinzel, J. M., & Jain, A. (2014). Modeling of steady-state convective cooling of cylindrical Li-ion cells. *Journal of Power Sources, 258,* 374-381.

[20] Taheri, P., & Bahrami, M. (2012). Temperature rise in prismatic polymer lithium-ion batteries: An analytic approach. S*AE International Journal of Passenger Cars-Electronic and Electrical Systems, 5*(2012-01-0334), 164-176.

[21] Wu, W., Xiao, X., & Huang, X. (2011, January). Modeling heat generation in a lithium ion battery. *In ASME 2011 5th International Conference on Energy Sustainability* (pp. 1513-1522). American Society of Mechanical Engineers.

[22] Chen, S. C., Wan, C. C., & Wang, Y. Y. (2005). Thermal analysis of lithium-ion batteries. *Journal of Power Sources, 140*(1), 111-124.

[23] Kim, U. S., Shin, C. B., & Kim, C. S. (2009). Modeling for the scale-up of a lithium-ion polymer battery. *Journal of Power Sources, 189*(1), 841-846.

[24] Kwon, K. H., Shin, C. B., Kang, T. H., & Kim, C. S. (2006). A two-dimensional modeling of a lithium-polymer battery. *Journal of Power Sources*, *163*(1), 151-157.

[25] Incropera, F. P., & Dewitt, D. P. Introduction to Heat Transfer (1996). *John Whey & Sons. New York. NY.*

[26] Özışık, M. N. (1993). Heat conduction. *John Wiley & Sons.*

[27] Cahill, D. G., Goodson, K., & Majumdar, A. (2002). Thermometry and thermal transport in micro/nanoscale solid-state devices and structures. *Journal of Heat Transfer*, *124*(2), 223-241.

[28] Shi, L., LI, D., Yu, C., Jang, W., Kim, D., Yao, Z., Kim, P. & Majumdar, A. (2003). Measuring thermal and thermoelectric properties of one-dimensional nanostructures using a microfabricated device. *Journal of heat transfer*, *125*(5), 881-888.

[29] Jain, A., & Goodson, K. E. (2008). Measurement of the thermal conductivity and heat capacity of freestanding shape memory thin films using the 3ω method. *Journal of Heat Transfer*, *130*(10), 102402.

[30] Cahill, D. G. (1990). Thermal conductivity measurement from 30 to 750 K: the 3ω method. *Review of scientific instruments, 61*(2), 802-808.

[31] Kurabayashi, K., Asheghi, M., Touzelbaev, M., & Goodson, K. E. (1999). Measurement of the thermal conductivity anisotropy in polyimide films. *Journal of microelectromechanical systems, 8*(2), 180-191.

[32] Cahill, D. G., Katiyar, M., & Abelson, J. R. (1994). Thermal conductivity of a-Si: H thin films. *Physical review B, 50*(9), 6077.

[33] Kovacs, G. T. (1998). Micromachined transducers sourcebook (pp. 586-587). *New York: WCB/McGraw-Hill*.

[34] Donachie, M. J. (2000). Titanium: a technical guide. *ASM international*.

[35] Gaur, U., & Wunderlich, B. (1981). Heat capacity and other thermodynamic properties of linear macromolecules. II. *Polyethylene. Journal of Physical and Chemical Reference Data, 10*(1), 119-152.

# CHAPTER 3

# HEAT TRANSFER ENHANCEMENT IN A LITHIUM-ION CELL

Vishwakarma, V., Waghela, C., Wei, Z., Prasher, R., Nagpure, S. C., Li, J., Liu, F., & Jain, A. (2015). Heat transfer enhancement in a lithium-ion cell through improved material-level thermal transport. *Journal of Power Sources, 300*, 123-131.

## Abstract

While Li-ion cells offer excellent electrochemical performance for several applications including electric vehicles, they also exhibit poor thermal transport characteristics, resulting in reduced performance, overheating and thermal runaway. Inadequate heat removal from Li-ion cells originates from poor thermal conductance within the cell. This work identifies the rate-limiting material-level process that dominates overall thermal conduction in a Li-ion cell. Results indicate that thermal characteristics of a Li-ion cell are largely dominated by heat transfer across the cathode-separator interface rather than heat transfer through the materials themselves. This interfacial thermal resistance contributes around 88% of total thermal resistance in the cell. Measured value of interfacial resistance is close to that obtained from theoretical models that account for weak adhesion and large acoustic mismatch between cathode and separator. Further, to address this problem, we enhance the adhesion of this interface using amine-based chemical bridging. This results in four-times lower interfacial thermal resistance without deterioration in electrochemical performance, thereby increasing effective thermal conductivity by three-fold. This improvement is expected to reduce peak temperature rise during operation by 60%. By identifying and addressing the material-level root cause of

poor thermal transport in Li-ion cells, this work may contribute towards improved thermal performance of Li-ion cells.

Keywords: Li-ion Cell; Thermal Management; Heat Transfer; Interfacial Thermal Conductance; Thermal Runaway.

## 3.1. Introduction

Inadequate heat removal in Li-ion battery cells [1-3] is a key technological challenge needed to be overcome for widespread adoption of electric vehicles (EVs) [4-5]. Despite excellent energy storage and conversion characteristics [1-3] Li-ion cells continue to suffer from poor heat dissipation. Inefficient heat dissipation and overheating in a Li-ion cell directly affects performance and reliability, in addition to presenting significant safety concerns related to thermal runaway [3-4]. A full charging of an EV battery pack within a few minutes is likely to generate significant amount of heat [6], which may be a limiting factor in the goal of fast charging of EVs. Even though the heat generation rate in a Li-ion cell is not particularly high (for example, around 4W for a 26650 cell undergoing 6C discharge [6]), its poor thermal conductivity [7] results in large temperature rise and thermal gradients within the cell [8-9], leading, in extreme cases, to a thermal runaway situation [3, 10]. In order to maintain the cell temperature within safe limits, performance is often sacrificed by operating the cell less aggressively than it could be, overdesigning the battery pack and providing an elaborate external cooling system [5, 11]. Each of these measures results in reduced performance and reliability, and does not address the root cause of inefficient thermal dissipation.

Despite the importance of thermal transport in Li-ion cells, a fundamental understanding of underlying mechanisms is lacking. While materials in a Li-ion cell are reasonably well-optimized for electrochemical performance [12-14], relatively lesser research has been carried out to measure, understand and optimize thermal transport within the Li-ion cell materials. Our recent work showed that thermal conduction within the cell is the dominant mechanism in determining the overall thermal performance of the cell, as opposed to heat transfer from outer surface of the cell [8-9]. Our recent measurements on Li-ion cells indicated strong anisotropy in thermal conduction, and a poor thermal conductivity of 0.15-0.20 W/mK in the direction normal to the electrodes [7]. This value is as poor as that of typical polymers [15]. It is clearly important to understand and improve the material-level origin of this poor thermal conductivity. Thermal conductivity of typical electrode and separator materials measured separately is around 2-5 W/m-K [16-18] and 0.3-1.0 W/m-K [19-21] respectively. Other components such as current collectors (copper or aluminum) and anode (graphite) have even higher thermal conductivity. Using a simple series resistance model that accounts for only material thermal conductivities, the effective thermal conductivity of the thermal unit cell in the direction normal to electrode surface is found to be around 1.76 W/mK, about 8 times higher than the experimentally measured cell-level thermal conductivity of a 18650 and 26650 Li-ion cells [7]. This suggests that thermal transport in a Li-ion cell may be dominated by interface thermal resistance between materials rather than thermal resistance of the materials themselves. This may be occurring in a Li-ion cell because separator and electrodes are merely pressed on to each other during cell manufacturing, which is likely to result in poor surface adhesion and hence large thermal contact resistance [22]. Dominance of thermal conduction processes by interfacial thermal resistance is encountered in other microsystems as well, including microelectronics and microelectromechanical systems (MEMS) [23-25].

Figure 3.1A shows a cut-out of a typical Li-ion cell, indicating the spirally wound stack of electrodes, separator and current collectors. While in-plane heat flow can occur along high thermal conductivity materials, such as current collectors, heat flow in the out-of-plane direction of the stack must conduct through each of these materials as well as through their interfaces before it can be convected away from the outer surface of the cell. The thermal unit cell that repeats itself in the direction normal to the electrode surface is shown in Figure 3.1B. The unit cell comprises multiple layers of anode, cathode, separator and current collectors, and offers various material and interfacial thermal resistances associated with these materials. Note that the anode/cathode materials are coated on both sides of the current collectors. In order to improve cell-level thermal performance, it is critical to measure the thermal resistances in this unit cell, and identify and improve the dominant, rate-limiting steps in the thermal conduction process.

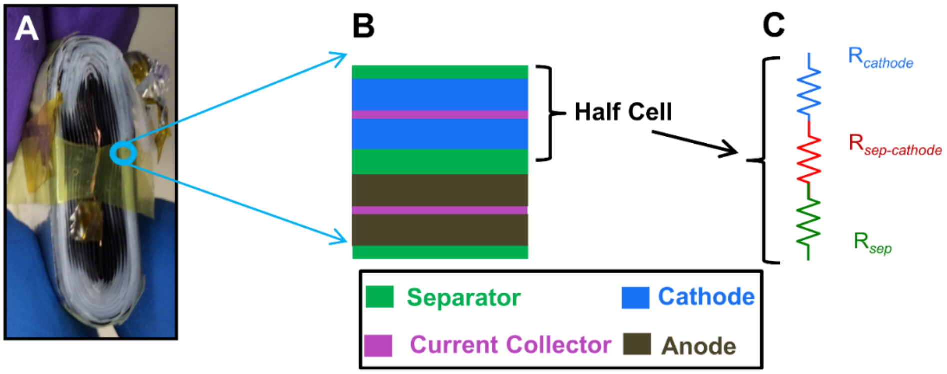

Figure 3.1. Thermal transport in the spiral geometry of a Li-ion cell: (A) Image of the spiral geometry of the electrode-separator roll extracted from a prismatic Li-ion cell; (B) Basic thermal unit cell that repeats itself in the direction normal to the electrode surface, and comprises of various material and interfacial thermal resistances; (C) Thermal resistances in the cathode-side half-cell considered in this work.

In this chapter, we show that thermal conduction within this thermal unit cell is dominated by a large thermal contact resistance (TCR) at the separator-cathode interface, contributing around 88% of total thermal resistance and temperature rise. On the other hand, TCR at the anode-separator interface is negligible. Our measured TCR correctly predicts the recently reported [7] poor cell-level thermal conductivity of Li-ion cells despite the large thermal conductivities of constituent materials. We show that the large TCR is caused by weak adhesion between the separator and cathode materials. Dominance of the TCR shows that improving thermal conductivity of electrode or separator is unlikely to result in significant enhancement in overall thermal performance. We demonstrate 4X improvement in thermal contact resistance by chemically bridging the interface with amine chemistry [23, 26-27] without affecting electrochemical performance of the cell. This improvement is expected to result in more than 3X improvement in cell-level thermal conductivity and 60% reduction in peak temperature rise during cell operation at 7C discharge rate. By identifying and alleviating the rate-limiting process in thermal conduction in a Li-ion cell, this work provides the technological basis for significantly reducing the overheating problem in Li-ion cells, resulting in improved performance, safety and reliability.

## 3.2. Experimental Methods

### 3.2.1. *Electrode and Separator Sample Preparation*

Positive electrode ($LiCoO_2$) and separator are extracted from 18650 commercial Li-ion batteries. The cell is first discharged completely. The metal casing enclosing the spirally-wound electrodes and separator is opened in a laminar flow fume hood. Separator and positive electrode are peeled off carefully from the separator–electrode stack. All experiments are carried out on these materials extracted from a 18650 cell, and not on the 18650 cell itself.

### 3.2.2. *Thermal Measurements*

Total thermal resistance across a material stack is determined by sandwiching the stack between two identical copper blocks [28]. Figure 3.2 shows a schematic of the experimental setup. A picture is also shown in the inset in Figure 3.3. The faces of the copper blocks are polished, first with a 120 grit sandpaper belt on a LECO BG-30 polisher, and then with a 1200 grit sandpaper embedded with 0.05 µm alumina microparticles on LECO Vp-150 polisher. In one of the blocks, heat is generated using a thin Kapton heater affixed on one of the faces. Heat is removed from the other block using cooling water from a chiller passing through a 1 mm diameter through-hole drilled close to one of the faces. Temperature measurement is carried out using T-type thermocouples inserted in seven holes of 1.0 mm diameter in each block. The holes are spaced closer to each other near the surfaces contacting the material stack for greater accuracy near the stack. Holes are drilled in the horizontal plane, which minimizes heat loss down the thermocouple wires. Omega CC High Temperature cement is used to ensure good thermal contact between thermocouple tips and the copper block. The copper blocks are then insulated on all faces except the ones contacting the material stack to minimize stray heat losses. Kapton heater attached to the top block is electrically heated using a power source. Since the electrical resistance of the heater does not vary appreciably in the temperature range of interest, it serves as a source of constant heat flux throughout the experiment.

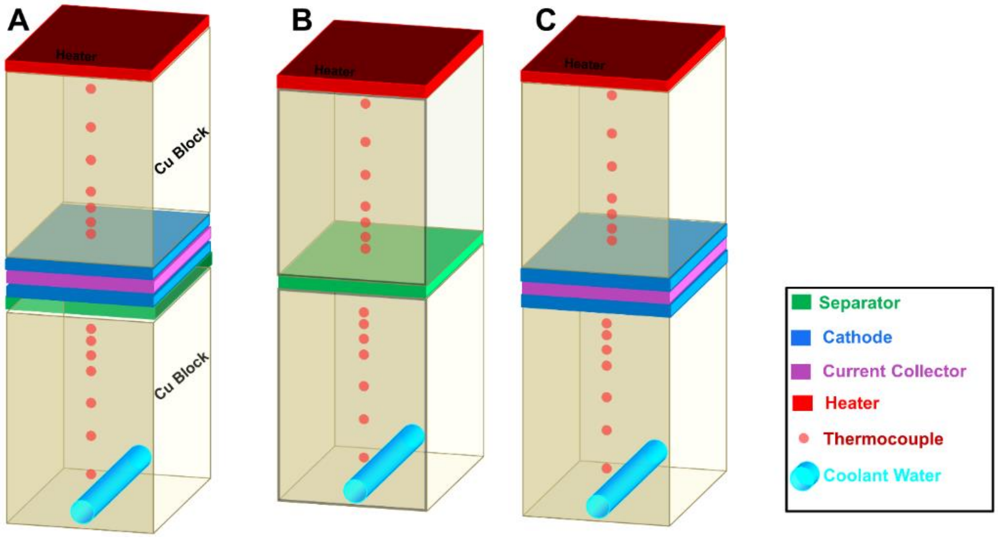

Figure 3.2. Schematics of three steady state temperature gradient based experiments. A (A) separator-electrode stack (Experiment 1), (B) single separator (Experiment 2), and (C) single cathode foil (Experiment 3) was placed between two copper blocks to determine various material and interface thermal resistances through measurement of total thermal resistance

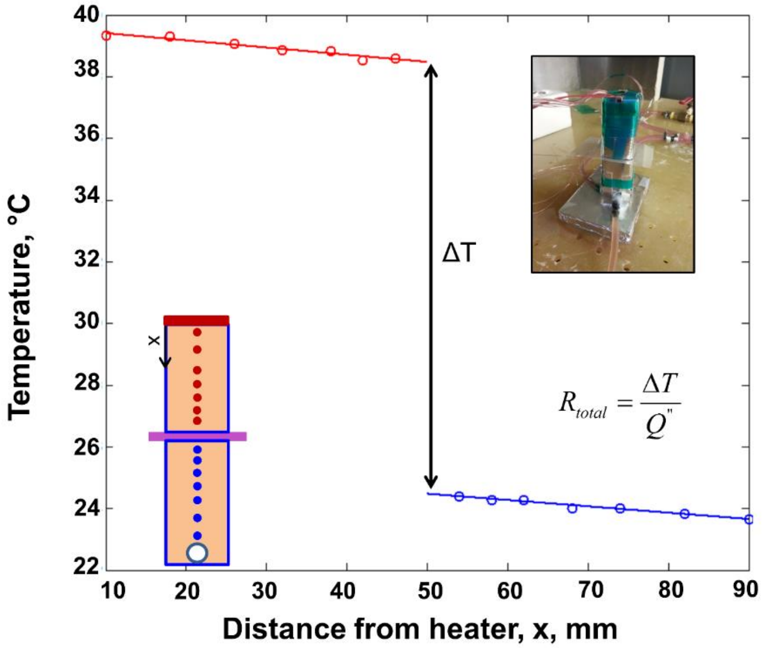

Figure 3.3. Measured temperature data from various thermocouples embedded in the copper blocks for Experiment 1. Extrapolated temperature difference determines temperature drop across the sample under test, and slope of the plot determines the heat flux. This results in measurement of total thermal resistance.

A Keithley 2100 digital multimeter is used to monitor voltage across the heater. Thermocouple temperature measurements are recorded using a National Instruments 9213 DAQ and LabView software with 1 Hz frequency. The experiment continues until steady state is reached. Steady-state temperature measurements from embedded thermocouples are extrapolated to determine the temperature drop across the sample. Heat flux passing through the blocks is determined from the slope of the temperature curve in the copper blocks. Total thermal resistance of the material stack is determined from the ratio of temperature drop and heat flux.

### 3.2.3. *Electrochemical Testing*

A split flat cell with active area of 2.54 $cm^2$ from MTI Corp. is employed for electrochemical testing. The baseline and modified cathodes, together with commercial Celgard 2500 separators and lithium anodes extracted from a 18650 cell as described in Section 3.2.1 are used as cell components. During assembly of the cell in a controlled atmosphere glove box, additional home-made 1.0 M $LiPF_6$ in mixed solvents of ethylene carbonate (EC)-dimethyl carbonate (DMC) (1:1 by volume) is added to compensate for electrolyte loss. After being kept at rest for 24 hours, the cell is first charged at 1.5 mA (roughly corresponding to a rate of 0.33 C) until the voltage reached 4.0 V, then was held at a constant voltage of 4.0 V for 30 minutes, followed by a second period of rest for 20 minutes. After that, the cell is discharged at 1.5 mA until the voltage dropped below 2.5 V. EIS experiments are conducted over a frequency range from 0.1 mHz to 100 MHz at open circuit with an amplitude of 10 mV while the cells are fully discharged. Both battery performance and EIS tests are performed on a Parstat 2273 potentiostat/galvanostat.

### 3.2.4. *Surface Modification*

In order to enhance interfacial thermal conductance, surface modification is carried out on both cathode and separator surfaces. The separator is subjected to oxygen plasma in Micro-RIE Series 800 Plasma System for 5-10 min at 30mTorr. Surface modification of cathode is carried out using amine chemistry [27]. Extracted cathode sample, after wash and dry is immersed into a 2% v/v solution of (3-Aminopropyl)triethoxysilane in ethanol, and left for incubation for 30 minutes at room temperature. This forms an amine self-assembled monolayer (SAM).

## 3.3. Theoretical Modeling for Electrode-Separator TCR

Multiple features of the cathode-separator interface must be accounted for in determining the interfacial thermal contact resistance: a) Large acoustic mismatch between cathode and separator, b) Weak adhesion between cathode and separator, c) Large porosity of separator resulting in reduction in effective area of contact, and, d) Further reduction in area of contact [29], due to the fibrous nature of the separator (~1 µm fiber diameter) [30]. The baseline contact conductance per unit area (g) between two material surfaces is given by [31]

$$g = \Gamma \cdot \frac{c \cdot v}{2} \tag{1}$$

where $\Gamma$ is the integrated phonon transmissivity, $c$ the specific heat for polyethylene and $v$ is the speed of phonons in polyethylene. Since the phonon speed is smaller in polyethylene, conductance must be calculated from the polyethyelene side, wherein $\Gamma$ is integrated till the critical angle. The conductance shown in equation (1) is valid only for interface between two flat substrates. This conductance is scaled to account for porosity and non-flat nature of the substrate. The effective thermal contact conductance is thus given by

$$g = \frac{a}{R} \cdot \phi \cdot \Gamma \cdot \frac{c \cdot v}{2} \tag{2}$$

where $\phi$ is the porosity, $a$ is the contact width and R is the radius of the fiber. $a$ is computed using the well-known Johnson-Kendall-Roberts adhesion mechanics model [32] for cylinders [33]. $R$ is assumed to be 1 μm in these calculations (typical radius of fibers in the separator [34]). Porosity is assumed to be 50%.

Note that critical angle of refraction for $LiCoO_2$ and Polyethylene interface is very low due to large mismatch in phonon speed, which is expected to result in very high interface resistance. On the other hand, the critical angle between graphite (anode) and polyethylene is much larger as the phonon speeds are much closer. Therefore, the contact conductance is expected to be much higher for this interface compared to $LiCoO_2$/Polyethylene interface.

## 3.4. Results and Discussion

### 3.4.1. *TCR Measurement*

The thermal unit cell shown in Figure 3.1B comprises of two half-cells, one each on the anode and cathode sides. The material thermal resistances in the two half-cells are expected to be similar to each other, due to the relatively similar values of thermal conductivity of anode and cathode materials [16-18, 35]. However, theoretical modeling results discussed in section 4.2 show that thermal contact resistance between anode and separator, $R_{sep\text{-}anode}$ is two orders of magnitude lower than thermal contact resistance between cathode and separator, $R_{sep\text{-}cathode}$. As a result, the overall thermal conductivity of the entire unit cell is expected to be dominated by the thermal resistance of the cathode-side half-cell. Consequently, we focus on measurement and reduction of total thermal resistance of the cathode half-cell, shown in Figure 3.1B. The total thermal resistance of the cathode half-cell is given by

$$R_{total} = \frac{L_{sep}}{k_{sep}} + 2 \cdot R_{sep-cathode} + \frac{L_{cathode}}{k_{cathode}} + \frac{L_{cc}}{k_{cc}} + 2 \cdot R_{cathode\text{-}cc} \qquad (3)$$

where subscripts *sep* and *cc* refer to the separator and current collector respectively, $L$ and $k$ are thickness and thermal conductivity respectively. $R_{sep\text{-}cathode}$ and $R_{cathode\text{-}cc}$ refer to the thermal contact resistances at the separator-cathode and cathode-current collector interfaces respectively. Note that $R_{sep\text{-}cathode}$ must be considered twice due to two cathode-separator interfaces in the unit cell.

We have neglected the contribution of the electrolyte to thermal transport. To verify this assumption, we carried out cell-level measurements on commercial 18650 Li-ion cells [7], which included electrolyte inside the cell. Our cell level thermal conductivity with electrolyte present matched with thermal conductivity determined from material-level measurements reported here.

Within the various thermal resistances shown in equation (3), $L_{cc}/k_{cc}$ is expected to be very small (estimated 0.05-0.1 $\mu Km^2/W$) due to the large thermal conductivity of current collector – typically made of copper or aluminum. Further, since the cathode material is coated directly on to the current collector foil, therefore, the two are in intimate thermal contact, with negligible thermal contact resistance compared to the interface between separator and cathode, which are merely pressed on to each other during cell manufacturing. As a result, the three dominant thermal resistances in this half-cell are expected to be the material resistance through cathode, material resistance through separator, and thermal contact resistance between cathode and separator (Figure 3.1C).

We carry out a series of measurements based on one-dimensional, steady-state, out-of-plane thermal conduction to determine these thermal resistances. In experiment 1, a separator-electrode stack is sandwiched between two copper blocks (Figure 3.2A). One of the blocks is heated using a Kapton heater, and the other is cooled using water flow, resulting in the setting up of linear one-dimensional heat flow through the sandwiched material. Figure 3.3 shows the steady-state temperature distribution measured using thermocouples for Experiment 1.

Figure S1 (Chapter 3 Appendix 1) shows temperature measurement from one of the thermocouples as a function of time. Only steady-state measurements are used here, since at steady-state, all of the heat passing through the top copper block conducts across the sample. Total thermal resistance, $R_{total}$ through the separator-electrode stack is determined by extrapolating these temperature measurements and dividing by the heat flux flowing through the stack. In this case, the total thermal resistance is given by

$$R_{total} = R_{Cu-sep} + \frac{L_{sep}}{k_{sep}} + R_{Cu-cathode} + \frac{L_{cathode}}{k_{cathode}} + R_{sep-cathode} \tag{4}$$

where, as noted prior, thermal resistance through the current collector and the cathode-current collector interface is negligibly small.

Thermal conductivities of cathode and separator materials have been measured in the past [16-19]. Based on a value of 0.5 W/mK for the separator thermal conductivity reported by two of the co-authors [19], the material thermal resistance for the separator is found to be $L_{sep}/k_{sep}$=50 µKm$^2$/W. Based on thermal measurements on various cathode materials [16-18], the cathode thermal conductivity is assumed to be 5.4 W/mK. As a result, the material thermal resistance of the cathode is around 11 µKm$^2$/W, which is even lower than the thermal resistance of the separator.

In contrast to material thermal resistances, the thermal contact resistances appearing in equation (4) are largely unknown. While $R_{Cu\text{-}sep}$ and $R_{Cu\text{-}cathode}$ occur due to the experimental setup, $R_{sep\text{-}cathode}$ is intrinsic to the Li-ion material stack. We carried out two sets of experiments, shown in Figures 3.2B and 3.2C to determine these thermal contact resistances.

In order to determine, $R_{Cu\text{-}sep}$, the contact resistance between copper block and separator, the total thermal resistance across a single separator sample sandwiched between copper blocks is measured (Experiment 2, shown in Figure 3.2B). Since there are two interfaces between copper and separator, the total resistance in this case is given by

$$R_{total} = 2R_{Cu-sep} + \frac{L_{sep}}{k_{sep}} \tag{5}$$

Measurement of $R_{total}$, together with the material thermal resistance of the separator based on prior measurements, results in $R_{Cu\text{-}sep}$ = 625 µKm$^2$/W from equation (5).

In Experiment 3, a cathode sample coated on both sides of a current collector is sandwiched between the copper blocks (Figure 3.2C). In this case, the total thermal resistance is given by

$$R_{total} = 2 \cdot R_{Cu-cathode} + \frac{L_{cathode}}{k_{cathode}} \tag{6}$$

where, similar to Experiment 1, we neglect the thermal resistance due to the current collector and the thermal contact resistance between cathode and current collector.

Using recently reported values for thermal conductivity of the cathode [16-18] together with measurement of $R_{total}$ for Experiment 3, we determine the thermal contact resistance $R_{Cu\text{-}cathode}$ to be 345 µKm$^2$/W.

Experiments 2 and 3 provide two of the thermal contact resistances appearing in equation (4), leaving only the thermal contact resistance between separator and cathode as an unknown. Thus, a measurement of the total thermal resistance of the separator-cathode stack in Experiment 1 can be used to determine

$R_{sep\text{-}cathode}$. This value is found to be 420 μKm$^2$/W, much larger than the material resistances due to separator and cathode.

These experiments provide measurements of all thermal resistances involved in the cathode-side half-cell shown in Figure 3.1B. Left side of Figure 3.4 summarizes the contributions of these thermal resistance terms to total thermal resistance. Note that the interface thermal resistance $R_{sep\text{-}cathode}$ must be accounted for twice since there are two separator-cathode interfaces in the unit cell. In addition, the unit cell also comprises two separator layers. Our measurements indicate that thermal contact resistance between separator and cathode dominates the thermal conduction process, accounting for around 88% of the total thermal resistance of the unit cell. Consequently, material-level optimization of thermal transport in a Li-ion cell must focus on this rate-limiting process by improving thermal contact between these two materials. Merely improving material thermal conductivities of separator and/or electrodes without addressing conduction through the interface [37] is unlikely to result in significantly improved overall thermal performance. For example, doubling the separator or cathode thermal conductivity results in only 4.4% and 0.5% reduction in total thermal resistance respectively. It is imperative, instead, to improve the thermal contact resistance between cathode and separator.

### 3.4.2. *Theoretical Modeling Results*

Material properties used for the calculation of thermal contact resistance are listed in Table 1. The baseline thermal contact resistance calculated using Acoustic Mismatch Model (AMM) [36] based on properties of the cathode and separator is 1.1 μKm$^2$/W. We account for the other effects listed in section 3.3 through the following analysis: we assume that the separator is in contact with the cathode through weak van der Waals adhesion due to the two being merely pressed against each other during the Li-ion cell manufacturing process. Prasher *et al.* has shown [31] that weak adhesion leads to dramatic reduction in transmissivity of phonons at the interface leading to high interface resistance. For van der waals adhesion, the adhesion energy is around 50 mJ/m$^2$ [34]. The transmissivity of phonons for this adhesion energy is 10 to 20 times lower than that of AMM [32] computed for a strongly bonded interface. Accounting for this effect results in thermal contact resistance in the range of 11–22 μKm$^2$/W. Furthermore, assuming 50% porous separator [12], the expected thermal contact resistance increases to 22–44 μKm$^2$/W.

Finally, since the separator is made of polymer fibers only the deformed part of the fiber due to adhesive forces participates in heat transfer [29]. This deformed part effectively creates a nano-constriction through which heat must conduct. The area of the deformed part is calculated using Johnson-Kendall-Roberts theory [32] for cylinders [33].

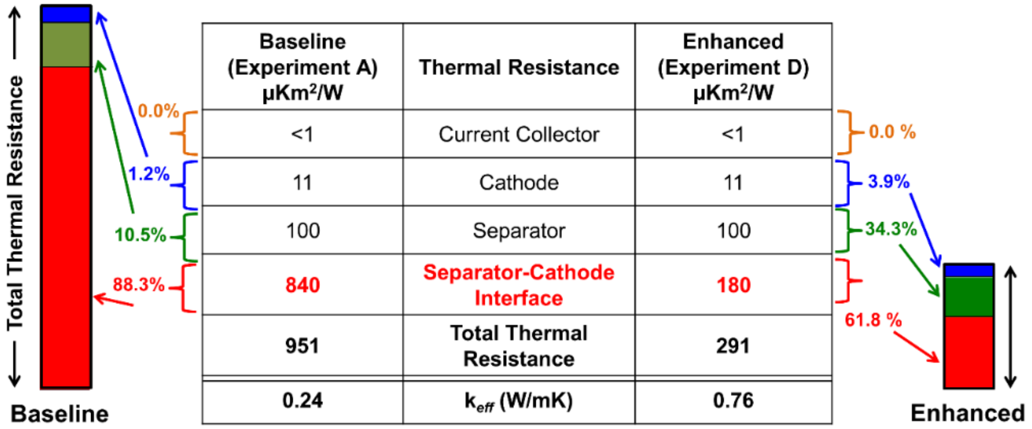

| Baseline (Experiment A) μKm$^2$/W | Thermal Resistance | Enhanced (Experiment D) μKm$^2$/W |
|---|---|---|
| <1 | Current Collector | <1 |
| 11 | Cathode | 11 |
| 100 | Separator | 100 |
| **840** | **Separator-Cathode Interface** | **180** |
| **951** | **Total Thermal Resistance** | **291** |
| **0.24** | **$k_{eff}$ (W/mK)** | **0.76** |

Figure 3.4. Summary of material-level thermal resistances in thermal unit cell of a Li-ion cell in baseline (Experiment A) and enhanced experiments (Experiment D). Color bars show relative magnitudes of various resistances. Note that resistances due to the separator-cathode interface and separator must be counted twice in determining the total thermal resistance of the unit cell. $k_{eff}$ refers to the effective thermal conductivity of the unit cell, including interface thermal resistances. The materials and surface modifications for Experiments A and D are discussed in Figure 3.5.

Table 3.1. Thermal and mechanical properties for various materials for theoretical calculation of thermal contact resistance Note that since the calculation of thermal contact resistance was done from the Polyethylene side, only the heat capacity of Polyethylene is needed.

| Material | Effective speed of sound (m/s) | Mass density (g/cm$^3$) | Heat capacity (J/m$^3$ °C) | Young's modulus (GPa) | Poisson's ratio |
|---|---|---|---|---|---|
| $LiCoO_2$ [18] | 5020 | 5.06 |  | 174 | 0.38 |
| Polyethylene [40] | 672 | 0.95 | 1824000 | 0.7 | 0.42 |
| Graphite [35] | 1940 | 2.26 |  | 33 | 0.33 |

Based on the properties of polypropylene, the ratio of width of this constriction and radius of the fiber is 0.084, i.e. the effective contact resistance increases by a factor of 1/0.084 = 11.85. Using this number, the thermal contact resistance between cathode and separator is found to be in the range of 260–520 μKm$^2$/W which is very close to the experimental measurements discussed in section 3.4.1. On the other hand, due to much larger critical angle between anode and separator compared to the cathode-separator interface, the thermal contact resistance between anode and separator is found to be in the range of 2–4 μKm$^2$/W, which represents around two orders of magnitude greater thermal contact conductance than the cathode–separator interface. This shows that the anode-separator interface plays an insignificant role in determining overall thermal performance of the unit cell.

### 3.4.3. *TCR Enhancement*

In order to improve thermal dissipation in a Li-ion cell by reducing the dominant thermal resistance, we carry out experiments to investigate improved thermal adhesion between the separator and cathode through surface treatment. This is motivated by past work by Kaur *et al.* [23] in which improved adhesion between surfaces using chemical surface modification led to significant decrease in thermal contact resistance [23]. It is well known that thermal contact resistance is correlated with surface adhesion energy [22-23], which is the lowest for van der Waals based adhesion, and can be improved through chemically bridging the

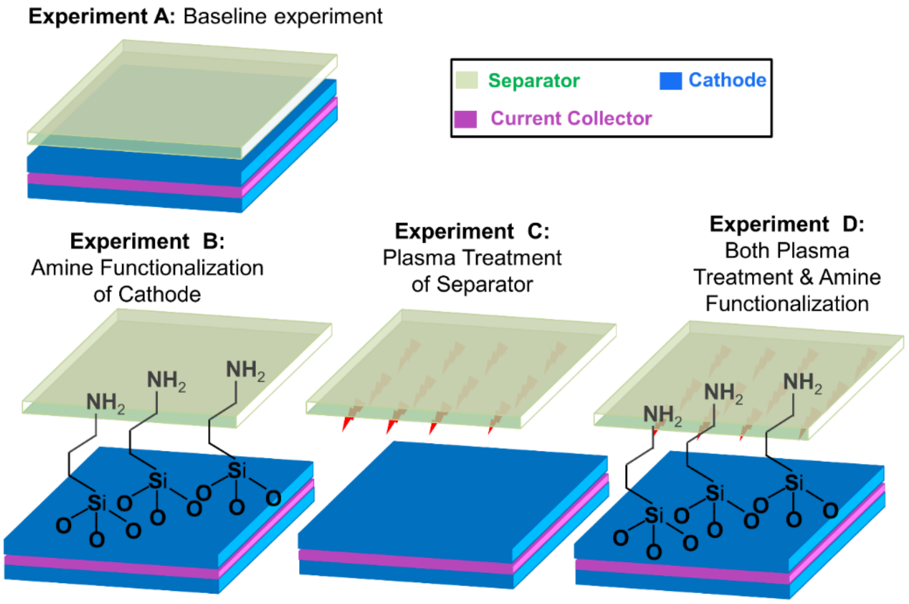

Figure 3.5. Schematic showing the baseline experiment and various surface chemistry modifications explored for understanding the effect on thermal contact resistance between cathode and separator.

interface. Three experiments are carried out as illustrated in Figure 3.5. Our experiments are based on a self-assembled monolayer of amine groups on the cathode surface, and plasma treatment of the separator. Amine groups are commonly used for functionalizing glass surfaces with DNA and other biomolecules [26-27]. Plasma treatment of the separator was motivated by well-known enhancement of surface adhesion of polymers and other materials caused by plasma treatment [38-39]. Four experiments that combine surface modification with plasma treatment, as shown schematically in Figure 3.5 are carried out. Experiment A is the baseline case. In Experiments B and C, surface modification of cathode and plasma treatment of separator are carried out, respectively. In Experiment D, both are carried out. In each case, we measure the resulting thermal contact resistance between the separator and cathode using the technique described in section 3.2.2. Figure 3.6 plots the steady-state temperature measurements from each thermocouple in the experimental setup for Experiments A-D. For each case, the temperature drop across the separator-electrode sample, and hence total thermal resistance is obtained by extrapolation of data shown in Figure 3.6. Starting from the imposition of Joule heating on the experimental setup, temperature drop across the sample increases with time, and eventually reaches a steady-state, as shown in Supplementary Figure S2 (Chapter 3 Appendix 1).

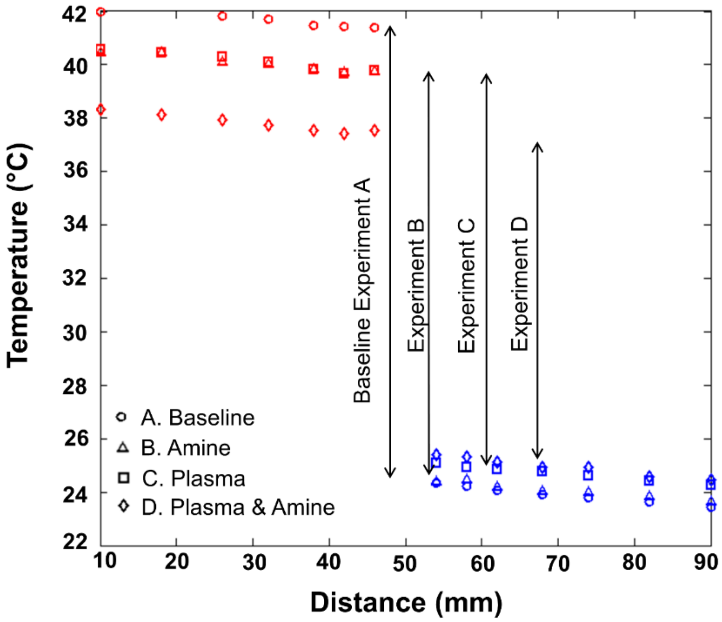

Figure 3.6. Comparison of the steady-state temperature response of baseline and three surface-modified separator-cathode stacks showing reduction in $R_{total}$. Note that the same heat flux is applied in each case. Once thermal contact resistance to copper blocks is subtracted out, the reduction in $R_{sep\text{-}cathode}$ due to surface treatment is even more significant.

Only the steady-state temperature difference is considered, since heat is being stored in the copper blocks prior to steady state, due to which the temperature difference across the sample does not accurately reflect its thermal resistance. Data presented in Figure 3.6 shows significant reduction in total thermal contact resistance due to surface modification. When the material resistances and contact resistances with the copper blocks are subtracted out, similar to previous section, $R_{sep\text{-}cathode}$ was found to reduce by 26%, 41% and 78% compared to baseline measurements for experiments B, C and D respectively. The largest reduction is found when both separator and cathode surfaces are treated (Experiment D), in which case, the measured TCR of 90 μKm$^2$/W is 4X lower than the baseline case, as shown on the right side of Figure 3.4. The total thermal resistance of the unit cell reduces from 951 μKm$^2$/W to 291 μKm$^2$/W. This extent of TCR reduction is consistent with 4X and 6X reduction reported by O'Brien, *et al.* [22] and Kaur, *et al.* [23] respectively, using an organic bonding layer across Cu/$SiO_2$ interface, and amine-terminated carbon nanotubes respectively.

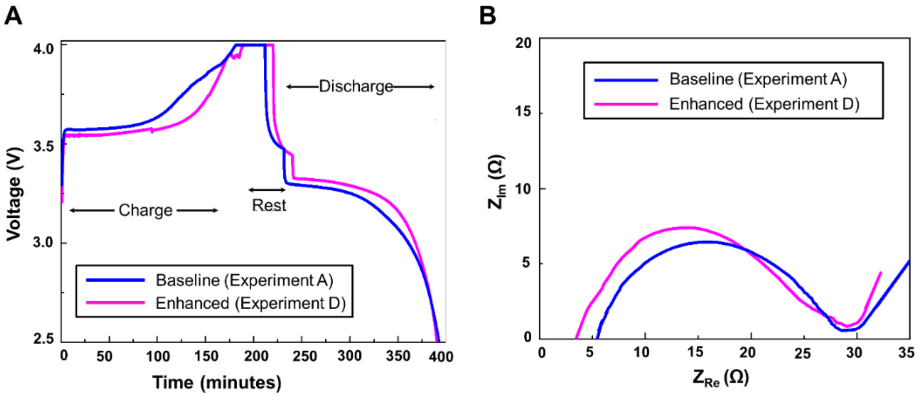

Figure 3.7. Electrochemical evaluation of the baseline and thermally enhanced cathodes in a half-coin cell format with a Lithium counter electrode: (a) charge-discharge performance at 1.5 mA, and (b) Electrochemical Impedance Spectroscopy (EIS) spectra taken at fully discharge state. A split flat cell with active area of 2.54 cm$^2$ was assembled using Lithium anodes.

By reducing the thermal resistance responsible for the largest contribution to overall thermal conduction in the Li-ion cell, the surface modification results in improved overall thermal conductance of the thermal unit cell, as summarized on the right side of Figure 3.4.

In order to investigate the effect of surface modification of the cathode on battery performance, electrochemical tests are performed in a split flat cell. Figure 3.7A shows the complete charge-rest-discharge curves for the baseline (Experiment A) and modified (Experiment D) electrodes. The charging potential is about 32 mV lower than the baseline, and the discharge potential is about 37 mV higher than the baseline, indicating more available energy and higher round trip energy efficiency. This may be due to lower interfacial impedance. The voltage efficiency, evaluated by the ratio of plateau potentials during discharge and charge, is improved by around 2%. To determine the cell internal resistance, electrochemical impedance spectroscopy (EIS) is conducted at fully discharged condition. Figure 3.7B shows that the internal resistance of the cell with modified cathode is reduced by about 3 Ohms, while the charge transfer resistance (diameter of the high-frequency semi-circle) does not change significantly. This indicates that the improved cell performance and reduced internal resistance may be due to a enhanced surface contact between the modified cathode and separator.

Further work must be carried out to fully optimize the specific nature of the chemical bridge for both thermal and electrochemical performance. Long-term stability of the chemical bridging in an electrochemically active environment needs to be further analyzed by evaluating electrochemical stability of the chemical species in the full electrochemical potential window of operation, and potential side reactions with chemical species present in the cell.

### 3.4.4. *Influence on Cell-level Thermal Performance*

Our material-level measurements are consistent with cell-level thermal conductivity measurements [7]. The thermal conductivity of the thermal unit cell, accounting for the measured value of the thermal contact resistance between cathode and separator, is found to be 0.24 W/mK, which is very close to cell-level measurements of 0.15-0.20 W/mK for 26650 and 18650 Li-ion cells [7]. If the thermal contact resistance measured here is not accounted for, and only material thermal resistances are considered, then the effective cell-level thermal conductivity is found to be 1.76 W/mK, which is much higher than cell-level measurements [7].

Figure 3.8 plots the expected overall cell-level thermal conductivity as a function of thermal contact resistance between cathode and separator. Baseline (Experiment A) and improved (Experiment D) values of the thermal contact resistance are also shown on the x-axis. Figure 3.8 indicates an improvement in overall thermal conductivity from 0.24 W/mK (baseline) to 0.76 W/mK (experiment D). There is potential for even steeper improvement in overall thermal conductivity by reducing TCR more through further optimization of the separator-electrode interface. If the TCR can be eliminated completely, the cell-level thermal conductivity can be improved up to 1.76 W/mK.

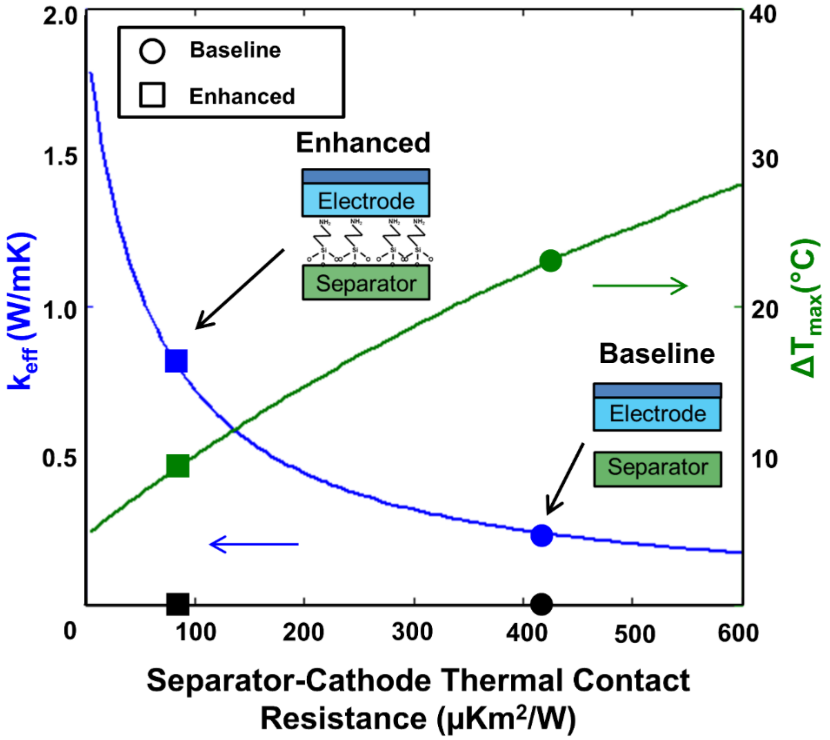

Figure 3.8. Cell-level thermal conductivity (left, blue) and peak temperature rise (right, green) as functions of $R_{sep\text{-}cathode}$, showing values corresponding to both baseline (circles) and enhanced (squares) thermal contact resistance. Measured values of the thermal contact resistance are shown on the x-axis. $k_{eff}$ data are based on calculation of the effective thermal conductivity of the thermal unit-cell, including thermal contact resistance. Temperature rise data are based on a recent analytical thermal model that predicts steady-state temperature distribution in a Li-ion cell.

Figure 3.8 also plots the peak temperature rise in a 26650 Li-ion cell operating at 7C discharge rate in ambient conditions as a function of TCR. The peak temperature rise is computed using our recently reported cell-level thermal model that solves the governing energy equations to predict the temperature distribution in a Li-ion cell as a function of its thermophysical properties [8]. Figure 3.8 shows a significant reduction in peak temperature rise due to TCR reduction and the consequent improvement in thermal conduction within the cell. An additional benefit of TCR reduction demonstrated here is a reduction in temperature gradients within the cell, which is very desirable for balanced and safe cell operation [3]. Temperature gradient within the cell is expected to reduce from 23 °C to 9.5 °C between the baseline TCR and enhanced TCR – a reduction of over 58%. This is made possible by more effective heat removal from the core of the cell, which is a significant challenge at present due to poor cell thermal conductivity. Reductions in both peak temperature and temperature gradient are expected to result in reduced risk of failure, improved reliability and enhanced performance [3]. For example, the thermal head made available by the reduced cell temperature could be made use of by allowing the cell to operate at a higher discharge rate than present, thereby improving performance. This may also reduce the number of cells needed in a battery pack for a certain power output, thereby reducing cost and weight.

Our material-level approach addresses the thermal management problem in Li-ion cells at its fundamental root cause, as opposed to other external approaches, such as cold plate cooling, external liquid cooling, embedded phase change cooling, etc. [3,11]. External cooling approaches are likely to have very limited benefits if the inherent cause of the poor thermal conduction within the cell is not addressed. In addition, our work shows the dominance thermal contact resistance over material resistances within the Li-ion material stack.

The key results presented here – the dominance of TCR as well as reduction in TCR due to surface modification – are both largely insensitive to the thermal conductivities of electrode and separator. Figure S3 (Chapter 3 Appendix 1) in Supplementary Information shows plots of measured baseline and enhanced thermal contact resistances (experiments A and D) over a range of $k_{sep}$ and $k_{elec}$ respectively. Figure S3 shows that results from our measurements do not change significantly with changes in the material thermal conductivities within the range of values reported in the recent past [16-19].

Our results also indicate key trade-offs in thermal and electrochemical performance of a Li-ion cell. Much effort has focused on increasing the porosity and pore size in separators to facilitate ionic transport through the separator [12]. Our results indicate that doing so may actually be detrimental to thermal performance, since the rate-limiting thermal transport at the separator-electrode interface depends critically on good thermal contact between the two.

## 3.5. Conclusions

This work identifies interfacial thermal conduction between cathode and separator as the rate-limiting material-level component of heat transfer within a Li-ion cell, contributing around 88% of overall thermal resistance of the cell. Results also indicate dramatic enhancement of this interfacial thermal transport without affecting electrochemical resistance based on surface modification. Experimental measurements of the interfacial thermal contact resistance are in good agreement with predictions based on the acoustic mismatch model. Cell-level thermal property values based on these measurements are close to recent measurements on 18650 and 26650 cells. Results indicate the possibility of significant improvement in cell-level thermal conductivity and reduction in operating temperature rise as a result of surface modification.

Future research should further investigate the effect of material properties on the separator-cathode contact, for example by changing the size and nature of separator polymer strands, etc. Various possible schemes for chemically bridging the interface must be evaluated experimentally and theoretically, for optimizing thermal and electrochemical effects, as well as for longer-term stability. Due to the closely coupled, multiphysics nature of a Li-ion cell, thermal transport must be evaluated in the context of the fundamental electrochemical processes within the cell. For inclusion in commercially manufactured batteries, integration of the surface modification process in the manufacturing flow must be considered and optimized.

## 3.6. Acknowledgments

A.J. and V.V. would like to acknowledge support from Provost's Office and Department of Mechanical and Aerospace Engineering, The University of Texas at Arlington. F.L. would like to acknowledge support from National Science Foundation (ECCS-1125588). Research at Oak Ridge National Laboratory, managed by UT Battelle, LLC, for the U.S. Department of Energy (DOE) under contract DE-AC05-00OR22725, utilized the DOE Battery Manufacturing R&D Facility at ORNL sponsored by the Office of Energy Efficiency and Renewable Energy's Vehicle Technologies Office.

## 3.7. References

[1] Goodenough, J. B., & Park, K. S. (2013). The Li-ion rechargeable battery: a perspective. *Journal of the American Chemical Society, 135*(4), 1167-1176.

[2] Scrosati, B., & Garche, J. (2010). Lithium batteries: Status, prospects and future. *Journal of Power Sources, 195*(9), 2419-2430.

[3] Bandhauer, T. M., Garimella, S., & Fuller, T. F. (2011). A critical review of thermal issues in lithium-ion batteries. *Journal of the Electrochemical Society, 158*(3), R1-R25.

[4] Karimi, G., & Li, X. (2013). Thermal management of lithium-ion batteries for electric vehicles. *International Journal of Energy Research, 37*(1), 13-24.

[5] Pesaran, A. A. (2001). Battery thermal management in EV and HEVs: issues and solutions. *Battery Man, 43*(5), 34-49.

[6] Drake, S. J., Martin, M., Wetz, D. A., Ostanek, J. K., Miller, S. P., Heinzel, J. M., & Jain, A. (2015). Heat generation rate measurement in a Li-ion cell at large C-rates through temperature and heat flux measurements. *Journal of Power Sources, 285*, 266-273.

[7] Drake, S. J., Wetz, D. A., Ostanek, J. K., Miller, S. P., Heinzel, J. M., & Jain, A. (2014). Measurement of anisotropic thermophysical properties of cylindrical Li-ion cells. *Journal of Power Sources, 252*, 298-304.

[8] Shah, K., Drake, S. J., Wetz, D. A., Ostanek, J. K., Miller, S. P., Heinzel, J. M., & Jain, A. (2014). Modeling of steady-state convective cooling of cylindrical Li-ion cells. *Journal of Power Sources, 258,* 374-381.

[9] Shah, K., Drake, S. J., Wetz, D. A., Ostanek, J. K., Miller, S. P., Heinzel, J. M., & Jain, A. (2014). An experimentally validated transient thermal model for cylindrical Li-ion cells. *Journal of Power Sources, 271*, 262-268.

[10] Lisbona, D., & Snee, T. (2011). A review of hazards associated with primary lithium and lithium-ion batteries. *Process Safety and Environmental Protection, 89*(6), 434-442.

[11] Zolot, M., Pesaran, A. A., & Mihalic, M. (2002). Thermal evaluation of Toyota Prius battery pack (No. 2002-01-1962). SAE Technical Paper.

[12] Zhang, S. S. (2007). A review on the separators of liquid electrolyte Li-ion batteries. *Journal of Power Sources, 164*(1), 351-364.

[13] Etacheri, V., Marom, R., Elazari, R., Salitra, G., & Aurbach, D. (2011). Challenges in the development of advanced Li-ion batteries: a review. *Energy & Environmental Science, 4*(9), 3243-3262.

[14] Yuan, L. X., Wang, Z. H., Zhang, W. X., Hu, X. L., Chen, J. T., Huang, Y. H., & Goodenough, J. B. (2011). Development and challenges of LiFePO 4 cathode material for lithium-ion batteries. *Energy & Environmental Science, 4(*2), 269-284.

[15] Henry, A. (2013). Thermal transport in polymers. *Annu. Rev. Heat Transfer, 17,* 485-520.

[16] Maleki, H., Al Hallaj, S., Selman, J. R., Dinwiddie, R. B., & Wang, H. (1999). Thermal Properties of Lithium-Ion Battery and Components. *Journal of the Electrochemical Society, 146*(3), 947-954.

[17] Nanda, J., Martha, S. K., Porter, W. D., Wang, H., Dudney, N. J., Radin, M. D., & Siegel, D. J. (2014). Thermophysical properties of LiFePO 4 cathodes with carbonized pitch coatings and organic binders: Experiments and first-principles modeling. *Journal of Power Sources, 251,* 8-13.

[18] Gong, M., Zhou, W., Tsai, M.C., Zhou, J., Guan, M., Lin, M.C., Zhang, B., Hu, Y., Wang, D.Y., Yang, J. & Pennycook, S. J. (2014). Nanoscale nickel oxide/nickel heterostructures for active hydrogen evolution electrocatalysis. *Nature communications*, *5*, 4695.

[19] Vishwakarma, V., & Jain, A. (2014). Measurement of in-plane thermal conductivity and heat capacity of separator in Li-ion cells using a transient DC heating method. *Journal of Power Sources, 272*, 378-385.

[20] Vishwakarma, V., & Jain, A. (2014). Measurement of in-plane thermal conductivity and heat capacity of separator in Li-ion cells using a transient DC heating method. *Journal of Power Sources, 272*, 378-385.

[21] Kim, U. S., Shin, C. B., & Kim, C. S. (2009). Modeling for the scale-up of a lithium-ion polymer battery. *Journal of Power Sources, 189*(1), 841-846.

[22] O'brien, P. J., Shenogin, S., Liu, J., Chow, P. K., Laurencin, D., Mutin, P.H., Yamaguchi, M., Keblinski, P. & Ramanath, G. (2013). Bonding-induced thermal conductance enhancement at inorganic heterointerfaces using nanomolecular monolayers. *Nature materials*, *12*(2), 118.

[23] Kaur, S., Raravikar, N., Helms, B. A., Prasher, R., & Ogletree, D. F. (2014). Enhanced thermal transport at covalently functionalized carbon nanotube array interfaces. *Nature communications*, *5*, 3082.

[24] Reifenberg, J. P., Chang, K. W., Panzer, M. A., Kim, S., Rowlette, J. A., Asheghi, M., Wong, H.S.P. & Goodson, K. E. (2010). Thermal boundary resistance measurements for phase-change memory devices. *IEEE Electron Device Letters, 31*(1), 56-58.

[25] Cho, J., Li, Z., Bozorg-Grayeli, E., Kodama, T., Francis, D., Ejeckam, F., Faili, F., Asheghi, M. & Goodson, K. E. (2013). Improved thermal interfaces of GaN–diamond composite substrates for HEMT applications. *IEEE Transactions on Components, Packaging and Manufacturing Technology, 3*(1), 79-85.

[26] Javed, A., Iqbal, S. M., & Jain, A. (2012). Microheater platform for selective detachment of DNA. *Applied Physics Letters, 101*(9), 093707.

[27] Kasry, A., Borri, P., Davies, P. R., Harwood, A., Thomas, N., Lofas, S., & Dale, T. (2009). Comparison of methods for generating planar DNA-modified surfaces for hybridization studies. *ACS applied materials & interfaces, 1*(8), 1793-1798.

[28] Vishwakarma, V., Waghela, C., & Jain, A. (2015). Measurement of out-of-plane thermal conductivity of substrates for flexible electronics and displays. *Microelectronic Engineering, 142*, 36-39.

[29] Prasher, R. (2008). Thermal boundary resistance and thermal conductivity of multiwalled carbon nanotubes. *Physical Review B, 77*(7), 075424.

[30] Kim, J. R., Choi, S. W., Jo, S. M., Lee, W. S., & Kim, B. C. (2005). Characterization and properties of P (VdF-HFP)-based fibrous polymer electrolyte membrane prepared by electrospinning. *Journal of the Electrochemical Society, 152*(2), A295-A300.

[31] Prasher, R. (2009). Acoustic mismatch model for thermal contact resistance of van der Waals contacts. *Applied Physics Letters, 94*(4), 041905.

[32] Johnson, K. L., Kendall, K., & Roberts, A. D. (1971, September). Surface energy and the contact of elastic solids. *In Proceedings of the Royal Society of London A: Mathematical, Physical and Engineering Sciences* (Vol. 324, No. 1558, pp. 301-313). The Royal Society.

[33] Baney, J. M., & Hui, C. Y. (1997). A cohesive zone model for the adhesion of cylinders. *Journal of adhesion science and technology, 11*(3), 393-406.

[34] Autumn, K., Sitti, M., Liang, Y. A., Peattie, A. M., Hansen, W. R., Sponberg, S. Kenny, T.W., Fearing, R., Israelachvili, J.N.& Full, R. J. (2002). Evidence for van der Waals adhesion in gecko setae. *Proceedings of the National Academy of Sciences*, *99*(19), 12252-12256.

[35] Alofi, A., & Srivastava, G. P. (2013). Thermal conductivity of graphene and graphite. *Physical Review B, 87*(11), 115421.

[36] Swartz, E. T., & Pohl, R. O. (1989). Thermal boundary resistance. *Reviews of modern physics, 61*(3), 605.

[37] Koo, B., Goli, P., Sumant, A. V., dos Santos Claro, P. C., Rajh, T., Johnson, C. S., Balandin, A.A. & Shevchenko, E. V. (2014). Toward lithium ion batteries with enhanced thermal conductivity. *ACS nano, 8*(7), 7202-7207.

[38] Egitto, F. D., & Matienzo, L. J. (1994). Plasma modification of polymer surfaces for adhesion improvement. *IBM Journal of Research and Development*, *38*(4), 423-439.

[39] Shenton, M. J., Lovell-Hoare, M. C., & Stevens, G. C. (2001). Adhesion enhancement of polymer surfaces by atmospheric plasma treatment. *Journal of Physics D: Applied Physics*, *34*(18), 2754.

[40] http://ocw.mit.edu/courses/materials-science-and-engineering/3-11-mechanics-of-materials-fall-1999/modules/props.pdf, accessed March 17, 2015.

# CHAPER 3 APPENDIX 1

# SUPPLEMENTARY MATERIALS

# HEAT TRANSFER ENHANCEMENT IN A LI-ION CELL

Vishwakarma, V., Waghela, C., Wei, Z., Prasher, R., Nagpure, S. C., Li, J., Liu, F., & Jain, A. (2015). Heat transfer enhancement in a lithium-ion cell through improved material-level thermal transport. *Journal of Power Sources*, *300*, 123-131.

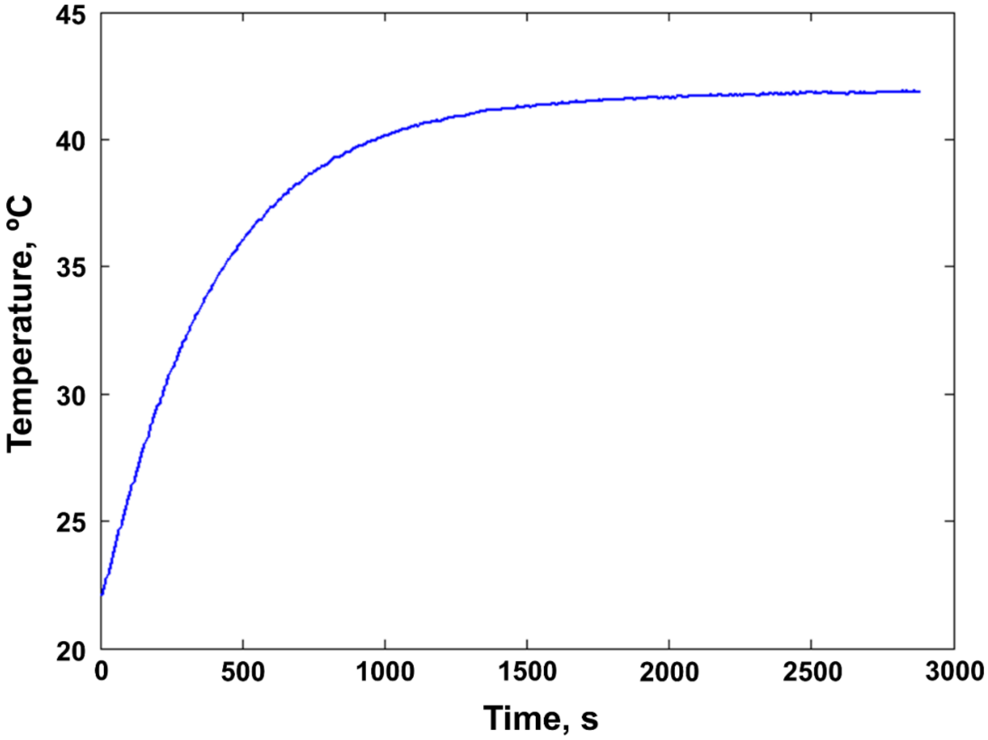

Figure S1. Plot of the measured temperature from top-most thermocouple in top copper block as a function of time for experiment A. Similar behavior is observed for other thermocouples, and in other experiments.

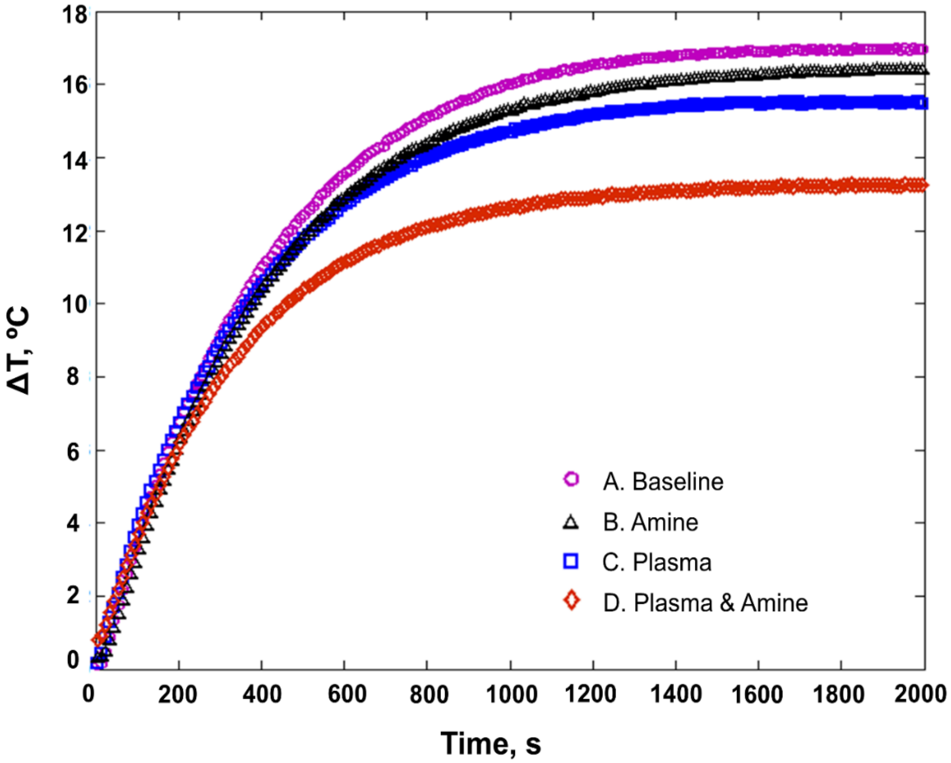

Figure S2. Plot of the measured temperature drop across the sample as a function of time for experiments A-D.

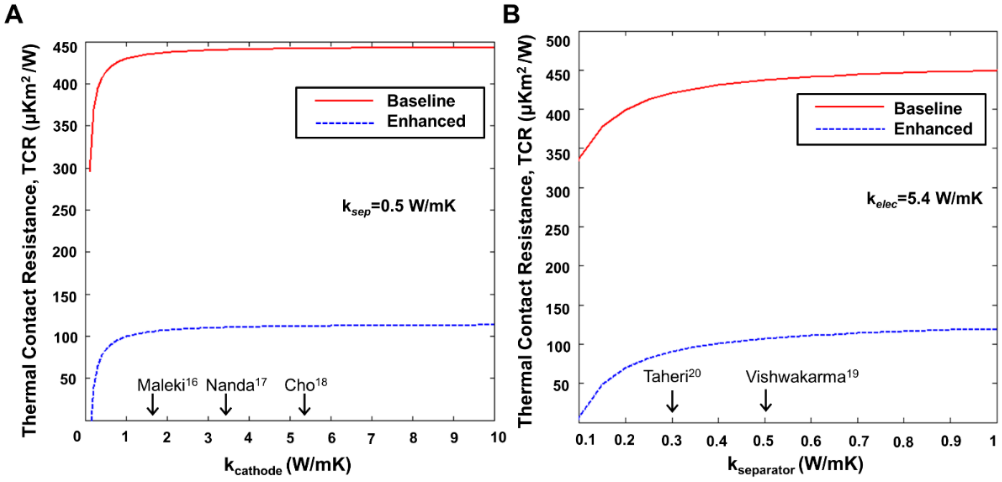

Figure S3. Plots showing the effect of values of cathode and separator thermal conductivities on experimental results, (A) shows the dependence of $R_{sep\text{-}cathode}$ on $k_{cathode}$, and (B) shows dependence of $R_{sep\text{-}cathode}$ on $k_{sep}$. Within the expected range of these thermal properties, $R_{sep\text{-}cathode}$ remains nearly invariant.

# CHAPTER 4

# ENHANCEMENT OF THERMAL TRANSPORT IN GEL-POLYMER ELECTROLYTES WITH EMBEDDED BN/AL$_2$O$_3$ NANO- AND MICRO-PARTICLES

Vishwakarma, V., & Jain, A. (2017). Enhancement of Thermal Transport in Gel-Polymer Electrolytes with Embedded BN/Al2O3 Nano- and Micro-Particles. *Journal of Power Sources*, *362*, 219-227.

Abstract

While Gel-Polymer Electrolytes (GPEs) have been widely investigated for use in next-generation Li-ion cells due to the potential for improved thermal safety, thermal transport within a GPE is still poorly understood. Among all materials in a Li-ion cell, the GPE has the lowest thermal conductivity, and hence determines the overall rate of heat flow in a Li-ion cell. This makes it critical to measure and understand thermal transport in a GPE and investigate trade-offs between thermal and ionic transport. This chapter presents measurements of thermal and ionic conductivities in a PVdF-based GPE. The effect of incorporating BN/$Al_2O_3$ ceramic nano/microparticles in the GPE on thermal and ionic transport is characterized. Measurements indicate up to 2.5X improvement in thermal conductivity of activated GPE membranes, with relatively minor effect on electrochemical performance of GPE-based single-layer cells. The measured enhancement in thermal conductivity is in very good agreement with theoretical calculations based on the effective medium theory that accounts for thermal transport in a dispersed, two-phase medium such as a GPE. The fundamental insights gained in this work on thermal transport in a GPE and the role of nano/microparticle inclusions may facilitate thermal-electrochemical optimization and design of GPEs for safe, high-performance Li-ion cells.

Keywords: Gel Polymer Electrolyte, Li-Ion Battery, Nanoparticles, Thermal Transport, Battery Safety.

## 4.1. Introduction

Li-ion batteries have been used extensively for energy storage and conversion in electric vehicles, energy storage systems, portable electronics, etc. due to their excellent electrochemical performance [1-3]. New battery paradigms are beginning to emerge to overcome the limitations of present Li-ion cells and extend the state-of-the-art for performance and safety. For example, the use of volatile and combustible liquid electrolyte in traditional Li-ion cells poses a severe risk of fire and explosion [4, 5], even at slightly elevated cell temperature. Such safety concerns have severely restricted the performance envelope of Li-ion cells. Traditional Li-ion cells also suffer from significant design restrictions due to the use of liquid electrolyte and rigid separator membranes. In the recent past, gel-polymer electrolytes (GPEs) have been widely investigated as a potential replacement of the conventional liquid electrolyte and separator [6-9]. A GPE comprises a polymer matrix capable of holding liquid electrolyte without sacrificing much of the electrochemical and mechanical performance [9]. The absorbed liquid electrolyte is immobilized within the pores of the polymer matrix, retaining the properties of the liquid electrolyte and conventional separator, while minimizing the volume of the combustible electrolyte needed, which results in improved safety [7]. By eliminating the need to contain a liquid electrolyte in a rigid containment, GPEs also offer an added advantage of enabling batteries in a wide variety of shapes, including flexible batteries [10, 11]. Polyethylene oxide (PEO), polyacrylonitrile (PAN), polymethyl methacrylate (PMMA), and polyvinylidene fluoride (PVdF) are the most widely studied polymer matrices for GPEs [7, 9]. The electrochemical performance of GPE-based Li-ion cells has been studied to understand the effect of replacing the traditional separator with a GPE. For example, GPE based Li–ion cells have been tested for charge-discharge cycling and capacity fade [13-19, 20]. Cycling performance of a $LiCoO_2$/GPE/Anode cell between 2-4.2V has been investigated, showing stable charge/discharge performance for up to 50 cycles without significant capacity loss and good compatibility of the polymer electrolyte with electrode materials [14-19]. The capacity fade in an $Al_2O_3$/$BaTiO_3$ ceramic filler based Li-ion polymer cell has been shown to be less than 10% after 50 discharge cycles [19]. While several research challenges remain, GPEs offer a plausible alternative to liquid electrolytes in next-generation electrochemical batteries [12, 21].

A key question that continues to be investigated is the effect of using a GPE on various transport and storage processes, such as charge transport and capacity.

PVdF based polymer membranes offer high dielectric constant, thereby increasing charge carrying capacity [23]. The semi-crystalline structure of PVdF also helps in enhanced ion storage and mobility [23]. When used along with a mixture of carbonate esters such as Ethylene Carbonate (EC) and Propylene Carbonate (PC), PVdF has been shown to offer reasonably large ionic conductivity of around 2 mS/cm [23, 24]. In order to further increase the ionic conductivity of a GPE, the use of ionic liquids such as imidazolium cations in the liquid electrolyte has been widely studied [25, 26]. The use of 1-ethyl-3-methylimidazolium tetrafluoroborate ($EMIBF_4$) as an electrolyte solvent for $LiBF_4$ has been shown to result in ionic conductivity in the 0.23-10 mS/cm range between 20°C and 40°C [26]. The fundamental nature of Li ion transport phenomena in the presence of these ionic liquids continues to be a topic of much current interest [17, 27].

In addition to ionic transport, thermal transport in GPE materials is also important to study. Although the use of a GPE in a Li-ion cell reduces the volume of combustible electrolyte, it also leads to introduction of new materials and manufacturing processes. Several research challenges related to thermal transport in GPEs must be fully understood before the safety advantage of GPEs can be conclusively established [12, 21]. The fundamental nature of heat transfer through GPE materials is still poorly understood, with very limited experimental data on fundamental thermal transport properties. The dominance of interfacial thermal contact resistance between electrode and separator in thermal transport in a conventional Li-ion cell [28] may not hold for a GPE based cell due to the distinctly different manufacturing and assembly of a GPE-based cell. Since electrode material is directly deposited on a GPE [29], interfacial thermal contact resistance may be negligible, and therefore, heat transfer through GPE materials may be the slowest, rate-determining step in overall thermal conduction process inside a Li-ion cell. This makes it critical to experimentally characterize the thermal transport properties of a GPE, and explore mechanisms for thermal transport enhancement. While some work is available on thermal characterization of traditional separators, including thermal conductivity [30, 31] and interfacial thermal contact resistance [28] measurements, there is a lack of such work on GPE materials.

Impregnation of micro-sized and nano-sized ceramic fillers has been used extensively for enhancement of mechanical, electrical, thermal and multifunctional properties in polymers [19, 32-35]. However, this approach has not yet been investigated much in the context of thermal transport in GPEs. Some work has been carried out with ceramics fillers such as $Al_2O_3$ [19, 32, 36-39], $BaTiO_3$ [19], $TiO_2$ [19] in a GPE to investigate electrochemical stability, ionic conductivity and compatibility with electrodes. Recently, thermally conductive $Al_2O_3$/polymer composite separator has been developed by mixing PVdF-HFP and nano-micro sized $Al_2O_3$ particles for conventional Li-ion batteries [32]. Clearly, much more needs to be done to fully understand the effect of nano/micro-sized particle inclusion on the thermal properties of GPEs, and eventually on thermal performance of GPE-based Li-ion cells.

This chapter presents measurement and enhancement of thermal transport in PVdF-based GPEs through $Al_2O_3$ and BN ceramic nano/micro particle inclusion in the GPE. Measurements show 13X and 2.5X improvement in thermal conductivity of the PVdF membrane and PVdF based GPE respectively. Experimental results are found to be in good agreement with the effective medium theory (EMT) model for thermal conductivity of baseline and thermally enhanced GPEs. Implications of such nano/microparticle inclusion on the electrochemical performance of the GPE and GPE-based Li-ion cell is also reported. Electrochemical impedance spectroscopy (EIS) and charge-discharge measurements characterize the effect of nanoparticle inclusion on electrochemical performance, highlighting the need for careful consideration of thermal-electrochemical trade-offs in GPEs. Results presented here may help understand and enhance thermal transport in GPE materials. The thermal transport properties reported in this work may facilitate accurate simulations of thermal performance and safety of GPE-based Li-ion cells, as well as multiphysics thermal-electrochemical co-optimization.

## 4.2. Experimental Methods and Materials:

### 4.2.1. *Materials*

$Al_2O_3$ and BN nanoparticles (800nm) and BN micro particles (~2.5µm) (US Research Nanomaterials Inc.) are used in this work for investigating GPE thermal enhancement. These materials are known to offer high thermal conductivity of 18-34 W/mK [32], high electrical resistivity of $10^{14}$ Ω-cm, light weight and has moderate cost compared to other ceramics [19, 35, 36, 40-42], which is critical for a GPE. Poly(vinylidene Fluoride) (PVdF) (Sigma Aldrich) is used as the gel polymer host matrix. PVdF offers high dielectric constant, supports high charge concentration and offers high thermal stability, due to which it has been used widely as the polymer host material for Li-ion battery GPEs [43-44]. Lithium hexafluorophosphate ($LiPF_6$) (Sigma Aldrich) is used as the electrolyte due to its excellent ionic conductivity in carbonate based solvents [44]. 1-Methyl-2-pyrrolidone (NMP) (Sigma Aldrich) is used as a solvent to dissolve PVdF and to obtain porous membranes. NMP offers high boiling point, low volatility and non-toxicity [45]. A mixture of ethylene carbonate (EC) (Sigma Aldrich) and propylene carbonate (PC) (Sigma Aldrich) acts as plasticizer for PVdF and is used to extract gel polymer membranes. Also, EC/PC ester acts as a solvent for $LiPF_6$ and offers thermal stability [46]. 1-Ethyl-3-methylimidazolium triluoromethanesufonate (EMI-TF) (Sigma Aldrich) is also used as a part of the ionic liquid in the electrolyte mixture. EMI-TF offers very high ionic conductivity (10mS/cm), which has been reported to enhance the overall ionic conductivity of the electrolyte mixture [16, 47]

### 4.2.2. *GPE Synthesis and Enhancement*

The synthesis of 100-1200 µm thick PVdF-based polymer membranes is carried out by following a previously described procedure in section 4.2.1 [43]. The porous PVDF membrane is obtained by first making an ester solution of 1:1 mixture of EC and PC by mass, and heating at 80 °C (Isotemp, Fisher Scientific) until a clear solution is obtained. This ester solution is then mixed with NMP and PVdF in 40%, 44% and 16% proportion by weight respectively, as shown in Figure 4.1(A). The mixture is heated at 110 °C (Isotemp, Fisher Scientific) and stirred until a pale viscous solution is obtained. This solution is poured in petri dishes (Figure 4.1(B)) and baked at 80 °C in 0.07 MPa vacuum in a vacuum oven (Across International AccuTemp-09) for two hours. The membranes are then soaked in 10% ethanol for 8 hours. Finally, the GPE is obtained by soaking and activating the PVdF membrane in a mixture of 1.0 M $LiPF_6$ with ionic liquid solvents (2:1:1 by volume of EMI-TF, EC and PC) for 24 hours. For samples with nano/microparticle

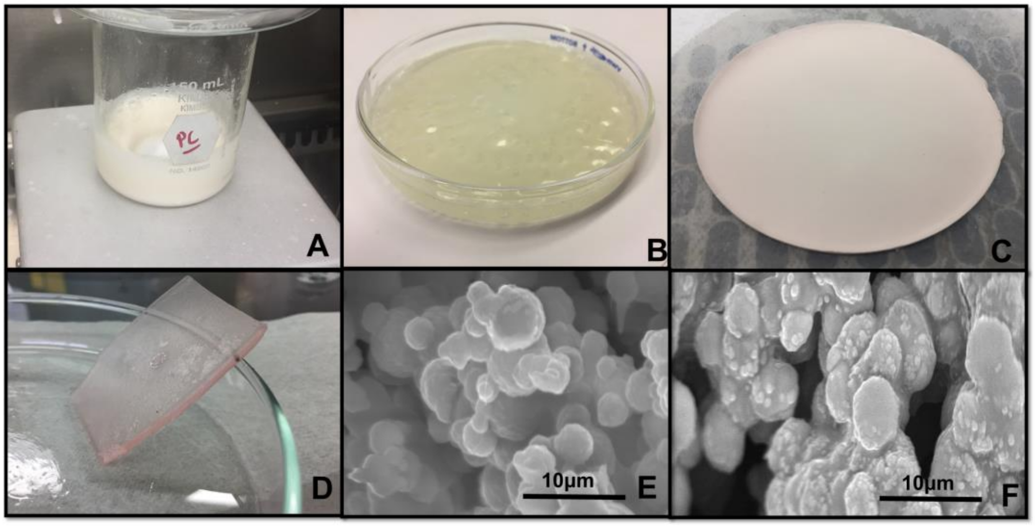

Figure 4.1. Gel polymer electrolyte synthesis by casting: (A) A mixture of PVdF, EC, PC, NMP (section 2.2) is heated at 110 °C and stirred until a pale viscous solution is obtained; (B) This solution is poured in petri dishes and baked at 80 °C under 0.07MPa vacuum in a vacuum oven for two hours; (C) Porous PVdF membrane after soaking in 10% ethanol for 8-10 hours; (D) the GPE is obtained by soaking and activating the PVdF membrane in a mixture of 1.0 M $LiPF_6$ with ionic liquid solvents; (E) SEM image of the PVdF membrane; (F) SEM image of the 800nm BN impregnated PVdF membrane.

inclusion, the nano/microparticles are mixed with NMP during the PVdF membrane formation process. 100-1200 µm thick samples of 4×4 $cm^2$ size are obtained through this process (Figure 4.1(C)). The thickness of the membranes is controlled through the volume of the solution poured in petri dishes, and measured using vernier calipers ( ±10 μm) (Figure 4.1(D)). The resulting PVdF based membranes are highly porous in nature, as shown in Supplementary Figure S1(A) (Chapter 4 Appendix 1), with pore diameter ranging from 2-10μm and PVdF grain diameter ranging from 2-5μm. Figures 4.1(E) and 4.1(F) show SEM images of the porous PVdF membrane with no nanoparticle and with 800nm BN nanoparticles. Figure 4.1(F) shows that BN nanoparticles are bonded uniformly to the outer periphery of the PVdF grains. Some agglomeration is observed at higher nanoparticle concentration. Tables 4.1 and 4.2 summarize GPE samples with a variety of micro/nanoparticles concentration investigated in this work. In addition to the baseline case without any nano/microparticles, cases investigated here include 1:32 BN, 1:8 BN and 1:8 $Al_2O_3$ inclusion in PVdF. A case of 1:8 800nm $Al_2O_3$+2.5μm BN is also investigated, which is expected to offer enhanced thermal transport compared to a nanoparticles-only case due to the reduction in thermally resistant junctions offered by multiscale micro-nano particles [40].

### 4.2.3. *Thermal Transport Measurements*

The primary thermal property of interest for a GPE is thermal conductivity, which determines the amount of heat flux for a given temperature gradient [48]. In general, a high thermal conductivity is desired, since it minimizes temperature rise of the cell above ambient temperature. Thermal conductivity of the GPE samples is measured by a thermal constants analyzer (TPS 2200, Thermtest Inc., Canada) capable of 0.1mK accuracy for temperature difference detection, as shown in Figure 4.2(A). The repeatability of measurements by this instrument is established through repeated measurements of a standard test sample made of steel, which demonstrates a standard deviation of less than 1% between five measurements. Figure 4.2(A) also shows pictures of PVdF and GPE samples used for thermal conductivity measurements. This instrument utilizes the transient plane source method [49-50]. In this method, a thin metal heater/sensor is sandwiched between two identical samples. It has been shown [49] that during transient heating, the measured temperature increase of the heater/sensor over a short period of time can be compared with an analytical model for heat diffusion in an infinite medium

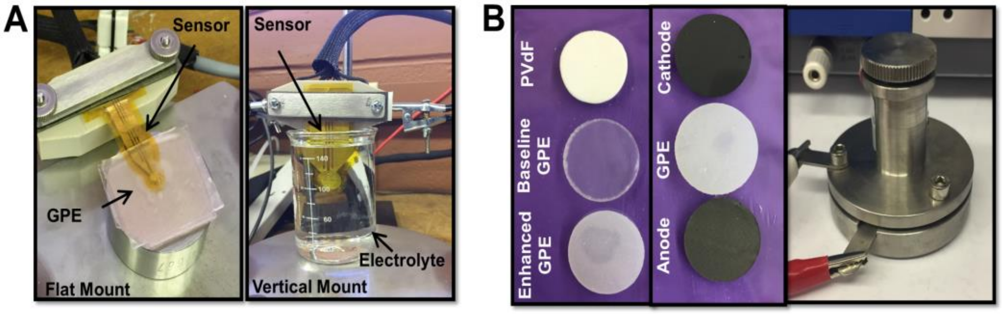

Figure 4.2. (A) Pictures of experimental setup for thermal conductivity measurement on GPE and electrolyte mixture using the transient plane source method. (B) Pictures of PVdF, baseline and nanoparticle-impregnated GPE. Pictures of electrodes and GPE for single-layer cell fabrication and testing are also shown.

to determine the thermal transport properties of the sample. Briefly, the temperature rise at the sensor is given by [49-50]:

$$\Delta T(\tau) = \frac{P}{\pi^{\frac{3}{2}} a k} D(\tau) \qquad (1)$$

where $\Delta T(\tau)$ is the temperature rise (°C), $P$ is power input to the sensor, $a$ is the radius of the senor, $k$ is the thermal conductivity of the sample and $D(\tau)$ is dimensionless time given by [49-50]:

$$D(\tau) = \frac{1}{m^2(m+1)^2} \int_0^{\tau} \frac{d\sigma}{\sigma^2} \sum_{i=1}^{m} i \sum_{l=1}^{m} l e^{-((i^2+l^2)/m^2)/4\sigma^2} I_0\left(\frac{il}{2m^2\sigma^2}\right) \qquad (2)$$

In equation (2), $m$ refers to the number of the concentric rings source in the heater.

Note that $\tau = \frac{\sqrt{\alpha t}}{a}$ involves the thermal diffusivity $\alpha$, which is determined as the value that results in a linear relationship between the measured functions $\Delta T(\tau)$ and $D(\tau)$based on equation (1). Following this, thermal conductivity is obtained from the slope of this relationship, as indicated by equation (1).

In these experiments, a 2.01 mm diameter heater is utilized. Due to temperature-dependent resistivity of the metal heater, it can simultaneously be used as a temperature sensor. The time period of the experiment is chosen such that it preserves the infinite medium assumption and results in highest possible sensitivity.

### 4.2.4. *Electrochemical Measurements*

Two-probe method is used to first measure the ionic conductivity of the GPE. The ionic conductivity of the GPE is measured by EIS using two steel plates (active area ~ 3.14 $cm^2$) as the blocking electrode cells. The GPE membrane is placed between two steel plates and enclosed in a split flat cell setup, as shown in Figure 2(B). Measurements are carried out at room temperature. Ionic conductivity is determined using measurements of internal resistance (*Z*), cross-section area (*A*) and thickness (*t*) of the sample as follows:

$$\sigma = \frac{t}{Z \cdot A} \tag{3}$$

A split flat cell (MTI Corporation) with an active area of 3.14 $cm^2$ is utilized for electrochemical characterization of a GPE and GPE based single-layer Li-ion cell without and with micro/nanoparticle enhancement. The assembly of the cell is carried out in an inert Argon atmosphere inside a glovebox (LC Technologies). 80μm thick $LiFePO_4$ positive electrode (MTI Corporation) and 80μm thick graphite-based negative electrode (MTI Corporation) are assembled along with a 100μm thick GPE . Pictures of electrodes and GPE samples used for the cell assembly process are shown in Figure 4.2(B).

After cell assembly, the cell is kept at rest for 24 h for minimum potential buildup. Electrochemical Impedance Spectroscopy (EIS) experiments are conducted using a VersaSTAT4 potentiostat/galvanostat over a frequency range from 0.1 mHz to 100 MHz at open circuit with an amplitude of 10 mV while the cells are fully discharged. In order to characterize the charging and discharging performance of various GPE samples, the cells are charged at 5mA current up to 3.1V, followed by discharge at the same current up to 2.2V using the same instrument. To avoid overcharge/discharge of a cell, pre-established limits of 3.6V for charging and 2.2V for discharging are implemented.

### 4.3. Theoretical Heat Transfer Model

From a heat transfer perspective, the GPE is a heterogeneous system comprising a porous PVdF matrix filled with liquid electrolyte. Several theoretical and empirical models have been proposed to predict the effective thermal conductivity of such systems [51-54]. In the past, expressions for effective thermal conductivity bounds for macroscopically homogeneous, isotropic, two-phase materials based on volume fractions and thermal conductivities of constituents have been proposed. These expressions usually utilize the Maxwell-Eucken model [55]. However, this model assumes that the inclusions of the dispersed phase, such as particles or bubbles do not come into contact with neighboring inclusions, resulting in a lack of continuous path for heat conduction by the dispersed phase. However, the porous GPE samples investigated here (Supplementary Figure S2 (A)(Chapter 4 Appendix 1)) appear to provide a continuous heat conduction path through the dispersed phase, as shown through image analysis (Supplementary Figures S2(B) (Chapter 4 Appendix 1)), where dark regions are the liquid electrolyte mixture and bright regions are PVdF grains. In such a case, the Effective Medium Theory (EMT) is a more appropriate model. EMT theory predicts the effective thermal conductivity, $k_{eff}$ of a porous system as follows [51-54]:

$$k_{eff} = \frac{1}{4}\left( (3v_e - 1)k_e + [3(1 - v_e) - 1]k_p + \sqrt{[(3v_e - 1)k_e + (3\{1 - v_e\} - 1)k_p]^2 + 8k_p k_e} \right) \quad (4)$$

where $v_e$ is the volume fraction of electrolyte in the PVdF matrix, $k_e$ and $k_p$ is the thermal conductivity of the electrolyte mixture and the PVdF respectively.

## 4.4. Results and Discussion:

### 4.4.1 *Thermal Transport measurements*

GPE is a binary system with liquid electrolyte immobilized within the porous PVdF matrix. Therefore, the thermal conductivity of the electrolyte plays an important role in determining the overall effective thermal conductivity of the GPE and is measured first. Figure 4.2(A) shows the experimental setup for measuring thermal conductivity of the electrolyte. Instead of using a horizontal stage for mounting the transient plane source sensor, as is the usual case, a vertical stage is designed to hold and submerge the sensor head in the liquid of interest (Figure 4.2(A)). A plot of the temperature rise normalized by power, *ΔT(τ)/P* as a function of the dimensionless time *D(τ)* for the electrolyte measurement is shown in Supplementary Figure S3 (Chapter 4 Appendix 1). A linear relationship in found, in accordance with equation (5). Thermal conductivity of the electrolyte mixture is measured in this manner to be 0.35±0.01W/mK.

Thermal conductivity measurement of various GPE samples without and with nanoparticles is carried out next. Figure 4.3 plots the sensor temperature rise normalized by power, *ΔT(τ)/P,* as a function of the dimensionless time *D(τ)* for five different cases of unactivated PVdF membrane. As discussed in section 4.2.3, a plot of *ΔT(τ)/P* versus *D(τ)* is expected to be linear with thermal conductivity related to the slope *M* as follows:

$$k = \left( \frac{1}{\pi^{\frac{3}{2}} a M} \right) \tag{5}$$

The linear nature of ΔT*(τ)/P* versus *D(τ)* curves as shown in Figure 4.3 for each case confirms the validity of the measurement.

Table 4.1. Thermal conductivity ($k_p$) of baseline and enhanced PVdF membranes measured using the transient plane source method.

| **Cases** | **Samples** | **Nano/microparticles Size** | **Weight Ratio of Nano/microparticles** | **PVdF Thermal Conductivity, $k_p$, W/mK** |
|---|---|---|---|---|
| 1A | Baseline | None | None | 0.09±0.002 |
| 1B | PVdF+BN | 800nm | 1:32 | 0.22±0.004 |
| 1C | PVdF+BN | 800nm | 1:8 | 0.83±0.017 |
| 1D | PVdF+$Al_2O_3$ | 800nm | 1:8 | 0.98±0.020 |
| 1E | PVdF+$Al_2O_3$, BN | 800nm, 2.5μm | 1:8 | 1.2±0.024 |

Thermal conductivity values for five different cases measured in this manner are summarized in Table 4.1 and also shown in Figure 4.3. Thermal conductivity for the baseline, un-activated PVdF membrane without nanoparticle

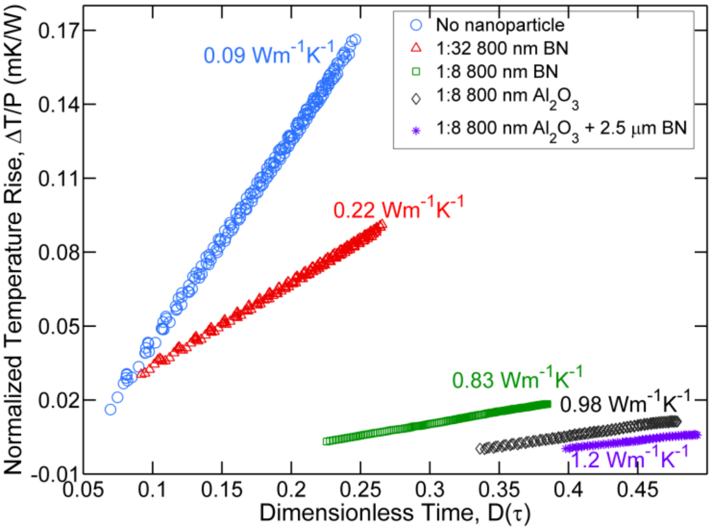

Figure 4.3. Normalized temperature rise, *ΔT/P* as a function of dimensionless time *D(τ)* for thermal conductivity ($k_p$) measurement of baseline and thermally enhanced PVdF membranes.

inclusion (Case 1A) is measured to be 0.09±0.002 W/mK. Enhancement in thermal conductivity is observed in each case when BN or $Al_2O_3$ nano/microparticles are embedded. The measured enhancement is greater at higher weight ratios of the nano/microparticles, with 9X enhancement at 1:8 weight ratio. The enhancement (Case 1C) for the same weight ratio. Interestingly, even further enhancement in thermal conductivity is measured when using a mixture of 800 nm $Al_2O_3$ nanoparticles and 2.5 μm BN microparticles (Case 1E). The measured thermal

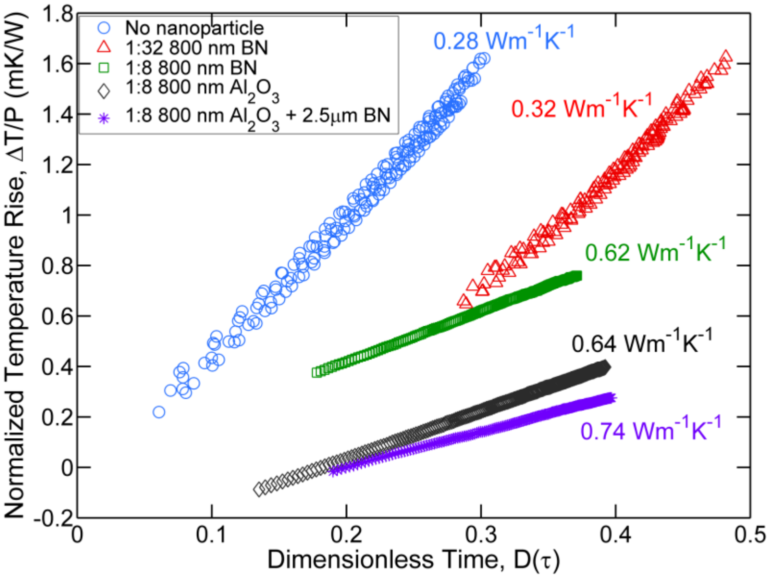

Figure 4.4. Normalized temperature rise, *ΔT/P* as a function of dimensionless time *D(τ)* for thermal conductivity ($k_{eff}$) measurement of baseline and thermally enhanced GPE samples.

conductivity of 1.2 W/mK represents a significant, 13X improvement in thermal conductivity compared to the baseline sample (Case 1A). The observed thermal conductivity enhancement is explained well by the effective medium model as discussed later in section 4.4.3.

Another set of experiments are carried out to investigate the effect of nano/microparticle inclusion in the GPE formed by activating the PVdF membranes with electrolyte. Figure 4.4 plots the temperature rise $\Delta T(\tau)/P$ at the sensor as a function of the dimensionless time $D(\tau)$ for these measurements, showing linear behavior for each case as expected. Measured values of thermal conductivity are shown in Figure 4.4 and summarized in Table 4.2.

Table 4.2. Thermal conductivity ($k_{eff}$) of baseline and enhanced GPE membranes measured using the transient plane source method.

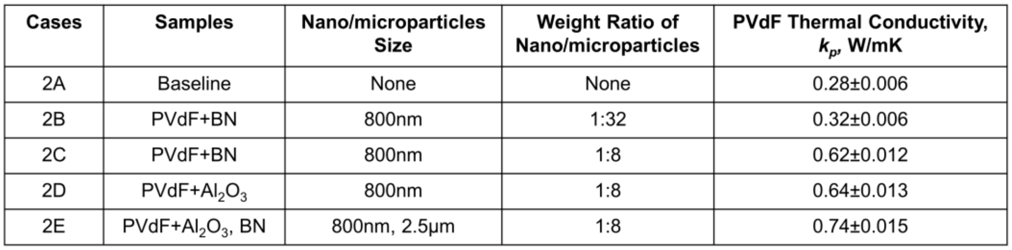

| Cases | Samples | Nano/microparticles Size | Weight Ratio of Nano/microparticles | PVdF Thermal Conductivity, $k_p$, W/mK |
|---|---|---|---|---|
| 2A | Baseline | None | None | 0.28±0.006 |
| 2B | PVdF+BN | 800nm | 1:32 | 0.32±0.006 |
| 2C | PVdF+BN | 800nm | 1:8 | 0.62±0.012 |
| 2D | PVdF+$Al_2O_3$ | 800nm | 1:8 | 0.64±0.013 |
| 2E | PVdF+$Al_2O_3$, BN | 800nm, 2.5μm | 1:8 | 0.74±0.015 |

The thermal conductivity of baseline GPE (Case 2A) is measured to be 0.28±0.006 W/mK, which is significantly larger than that of the unactivated PVdF membrane (Case 1A) due to increased thermal conduction by the electrolyte in the activated samples. The degree of enhancement in thermal conductivity due to nano/microparticle inclusion in GPE is somewhat lower compared to the unactivated PVdF membranes. For example, there is 2.5X enhancement with 1:8 weight ratio of a combination of $Al_2O_3$ nanoparticles and BN microparticles (Case 2E). Since the baseline thermal conductivity itself is so low, this 2.5X enhancement is quite significant and may result in significant reduction in peak operating temperature at large discharge rates [28], and potentially improved thermal runaway behavior. A similar enhancement is measured for 800 nm $Al_2O_3$ nanoparticles (Case 2D) as well. Finally, similar to experiments on unactivated PVdF membranes, there is additional enhancement when using a combination of micro and nanoparticles (Case 2E) instead of nanoparticles only. This synergistic effect is consistent with observations in past papers [32].

### 4.4.2 *Electrochemical Measurements*

Various compositions of ionic liquids (EC:PC:EMI-TF = 0:1:1, 1:1:6, 1:1:2) in 1:1 $LiPF_6$ mixture and various percentages of ionic liquid in an electrolyte mixture have been investigated in the literature in the past [43]. In the present work, a 1:1:2 composition of EC, PC and EMI-TF is mixed in 1:1 ratio with 1 M $LiPF_6$, which has been reported to have higher ionic conductivity [43]. As shown in Figure 4.5(A), the ionic conductivity of the activated GPE without any thermal enhancement is found to be 4.1±0.25 mS/cm whereas ionic conductivity of the 1:8

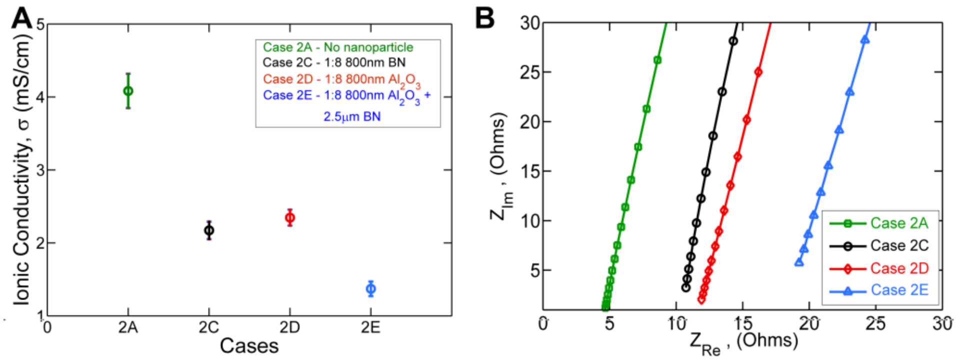

Figure 4.5. (A) Ionic conductivity measurement of GPE samples with different concentrations of micro-sized (2.5µm BN) and nano-sized (800nm $Al_2O_3$) ceramic particles. (B) Nyquist plot for baseline and enhanced GPE samples (Case 2A, Case 2C, Case 2D and Case 2E) to obtain internal resistance for ionic conductivity calculation

micro/nano BN-$Al_2O_3$ embedded GPE (Case 2E) is found to be 1.4±0.03 mS/cm. Figure 4.5(B) shows the Nyquist plot for all the cases disused in Figure 4.5(A). As expected internal resistance (*Z*) offered by baseline sample (Case 2A) is found to be 4.2±0.7 Ohms whereas internal resistance for the enhanced sample (Case 2E) is found to be 17.4±0.3 Ohms. Case 2C and 2D are also resulted in higher internal resistance due to reduced volume fraction of electrolyte mixture in the PVdF matrix due to micro/nano particles loading [39]. Therefore as per eq. 3, increased internal resistance has resulted in the reduction in ionic conductivity.

In order to further investigate the effect of thermal enhancement of the GPE on battery performance, electrochemical tests are performed in a split flat cell on a single layer cell using the GPE samples. Figure 4.6(A) shows the charge discharge profile of cells with baseline, unenhanced GPE sample (Case 2A) and BN-$Al_2O_3$ embedded GPE (Case 2E). The two curves are similar in nature to each other. The charging potential for the enhanced GPE case is about ~44mV lower than the traditional GPE at the peak of charging potential, until it reaches 3.1V. However, the discharge potential of enhanced GPE is about ~ 140mV higher than the traditional GPE as the discharge potential reaches lower threshold limit of 2.2V, indicating somewhat better discharge capacity with more available energy in the thermally enhanced case. Ceramics such as $Al_2O_3$ and BN possess high dielectric constant, which helps in capturing anions in the liquid electrolyte and transferring lithium ions without coordinating with the anions. This could be the possible reason for the increased discharged plateau of the enhanced case.

The internal resistance of the cell is also determined by electrochemical impedance spectroscopy (EIS) measurement at fully discharged state. As shown in Figure 4.6(B), the internal resistance for BN-$Al_2O_3$ embedded GPE based cell is found to be 6.7 Ohms which is 2 Ohms more that the unenhanced GPE based cell. Also, the diameter of the semicircle, representing the charge transfer resistance, is slightly larger for BN-$Al_2O_3$ embedded GPE based cell ($R_2>R_1$). The small increase in internal resistance and charge transfer resistance may be due to the

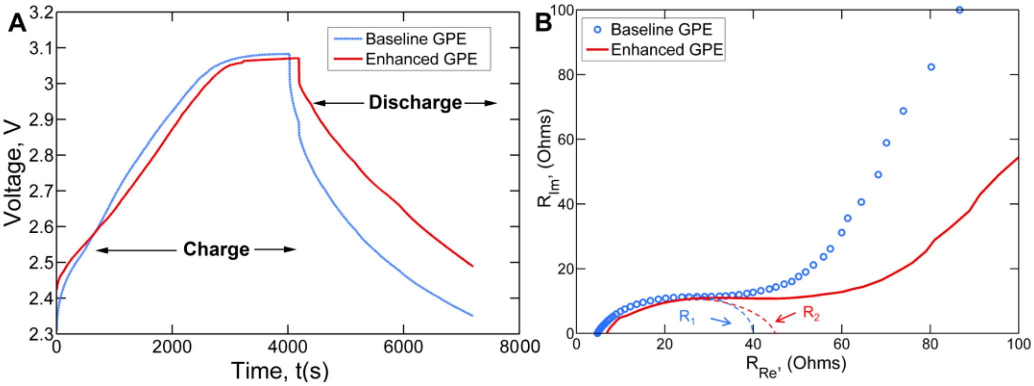

Figure 4.6. Electrochemical evaluation of baseline and thermally enhanced GPEs in a half-coin cell format: (A) charge discharge performance at 5mA, and (B) Electrochemical Impedance Spectroscopy (EIS) measured at fully discharge state.

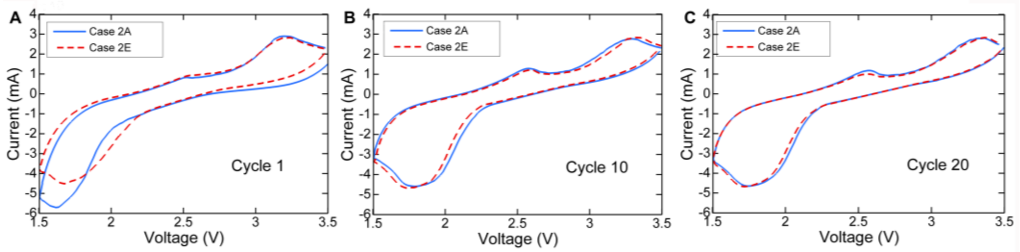

Figure 4.7. Cyclic voltammetry profile of the reversible anodic and cathodic cycles for baseline (Case 2A) and enhanced (Case 2E) GPE based $LiFePO_4$/PVdF-GPE/LiC Li-ion split cell at the scan rate of 0.5mV/s for 1st, 10th and 20th cycle.

presence of the micro/nano particles. Further, cyclic voltammogram (CV) experiments are conducted to investigate the impact of nano/micro particle inclusion in the GPE on cycling performance. Figure 4.7 plots CV profiles of the GPE based Li-ion cell ($LiFePO_4$/PVdF-GPE/Li) at a scan rate of 0.5mV/s for 1st,10th and 20th cycles, over a voltage range of 1.5-3.5V versus Li/Li+ to reveal the continual delithiation/lithiation during the charge and discharge cycles. These plots, particularly at the 10th and 20th cycles show similar characteristics of the baseline (Case 2A) and enhanced (Case 2E) samples. During the 1st cycle, both baseline and enhanced samples exhibit large reduction peak at 1.6V and 1.7V corresponding to reduction of $FePO_4$. Oxidation peaks for baseline and enhanced samples after the 1st cycle is around 3.2V. Reduction and oxidation peaks for both cases shift somewhat to 1.8V and 3.4V respectively after the 10th and 20th cycles, indicating the polarization of electrode material in the first cycle [56]. During the 1st cycle, the CV profile of baseline (Case2A) shows higher peak than that of enhanced (Case2E) samples, indicating more Lithium ions can be reversibly stored/released [57]. However, after around 10 cycles, the values of the current peaks for baseline and enhanced samples are very close to each other, indicating that the reaction kinetics of $Li^+$ ion insertion/extraction is not affected by the presence of the nano-micro particles. These measurements indicate some changes in key electrochemical characteristics due to nanoparticle inclusion that occur along with improved thermal transport. For example, the 2.5X improvement in thermal conductivity is accompanied by a 3X reduction in ionic conductivity, most likely due to the reduced volume fraction of the electrolyte due to nano/microparticle loading [38]. Such a reduction could potentially be offset with a more effective composition of the electrolyte, which has not been optimized in the present work, but is being widely investigated in other efforts [43]. At the cell level, the electrochemical performance of the thermally enhanced cell is not dramatically different from baseline cell. Nevertheless, these changes in electrochemical performance need to be recognized in conjunction with the improved thermal transport in order to appropriately balance thermal-electrochemical trade-offs in the cell.

### 4.4.3 *Theoretical Modeling Results*

The material properties and volume fraction values used for the $k_{eff}$ calculations are listed in Supplementary Table 4.1. The measured thermal conductivity of the micro-nanoparticles embedded PVdF membranes ($k_p$), presented in Table 4.1 are used for the calculation of effective thermal conductivity of the GPE. Thermal conductivity of electrolyte, $k_e$ is taken to be 0.35 W/mK, based on measurements described in section 4.4.1. Based on eq. (4), the theoretical effective thermal conductivity ($k_{eff}$) of the baseline GPE is calculated to be

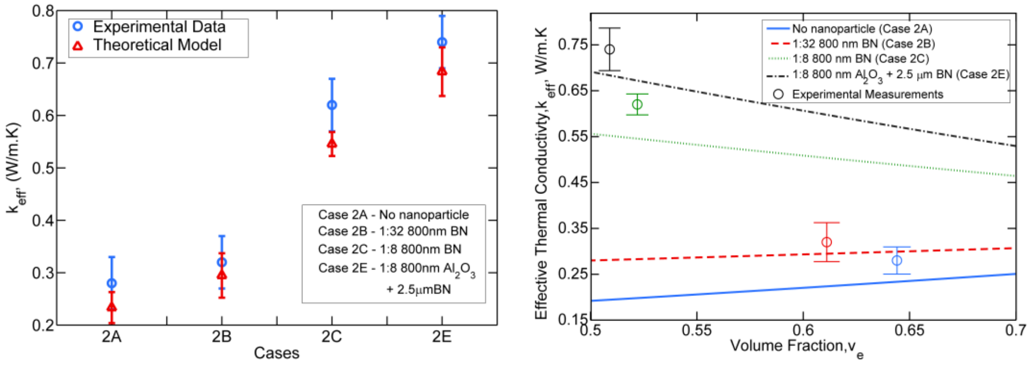

Figure 4.8. (A) Comparison of experimentally measured $k_{eff}$ of GPE samples (Table 4.2) with theoretical predictions based on the Effective medium theory (EMT) model.(B)Theoretically predicted variation of $k_{eff}$ with volume fraction of electrolyte ($v_e$) in GPE. Experimental measurements are also shown for comparison.

0.24±0.03 W/mK, which agrees very closely with the experimentally measured value of 0.28±0.05 W/mK. Figure 4.8(A) compares the theoretically computed values of $k_{eff}$ based on the EMT model with experimental measurements for various micro/nanoparticles embedded in the GPE. In each case, experiment and theory are in good agreement with each other, and are well within the estimated error bounds. Potential sources of error that may contribute towards the small deviation between the two may include error associated with volume fraction calculation, experimental uncertainties associated with measurements, etc. Figure 4.8(B) plots the theoretically calculated $k_{eff}$ as a function of the volume fraction of the dispersed electrolyte phase. Experimentally measured values for four cases listed in Table 4.2

(Cases 2A, 2B, 2C and 2E) are also shown for reference. There is a good agreement between the experimental data and the model. It is interesting to note that going from Case 2B to 2E, a 20% reduction in the volume fraction of electrolyte results in more than 60% increment in the effective thermal conductivity, both measured ceramic fillers at relatively lower weight fraction may result in simultaneous improvement in both thermal conductivity and ionic conductivity. Further optimization may be needed for selecting the right size of nanoparticles and their Concentration in order to balance these thermal-electrochemical tradeoffs in a GPE based Li-ion cell.

## 4.5. Conclusions

This work presents thermal conductivity measurement and enhancement of PVdF-based GPE using BN and $Al_2O_3$ ceramic micro-nanoparticles. Up to 13X and 2.5X improvement in thermal conductivity is reported for PVdF membranes and GPE respectively. Since the baseline GPE has very poor thermal conductivity, this is a significant enhancement that may cause large reduction in operating temperature of GPE-based Li-ion cells, where the GPE offers the greatest thermal impedance among all materials. A theoretical understanding of the effect of nanoparticle inclusion is offered using the effective medium theory, which is found to be in good agreement with experimental measurements. The effect of such thermal enhancement on electrochemical characteristics is also investigated.

Thermal conductivity measurement and enhancement presented in this work are important for a complete understanding of thermal transport in GPE based Li-ion cells, and for designing cells with superior thermal performance. Further, these results highlight the importance of considering thermal-electrochemical tradeoffs in the design of GPE-based Li-ion cells.

## 4.6. Acknowledgments

This material is based upon work supported by CAREER Award No. CBET-1554183 from the National Science Foundation. The authors would like to acknowledge Prof. Fuqiang Liu for useful discussions.

## 4.7. References

[1] Karimi, G., & Li, X. (2013). Thermal management of lithium-ion batteries for electric vehicles. *International Journal of Energy Research, 37*(1), 13-24.

[2] Jung, S., Lauterbach, C., Strasser, M., & Weber, W. (2003, February). Enabling technologies for disappearing electronics in smart textiles. *In Solid-State Circuits Conference, 2003. Digest of Technical Papers. ISSCC. 2003 IEEE International* (pp. 386-387). IEEE.

[3] Zhou, L., Wanga, A., Wu, S. C., Sun, J., Park, S., & Jackson, T. N. (2006). All-organic active matrix flexible display. *Applied Physics Letters*, *88*(8), 083502.

[4] Wang, Q., Ping, P., Zhao, X., Chu, G., Sun, J., & Chen, C. (2012). Thermal runaway caused fire and explosion of lithium ion battery. *Journal of power sources*, *208*, 210-224.

[5] Maleki, H., Deng, G., Anani, A., & Howard, J. (1999). Thermal Stability Studies of Li-Ion Cells and Components. *Journal of The electrochemical society*, *146*(9), 3224-3229.

[6] Meyer, W. H. (1998). Polymer electrolytes for lithium-ion batteries. *Advanced materials*, *10*(6), 439-448.

[7] Stephan, A. M. (2006). Review on gel polymer electrolytes for lithium batteries. *European polymer journal*, *42*(1), 21-42.

[8] Song, J. Y., Wang, Y. Y., & Wan, C. C. (1999). Review of gel-type polymer electrolytes for lithium-ion batteries. *Journal of Power Sources*, *77*(2), 183-197.

[9] Arora, P., & Zhang, Z. (2004). Battery separators. *Chemical reviews*, *104*(10), 4419-4462.

[10] Cho, Jeong Ho, Jiyoul Lee, Yu Xia, BongSoo Kim, Yiyong He, Michael J. Renn, Timothy P. Lodge, and Frisbie, C. D. (2008). Printable ion-gel gate dielectrics for low-voltage polymer thin-film transistors on plastic. *Nature materials*, *7*(11), 900.

[11] Meng, C., Liu, C., Chen, L., Hu, C., & Fan, S. (2010). Highly flexible and all-solid-state paperlike polymer supercapacitors. *Nano letters*, *10*(10), 4025-4031.

[12] Armand, M., & Tarascon, J. M. (2008). Building better batteries. *Nature*, *451*(7179), 652-657.

[13] Lee, Y. S., Lee, J. H., Choi, J., Yoon, W. Y., & Kim, D. W. (2013). Cycling characteristics of lithium powder polymer batteries assembled with composite gel polymer electrolytes and lithium powder anode. *Advanced Functional Materials*, *23*(8), 1019-1027.

[14] Kil, E.H., Choi, K.H., Ha, H.J., Xu, S., Rogers, J.A., Kim, M.R., Lee, Y.G., Kim, K.M., Cho, K.Y. and Lee, S. Y. (2013). Imprintable, Bendable, and Shape-Conformable Polymer Electrolytes for Versatile-Shaped Lithium-Ion Batteries. *Advanced Materials*, *25*(10), 1395-1400.

[15] Appetecchi, G. B., Croce, F., Marassi, R., Panero, S., Ronci, F., Savo, G., & Scrosati, B. (2001). Novel types of lithium-ion polymer electrolyte batteries. *Solid State Ionics*, *143*(1), 73-81.

[16] Sirisopanaporn, C., Fernicola, A., & Scrosati, B. (2009). New, ionic liquid-based membranes for lithium battery application. *Journal of Power Sources*, *186*(2), 490-495.

[17] Shin, J. H., Henderson, W. A., & Passerini, S. (2003). Ionic liquids to the rescue? Overcoming the ionic conductivity limitations of polymer electrolytes. *Electrochemistry Communications*, *5*(12), 1016-1020.

[18] Kumar, A., Logapperumal, S., Sharma, R., Das, M. K., & Kar, K. K. (2016). Li-ion transport, structural and thermal studies on lithium triflate and barium titanate incorporated poly (vinylidene fluoride-co-hexafluoropropene) based polymer electrolyte. *Solid State Ionics*, *289*, 150-158.

[19] Yang, C. M., Kim, H. S., Na, B. K., Kum, K. S., & Cho, B. W. (2006). Gel-type polymer electrolytes with different types of ceramic fillers and lithium salts for lithium-ion polymer batteries. *Journal of power sources*, *156*(2), 574-580.

[20] Goodenough, J. B., & Kim, Y. (2009). Challenges for rechargeable Li batteries. *Chemistry of materials*, *22*(3), 587-603.

[21] Cui, Y., Chai, J., Du, H., Duan, Y., Xie, G., Liu, Z., & Cui, G. (2017). Facile and Reliable in Situ Polymerization of Poly (Ethyl Cyanoacrylate)-Based Polymer Electrolytes toward Flexible Lithium Batteries. *ACS Applied Materials & Interfaces*, *9*(10), 8737-8741.

[22] Shin, J. H., Henderson, W. A., Scaccia, S., Prosini, P. P., & Passerini, S. (2006). Solid-state Li/LiFePO 4 polymer electrolyte batteries incorporating an ionic liquid cycled at 40 C. *Journal of Power Sources*, *156*(2), 560-566.

[23] Sekhon, S. S., & Singh, H. P. (2002). Ionic conductivity of PVdF-based polymer gel electrolytes. *Solid State Ionics*, *152*, 169-174.

[24] Xu, K. (2004). Nonaqueous liquid electrolytes for lithium-based rechargeable batteries. *Chemical reviews*, *104*(10), 4303-4418.

[25] Fernicola, A., Scrosati, B., & Ohno, H. (2006). Potentialities of ionic liquids as new electrolyte media in advanced electrochemical devices. *Ionics*, *12*(2), 95-102.

[26] Egashira, M., Todo, H., Yoshimoto, N., & Morita, M. (2008). Lithium ion conduction in ionic liquid-based gel polymer electrolyte. *Journal of Power Sources*, *178*(2), 729-735.

[27] Armand, M., Endres, F., MacFarlane, D. R., Ohno, H., & Scrosati, B. (2009). Ionic-liquid materials for the electrochemical challenges of the future. *Nature materials*, *8*(8), 621-629.

[28] Vishwakarma, V., Waghela, C., Wei, Z., Prasher, R., Nagpure, S.C., Li, J., Liu, F., Daniel, C. & Jain, A. (2015). Heat transfer enhancement in a lithium-ion cell through improved material-level thermal transport. *Journal of Power Sources*, *300*, 123-131.

[29] Sun, X. G., Fang, Y., Jiang, X., Yoshii, K., Tsuda, T., & Dai, S. (2016). Polymer gel electrolytes for application in aluminum deposition and rechargeable aluminum ion batteries. *Chemical Communications*, *52*(2), 292-295.

[30] Vishwakarma, V., & Jain, A. (2014). Measurement of in-plane thermal conductivity and heat capacity of separator in Li-ion cells using a transient DC heating method. *Journal of Power Sources*, *272*, 378-385.

[31] Shah, K., Vishwakarma, V., & Jain, A. (2016). Measurement of multiscale thermal transport phenomena in Li-ion cells: a review. *Journal of Electrochemical Energy Conversion and Storage*, *13*(3), 030801.

[32] Yang, Y., Huang, X., Cao, Z., & Chen, G. (2016). Thermally conductive separator with hierarchical nano/microstructures for improving thermal management of batteries. *Nano Energy*, *22*, 301-309.

[33] Bruce, P. G., Scrosati, B., & Tarascon, J. M. (2008). Nanomaterials for rechargeable lithium batteries. *Angewandte Chemie International Edition*, *47*(16), 2930-2946.

[34] Breuer, O., & Sundararaj, U. (2004). Big returns from small fibers: a review of polymer/carbon nanotube composites. *Polymer composites*, *25*(6), 630-645.

[35] Shan, J., & Tenhu, H. (2007). Recent advances in polymer protected gold nanoparticles: synthesis, properties and applications. *Chemical Communications*, (44), 4580-4598.

[36] Li, Z., Su, G., Wang, X., & Gao, D. (2005). Micro-porous P (VDF-HFP)-based polymer electrolyte filled with Al 2 O 3 nanoparticles. *Solid State Ionics*, *176*(23), 1903-1908.

[37] He, Y., & Hong, J. M. (2011). Effect of Nano-Sized ZnO Particle Addition on PVDF Ultrafiltration Membrane Performance. In *Advanced Materials Research*(Vol. 311, pp. 1818-1821). Trans Tech Publications.

[38] Sakarya, O., Kurama, S., & Gunkaya, G. (2016). Effect of Al2O3 Nanofiller on ion conductivity, transmittance, and glass transition temperature of PEI: LiTFSI: PC: EC polymer electrolytes. *J. of Polymer Research*, *24*(1), 14.

[39] Kim, K. W., Kim, H. W., Kim, Y., & Kim, J. K. (2017). Composite gel polymer electrolyte with ceramic particles for LiNi 1/3 Mn 1/3 Co 1/3 O 2-Li 4 Ti 5 O 12 lithium ion batteries. *Electrochimica Acta*, *236*, 394-398.

[40] Ishida, H., & Rimdusit, S. (1998). Very high thermal conductivity obtained by boron nitride-filled polybenzoxazine. *Thermochimica Acta*, *320*(1), 177-186.

[41] Zhou, W., Qi, S., An, Q., Zhao, H., & Liu, N. (2007). Thermal conductivity of boron nitride reinforced polyethylene composites. *Materials Research Bulletin*, *42*(10), 1863-1873.

[42] Lee, G. W., Park, M., Kim, J., Lee, J. I., & Yoon, H. G. (2006). Enhanced thermal conductivity of polymer composites filled with hybrid filler. *Composites Part A: App. science and manufacturing*, *37*(5), 727-734.

[43] Zhang, R., Hashemi, N., Ashuri, M., & Montazami, R. (2013, July). Advanced gel polymer electrolyte for lithium-ion polymer batteries. In *ASME 2013 7th International Conference on Energy Sustainability collocated with the ASME 2013 Heat Transfer Summer Conference and the ASME 2013 11th International Conference on Fuel Cell Science, Engineering and Technology* (pp. V001T05A005-V001T05A005). American Society of Mechanical Engineers.

[44] Zheng, Z., Song, Y., Yang, R., & Zheng, Q. (2015). Direct evidence for percolation of immobilized polymer layer around nanoparticles accounting for sol–gel transition in fumed silica dispersions. *Langmuir*, *31*(50), 13478-13487.

[45] Kim, J. R., Choi, S. W., Jo, S. M., Lee, W. S., & Kim, B. C. (2004). Electrospun PVdF-based fibrous polymer electrolytes for lithium ion polymer batteries. *Electrochimica Acta*, *50*(1), 69-75.

[46] Zhang, S. S. (2006). A review on electrolyte additives for lithium-ion batteries. *Journal of Power Sources*, *162*(2), 1379-1394.

[47] Pandey, G. P., & Hashmi, S. A. (2009). Experimental investigations of an ionic-liquid-based, magnesium ion conducting, polymer gel electrolyte. *Journal of Power Sources*, *187*(2), 627-634.

[48] Incropera, F. P., & Dewitt, D. P. Introduction to Heat Transfer (1996). *John WHey & Sons. New York. NY*.

[49] Gustafsson, S. E. (1991). Transient plane source techniques for thermal conductivity and thermal diffusivity measurements of solid materials. *Review of scientific instruments*, *62*(3), 797-804.

[50] Gustafsson, S. E., Karawacki, E., & Khan, M. N. (1979). Transient hot-strip method for simultaneously measuring thermal conductivity and thermal diffusivity of solids and fluids. *Journal of Physics D: Applied Physics*, *12*(9), 1411.

[51] Progelhof, R. C., Throne, J. L., & Ruetsch, R. R. (1976). Methods for predicting the thermal conductivity of composite systems: a review. *Polymer Engineering & Science*, *16*(9), 615-625.

[52] Ingham, D. B., & Pop, I. (1998). *Transport phenomena in porous media*. Elsevier.

[53] Landauer, R. (1952). The electrical resistance of binary metallic mixtures. *Journal of Applied Physics*, *23*(7), 779-784.

[54] Kirkpatrick, S. (1973). Percolation and conduction. *Reviews of modern physics*, *45*(4), 574.

[55] Hashin, Z., & Shtrikman, S. (1962). A variational approach to the theory of the effective magnetic permeability of multiphase materials. *Journal of applied Physics*, *33*(10), 3125-3131.

[56] Ju, Z., Zhang, E., Zhao, Y., Xing, Z., Zhuang, Q., Qiang, Y., & Qian, Y. (2015). One-Pot Hydrothermal Synthesis of FeMoO4 Nanocubes as an Anode Material for Lithium-Ion Batteries with Excellent Electrochemical Performance. *Small*, *11*(36), 4753-4761.

[57] Jiang, R., Cui, C., & Ma, H. (2013). Using graphene nanosheets as a conductive additive to enhance the rate performance of spinel LiMn 2 O 4 cathode material. *Physical Chemistry Chemical Physics*, *15*(17), 6406-6415.

## CHAPTRER 4 APPENDIX 1

# SUPPLEMENTARY MATERIALS

# ENHANCEMENT OF THERMAL TRANSPORT IN GEL-POLYMER ELECTROLYTES WITH EMBEDDED BN/AL$_2$O$_3$ NANO- AND MICRO-PARTICLES

Vishwakarma, V., & Jain, A. (2017). Enhancement of Thermal Transport in Gel-Polymer Electrolytes with Embedded BN/Al2O3 Nano- and Micro-Particles. Journal of Power Sources, (Accepted 11 July 2017).

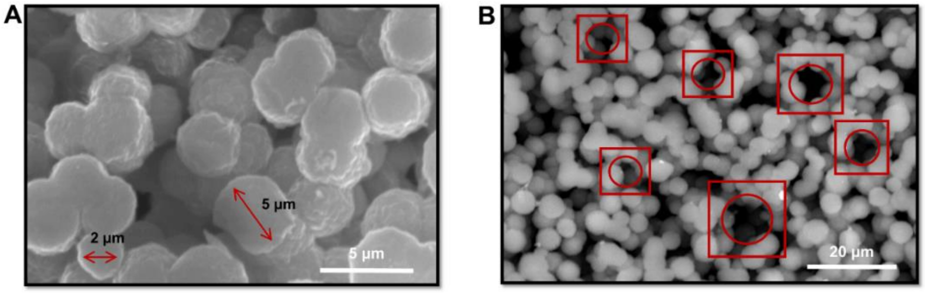

Supplementary Figure S1. (A) SEM image of PVdF membrane showing typical grain size; (B) SEM image of PVdF membrane showing porosity and average diameter of the pores.

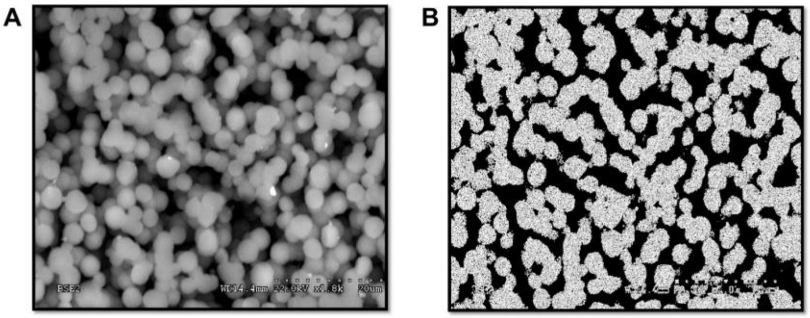

Supplementary Figure S2. A) SEM image of the GPE B) Image analysis of this image to show the presence of a continuous thermal conduction path in the GPE matrix.

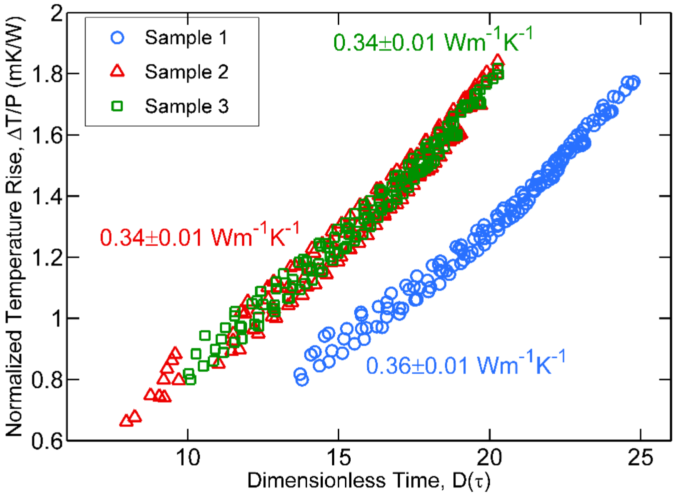

Supplementary Figure S3. Normalized temperature rise, *ΔT/P* as a function of dimensionless time *D(τ)* for thermal conductivity ($k_e$) measurements on the electrolyte. . Data from three separate measurements are shown to establish repeatability.

Supplementary Table 1. Measurements of thermal conductivity of PVdF membrane ($k_p$) and volume fraction of electrolyte, $v_e$ for calculating the effective thermal conductivity of the GPE, $k_{eff}$ using Effective medium theory model

| **GPE Samples** | **Weight Ratio of Nano/microparticles** | **PVdF Thermal Conductivity, $k_p$, W/m.K** | **Volume Fraction of electrolyte, $v_e$** |
|---|---|---|---|
| Baseline | 0 | 0.09±0.002 | 0.64±0.02 |
| BN | 1:32 | 0.22±0.004 | 0.61±0.02 |
| BN | 1:8 | 0.83±0.017 | 0.52±0.02 |
| $Al_2O_3$, BN | 1:8 | 1.2±0.024 | 0.51±0.02 |

# CHAPTER 5

# CONCLUSION AND FUTURE WORK

The need for continued improvement in performance, safety, and reliability of Li-ion cells makes it imperative to continue to innovate not only in thermal transport phenomena but also in the interactions with other thermal transport processes. The coupled, multiscale nature of physics governing a Li-ion cell makes this a challenging task, with significant potential for performance improvement through the fundamental understanding of these processes. These potential improvements may positively impact energy storage and conversion for a wide variety of engineering systems. This work is focused on heat transfer of lithium ion battery at material level by investigating not only individual material but also the nature of their interaction with each other. The separator material is expected to have the lowest thermal conductivity among all materials in the electrode stack of a Li-ion cell. In chapter 2 we present a novel experimental method to measure the in-plane thermal conductivity and heat capacity of the separator from a Li-ion cell. Experimental data from this measurement method, based on a thermally semi-infinite domain in the separator, are found to be in excellent agreement with the underlying theoretical model. Data suggest that the separator has poor thermal conductivity, which does not change significantly at a higher temperature. These measurements contribute towards the understanding of thermal conduction within a Li-ion cell and provide useful thermal property data that has so far been missing from the literature for a material of much importance for ensuring safety and performance of Li-ion cells.

We have also identified that interfacial thermal conduction between cathode and separator as the rate-limiting material-level component of heat transfer within a Li-ion cell, contributing around 88% of the overall thermal resistance of the cell. Results also indicate the dramatic reduction in this thermal resistance without affecting electrochemical resistance based on the surface modification. Experimental measurements of the interfacial thermal contact resistance are in good agreement with predictions based on the acoustic mismatch model. These measurements also correctly predict cell-level thermal properties of a Li-ion cell. Results indicate the possibility of significant improvement in cell-level thermal conductivity and reduction in operating temperature rise as a result of the surface modification.

Further in Chapter 4, we present thermal conductivity measurement and enhancement of PVdF-based GPE using BN and $Al_2O_3$ ceramic micro-nanoparticles. Up to 13X and 2.5X improvement in thermal conductivity is reported for PVdF membranes and GPE respectively. Since the baseline GPE has very poor thermal conductivity, this is a significant enhancement that may cause a large reduction in operating temperature of GPE-based Li-ion cells, where the GPE offers the greatest thermal impedance among all materials. A theoretical understanding of the effect of nanoparticle inclusion is offered using the effective medium theory, which is found to be in good agreement with experimental measurements. The effect of such thermal enhancement on electrochemical characteristics is also investigated

Thermal conductivity measurement and enhancement presented in chapter 4 are important for a complete understanding of thermal transport in GPE based Li-ion cells, and for designing cells with superior thermal performance. Further, these results highlight the importance of considering thermal-electrochemical tradeoffs in the design of GPE-based Li-ion cells.

In the last two decades, Li-ion cells have emerged as a promising future energy storage and conversion systems with plenty of research towards electrochemical optimization to obtain maximum performance. However, such efforts towards developing thermally efficient Li-ion cell is lacking. This dissertation presents the ex-situ measurements of thermal conductivity and specific heat capacity of the battery materials such as traditional separators, GPE, Separator-

Electrode interfaces, which are crucial for thermal modeling and simulations of Li-ion cell for a wide variety of applications. However, these simulations can be made more accurate if in-situ (dynamic) thermal transport properties are used instead of ex-situ. As a part of the future direction, we propose the development of experimental techniques to capture the dynamic nature of thermal transport properties during Li-ion cell in operation. Such measurements will help in accurate estimation of cell temperature rise and develop efficient thermal management methodologies.

# APPENDIX A

# COPYRIGHT PERMISSIONS

## 1. ASME

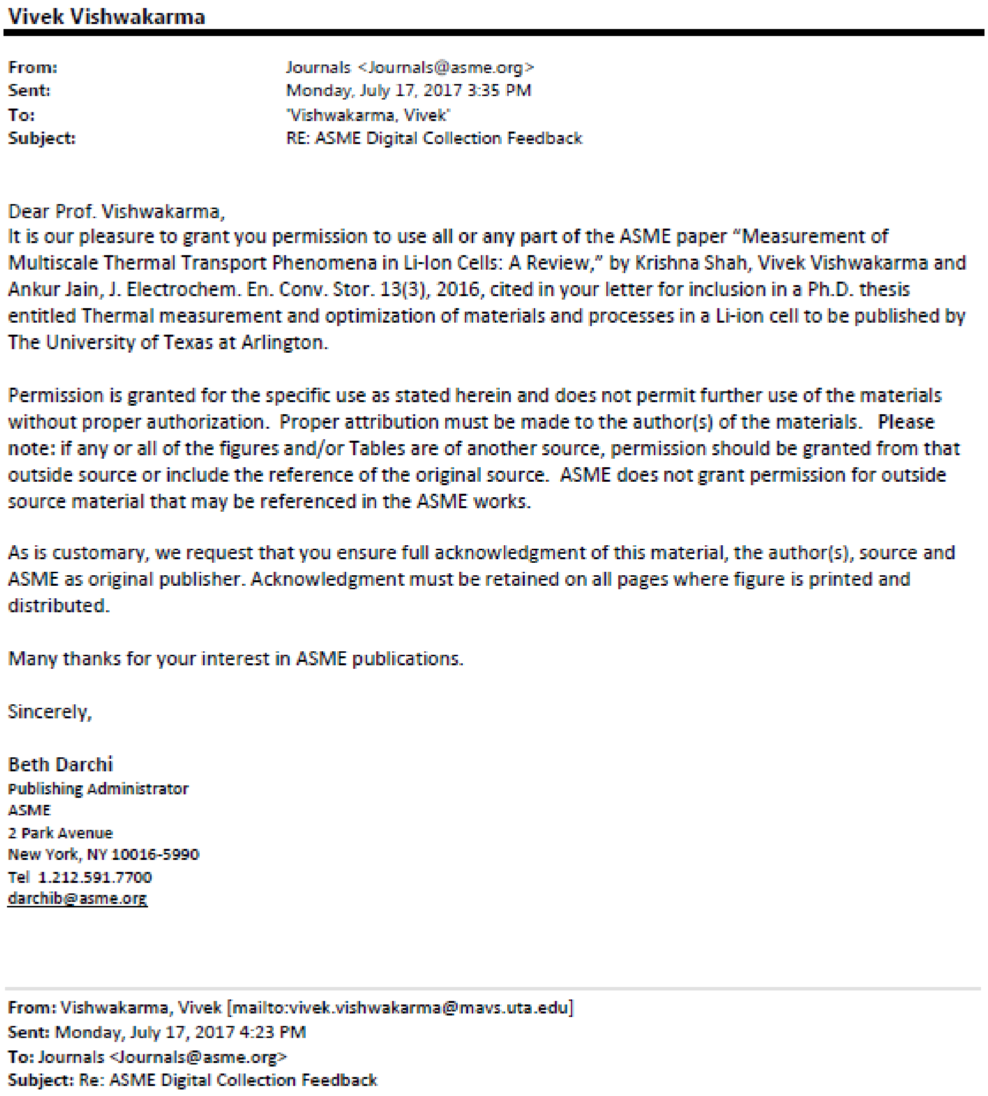

**Vivek Vishwakarma**

| | |
|---|---|
| **From:** | Journals <Journals@asme.org> |
| **Sent:** | Monday, July 17, 2017 3:35 PM |
| **To:** | 'Vishwakarma, Vivek' |
| **Subject:** | RE: ASME Digital Collection Feedback |

Dear Prof. Vishwakarma,
It is our pleasure to grant you permission to use all or any part of the ASME paper "Measurement of Multiscale Thermal Transport Phenomena in Li-Ion Cells: A Review," by Krishna Shah, Vivek Vishwakarma and Ankur Jain, J. Electrochem. En. Conv. Stor. 13(3), 2016, cited in your letter for inclusion in a Ph.D. thesis entitled Thermal measurement and optimization of materials and processes in a Li-ion cell to be published by The University of Texas at Arlington.

Permission is granted for the specific use as stated herein and does not permit further use of the materials without proper authorization. Proper attribution must be made to the author(s) of the materials. **Please note:** if any or all of the figures and/or Tables are of another source, permission should be granted from that outside source or include the reference of the original source. ASME does not grant permission for outside source material that may be referenced in the ASME works.

As is customary, we request that you ensure full acknowledgment of this material, the author(s), source and ASME as original publisher. Acknowledgment must be retained on all pages where figure is printed and distributed.

Many thanks for your interest in ASME publications.

Sincerely,

**Beth Darchi**
**Publishing Administrator**
**ASME**
**2 Park Avenue**
**New York, NY 10016-5990**
**Tel 1.212.591.7700**
**darchib@asme.org**

---

**From:** Vishwakarma, Vivek [mailto:vivek.vishwakarma@mavs.uta.edu]
**Sent:** Monday, July 17, 2017 4:23 PM
**To:** Journals <Journals@asme.org>
**Subject:** Re: ASME Digital Collection Feedback

2. ELSEVIER (https://www.elsevier.com/__data/assets/pdf_file/0007/55654/AuthorUserRights.pdf )

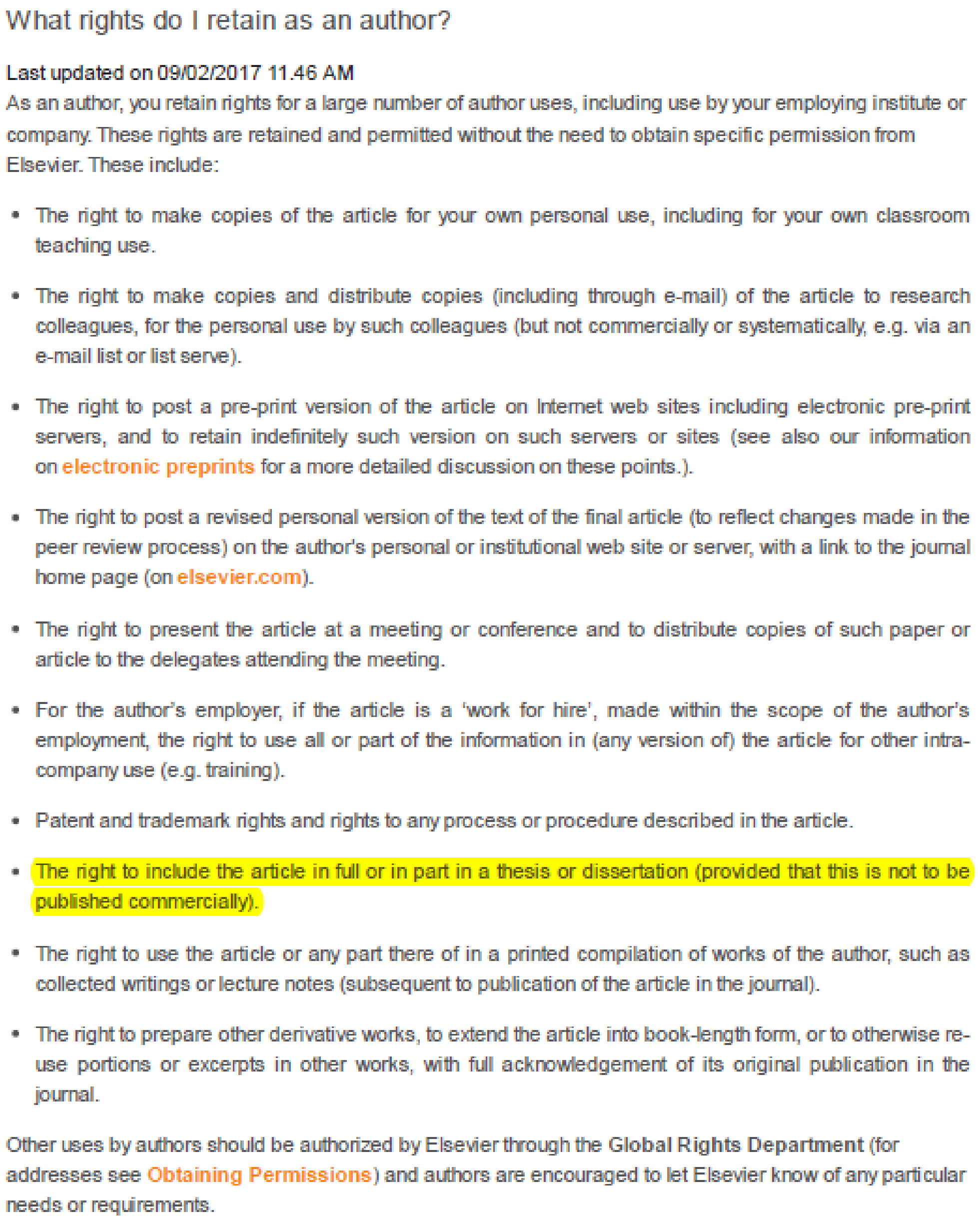

## What rights do I retain as an author?

**Last updated on 09/02/2017 11.46 AM**

As an author, you retain rights for a large number of author uses, including use by your employing institute or company. These rights are retained and permitted without the need to obtain specific permission from Elsevier. These include:

- The right to make copies of the article for your own personal use, including for your own classroom teaching use.
- The right to make copies and distribute copies (including through e-mail) of the article to research colleagues, for the personal use by such colleagues (but not commercially or systematically, e.g. via an e-mail list or list serve).
- The right to post a pre-print version of the article on Internet web sites including electronic pre-print servers, and to retain indefinitely such version on such servers or sites (see also our information on electronic preprints for a more detailed discussion on these points.).
- The right to post a revised personal version of the text of the final article (to reflect changes made in the peer review process) on the author's personal or institutional web site or server, with a link to the journal home page (on elsevier.com).
- The right to present the article at a meeting or conference and to distribute copies of such paper or article to the delegates attending the meeting.
- For the author's employer, if the article is a 'work for hire', made within the scope of the author's employment, the right to use all or part of the information in (any version of) the article for other intra-company use (e.g. training).
- Patent and trademark rights and rights to any process or procedure described in the article.
- The right to include the article in full or in part in a thesis or dissertation (provided that this is not to be published commercially).
- The right to use the article or any part there of in a printed compilation of works of the author, such as collected writings or lecture notes (subsequent to publication of the article in the journal).
- The right to prepare other derivative works, to extend the article into book-length form, or to otherwise re-use portions or excerpts in other works, with full acknowledgement of its original publication in the journal.

Other uses by authors should be authorized by Elsevier through the **Global Rights Department** (for addresses see Obtaining Permissions) and authors are encouraged to let Elsevier know of any particular needs or requirements.

# BIOGRAPHICAL STATEMENT

Vivek Vishwakarma was born in M.P., India, in 1990. He received his B.Tech. from Indian Institute of Technology (IIT), Ropar, in 2012 and Ph.D. from The University of Texas at Arlington in 2017, all in Mechanical Engineering. During his undergraduate studies he worked to simulate and optimize a solar based cooling system under the supervision of Dr. Himanshu Tyagi. Vivek was selected for the joint UNSW-IIT Ropar Sustainable Energy workshop and attended the workshop in UNSW Sydney, Australia, during April 2012. He has also worked at Roche Tissue Diagnostics of F. Hoffmann-La Roche AG (Tucson, AZ) as a Graduate Research Intern during the summer of 2015 and 2016. His research interests includes Thermal management in Li-ion batteries, Cell and pack level modeling, Li-ion battery material characterization and reliability, MEMS, Silicon IC fabrication and Bio-MEMS. In the near future, he aspire to pursue his career in industry.